Civil Engineering and Applied Solutions, 2025; 1(3): 1–16

Civil Engineering and Applied Solutions

Research Article

journal homepage: ceas.journals.umz.ac.ir

CEAS Civil Engineering and Applied Solutions

Shape Optimization of Truss Structures for Displacement Constraints Using a Modified Particle Swarm Optimization (MPSO) Algorithm

Seyed Mohammad Seyedpoor [a*], Morteza Pendashteh [a]

[a] *Department of Civil Engineering, Shomal University, Amol, Iran*

ARTICLE INFO

Keywords:
Shape optimization
Truss structures
Particle swarm optimization
Modified particle swarm optimization

Article history:
Received 03 June 2025
Accepted 14 July 2025
Available online 01 August 2025

ABSTRACT

This paper presents a modified particle swarm optimization (MPSO) algorithm for the shape optimization of truss structures under displacement constraints. The proposed MPSO employs a multi-stage strategy, where the final solution of each stage is used to reinitialize the swarm in the next stage, improving convergence accuracy. A normal-based distribution is used for swarm regeneration, promoting effective exploration around the best solution found. Design variables are the nodal coordinates of the structures, and the total weight is considered as the objective function. Design constraints include limitations on nodal displacements, and some geometric constraints are also considered. The method is evaluated using four benchmark truss examples. Results show that MPSO reduces structural weight by 7% for the 13-bar truss, 5.7% for the 25-bar truss, and 2.2% for the 52-bar truss, compared to those reported in the literature, while also maintaining or improving displacement control. In the 37-bar planar truss, the algorithm marginally outperforms the existing result by reducing weight by 0.18%. These outcomes confirm that the proposed MPSO provides competitive or superior performance compared to reference methods in both efficiency and solution quality.

1. Introduction

Over recent years, substantial progress has been made in optimizing structures with linear elastic behavior. In many studies related to the optimal design of structures, instead of using classical mathematical methods, modern optimization algorithms have been used, and their performance is assessed. Natural processes often inspire modern optimization methods and offer key advantages, such as eliminating the need for derivative information and enhancing the ability to find global optima. Among these, a prominent class is metaheuristic algorithms, which have gained widespread attention for their effectiveness in tackling complex constrained optimization problems where traditional methods often fall short [1]. Metaheuristic algorithms are commonly categorized into three main groups, including evolutionary algorithms (e.g., genetic algorithm, differential evolution) [2, 3]; swarm intelligence methods (e.g., particle swarm optimization, ant colony optimization) [4-7]; and physics-inspired algorithms (e.g., simulated annealing) [8, 9].

Rajeev and Krishnamoorthy [10] modified the simple genetic algorithm introduced by Goldberg [11] for minimizing the structural weight as the objective function while the discrete area members of the structure were considered as the design variables. Wang et al. [12] made an effort to find the optimal shape of structures with displacement constraints. Lee and Geem [13] introduced a harmonic search algorithm (HS) for size optimization of truss structures under various loading conditions. Toğan and Daloğlu [14] introduced an adaptive approach in genetic algorithms (GA) in order to optimize three-dimensional truss structures. A modified genetic algorithm (MGA) was used by Salajegheh et al. [15] to optimize the space structures, in which the optimal size and shape design under various static loading conditions were studied. Limitations on stress, nodal displacement, and slenderness ratio were considered as design constraints, and structural weight was also selected as the objective function. Cheng [16] used a hybrid genetic

---

* Corresponding author.
E-mail addresses: s.m.seyedpoor@gmail.com (S. M. Seyedpoor).

https://doi.org/10.22080/ceas.2025.29404.1017
ISSN: 3092-7749/© 2025 The Author(s). Published by University of Mazandaran.
This article is an open access article distributed under the terms and conditions of the Creative Commons Attribution (CC-BY) license (https://creativecommons.org/licenses/by/4.0/deed.en)
How to cite this article: Seyedpoor, S. M., Pendashteh, M. Shape Optimization of Truss Structures for Displacement Constraints Using a Modified Particle Swarm Optimization (MPSO) Algorithm. Civil Engineering and Applied Solutions. 2025; 1(3): 1–16. doi:10.22080/ceas.2025.29404.1017.

algorithm for the optimal design of steel trusses of arched bridges, where the total structural weight was considered as the objective function. An enhanced charge system search (CSS) to determine the size and configuration optimum design of structures was introduced by Kaveh and Talatahari [17].

Particle swarm optimization (PSO), introduced by Kennedy and Eberhart [18], is a widely used metaheuristic known for its simplicity, fast convergence, and minimal parameter tuning. Its effectiveness has led to broad applications across disciplines, including structural engineering. Seyedpoor et al. [19] combined PSO with SPSA for truss size optimization, demonstrating improved efficiency in several benchmark problems. Luh and Lin [20] developed a two-stage PSO method for truss optimization, combining binary PSO for topology design and ARPSO for size and shape optimization. Their approach outperformed genetic algorithms and ant colony optimization in terms of structural weight, solution quality, and computational efficiency. The work of Gholizadeh [21] involved the formulation of a hybrid optimization technique for truss layout design, which integrates PSO alongside cellular automata (CA). This approach utilized a new CA-based PSO (CPSO) to improve particle paths, while constraints were addressed through a sequential unconstrained minimization technique (SUMT) paired with an exact penalty function. The findings indicated that SCPSO surpassed traditional PSO and other methods in reducing structural weight, speeding up convergence, and enhancing computational efficiency. Kaveh and Zolghadr [22] developed a democratic particle swarm optimization (DPSO) algorithm to address premature convergence in standard PSO, particularly in structural optimization problems with frequency constraints. The proposed DPSO introduces a democratic decision-making process where all eligible particles contribute to updating positions, enhancing exploration, and preventing local optima stagnation. Mortazavi and Toğan [23] introduced an integrated particle swarm optimizer (IPSO) for simultaneous size, shape, and topology optimization of truss structures. The algorithm employs a unified coding scheme within a ground structure framework to represent all design variables in a single solution vector. This integration allows for efficient exploration of the design space while satisfying structural constraints. Cao et al. [24] proposed an enhanced particle swarm optimization (EPSO) algorithm to improve the size and shape optimization of truss structures. EPSO integrates new movement rules and diversity-preserving mechanisms to prevent premature convergence and enhance global search ability. Tsiptsis et al. [25] Integrated isogeometric analysis (IGA) with PSO to improve structural shape optimization. By leveraging the smoothness and accuracy of NURBS-based IGA within the PSO framework, the method enhanced geometric representation and reduced numerical errors. Jafari et al. [26] proposed a hybrid optimization method integrating Particle Swarm Optimization (PSO) with cultural algorithm (CA) for truss structure design. In the proposed PSOC algorithm, the cultural space is used to guide particle movements, restrict variables within feasible ranges, and eliminate unnecessary analyses. By modifying the personal best term and applying a selective analysis strategy based on structural weight changes, the algorithm improves convergence speed and solution quality.

In this study, a modified version of the particle swarm optimization algorithm referred to as modified particle swarm optimization (MPSO) is introduced for the shape optimization of truss structures under displacement constraints. The proposed MPSO algorithm incorporates a multi-stage search strategy to improve convergence and solution accuracy. The method is validated using several benchmark truss examples, and numerical results indicate the effectiveness and robustness of MPSO in achieving optimized structural configurations.

2. PSO algorithm

The particle swarm optimization (PSO) algorithm was first introduced by Kennedy and Eberhart [18] in 1995. The algorithm has been inspired by the life of birds that live sociably and supply their needs together, such as searching for food. According to the algorithm, it has been assumed that the birds instinctively recognize their distance to the food while they are not aware of the food location. Furthermore, all the birds, by sharing their information, are aware of the location nearest to the food. In this algorithm, each bird can be considered as a potential solution called a particle, and the group of particles is called the swarm. Each particle has a fitness value that can be obtained by the objective function of the optimization problem. Accordingly, a bird that is closer to the food has the most merit. Each bird also has a velocity vector that indicates the movement direction and the size of the bird. During the optimization process, the location of a bird based on its personal experience and the experience of other birds is improved.

Numerically, the position of the *i*th particle at iteration $k + 1th$ is improved by Eq. 1. In this formula V_{k+1}^{i} is the modified velocity of the *i*th particle that can be obtained from Eq. 2 and Δt is a time step which may be calculated by Eq. 3. In many studies, the time step is assumed to be 1.

$$X_{k+1}^{i} = X_{k}^{i} + V_{k+1}^{i}\Delta t \tag{1}$$

$$V_{k+1}^{i} = \rho_k V_{k}^{i} + c_1 r_1 \frac{(P_{k}^{i} - X_{k}^{i})}{\Delta t} + c_2 r_2 \frac{(P_{k}^{g} - X_{k}^{i})}{\Delta t} \tag{2}$$

$$\Delta t = \frac{1}{k_{max}} \tag{3}$$

where V_{k}^{i} is the velocity vector at iteration k, r_1 and r_2 are two random numbers between zero and one, P_{k}^{i} shows the best position of the i^{th} particle, and P_{k}^{g} is the best position of all particles until the k^{th} iteration in all groups. The c_1 and c_2 are called the trust and confidence parameters, ρ is a parameter called the inertia weight, and $k_{\max}$ stands for the maximum number of iterations.

Due to the importance of inertia weight in the PSO algorithm to reach the global solution, rather than considering a fixed value for ρ during the optimization process, it can be linearly varied from a maximum value ρ_{max} to a minimum value ρ_{min} as:

$$\rho_k = \rho_{max} - \frac{\rho_{max} - min}{k_{max} - 1}(k-1) \tag{4}$$

More information about the PSO algorithm can be found in research by Kennedy and Eberhart [18] and Seyedpoor et al. [27]. The PSO algorithm flowchart is shown in Fig. 1.

3. Modified particle swarm optimization (MPSO) algorithm

The MPSO algorithm is a modified form of the PSO algorithm. The main body of the MPSO algorithm consists of the PSO. According to the algorithm, instead of implementing the PSO algorithm at once, it is run in several stages so that the final solution of each stage is used to create an initial swarm for the next optimization stage. In the first stage of the optimization, an initial swarm is randomly generated within the allowable space of design variables. In the next stage, the swarm is produced by a normal distribution around the solution obtained from the previous stage according to Eq. 5, and the PSO program is called again. This process is repeated until a satisfactory convergence is achieved in solving the optimization problem.

$$X^i = X_{MPSO}\{1 + randn(i,j)\}_{nv\times 1}Covx, \quad i = 1,\dots,np, \ j = 1,\dots,nv \tag{5}$$

where the randn (i, j) is a function that will generate a random quantity with a normal distribution, and *Covx* is the variation coefficient of the random variable. Also, *np* and *nv* are the total number of particles and design variables in optimization.

The MPSO algorithm flowchart is shown in Fig. 2.

4. The optimal design problem

In this study, the capabilities of the MPSO algorithm for solving the shape optimization of truss structures are studied. The truss optimization problem under displacement constraints is examined, and the optimal design problem can be expressed as:

$$\begin{aligned} &\text{Find} && : X = \{x_1, x_2, \dots, x_{nv}\}^T \\ &\text{Minimize} && : W(X) \\ &\text{Subject to} && : g_q(X) \leq , \ \ q = 1,\dots,m \\ &&& \ \ X^1 \leq X \leq X^u \end{aligned} \tag{6}$$

where X is a design variable vector with *nv* unknowns, $W(X)$ represents an objective function that should be minimized, and g_q is the *qth* constraint from *m* inequality constraints. Also, X^l and X^u represent the lower and upper bounds of the design variable vector, respectively.

4.1. The design variables

In optimization of truss structures, the nodal coordinates of joints are considered as the design variable vector that can be expressed as:

$$X = \{x_1, y_1, z_1, \dots, x_i, y_i, z_i, \dots, x_{nj}, y_{nj}, z_{nj}\}^T \tag{7}$$

where x_i, y_i, *and* z_i are the x, y, and z coordinates of joint i of the structure, and *nj* is the total number of joints in the truss.

4.2. The objective function

The total weight of the truss structure is considered as the objective function, which can be defined as follows:

$$W(X) = \sum_{n=1}^{ng} a_n \sum_{i=1}^{nm} \gamma_i l_i\,(X) \tag{8}$$

where γ_i and l_i are the specific weight and length of the *ith* member of the structure, respectively; *nm* is the total number of members in group *n* having the sectional area a_n, and *ng* is the total number of area groups in the structure.

4.3. Design constraints

Design constraints include some restrictions on nodal displacements and a number of geometric ones. Nodal displacement constraints can be given by Eq. 9.

$$g_{dj}(X) = \frac{|\delta_j|}{|\delta_{ju}|} - 1 \leq 0 \quad j = 1,\dots,nj \tag{9}$$

where δ_j is the nodal displacement of node *j*; δ_{ju} is the allowable displacement of node *j*, and *nj* is the total number of displacement constraints.

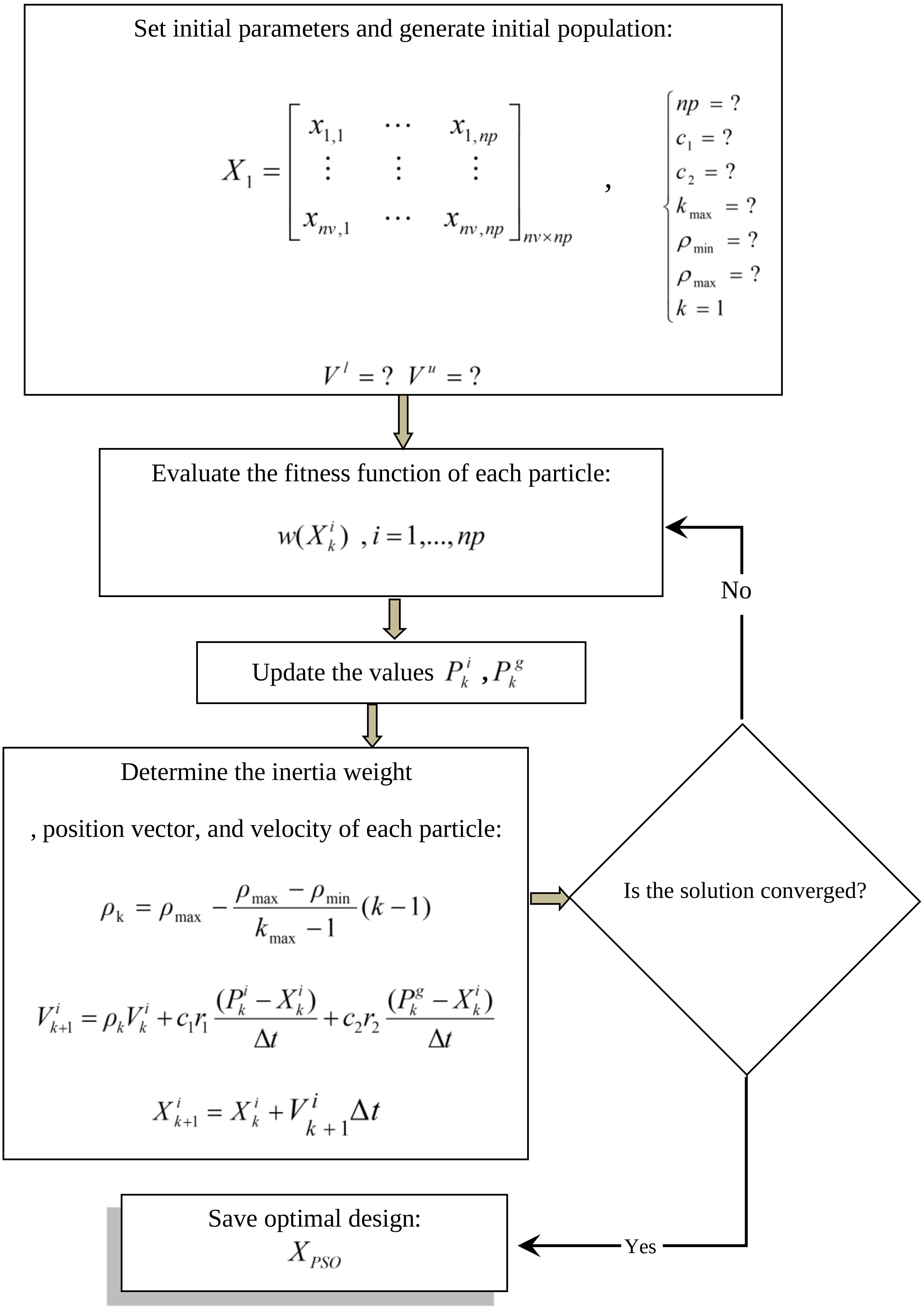

Fig. 1. PSO algorithm flowchart.

In this study, a fitness function (quasi-objective function) is defined by Eq. 10:

$$Z(X, r_p) = W(X)\left\{1 + r_p \sum_{q=1}^{m}\left[max\left(0, g_q(X)\right)\right]^2\right\} \tag{10}$$

where Z is the fitness function and r_p is a penalty multiplier.

5. Numerical examples

In order to assess the performance of the proposed method, four standard test examples are selected from the literature. The examples consist of a 13-bar planar truss, a 25-bar space truss, a 52-bar space truss, and a 37-bar planar truss, respectively. The input parameters of the MPSO algorithm for all the test examples are given in Table 1.

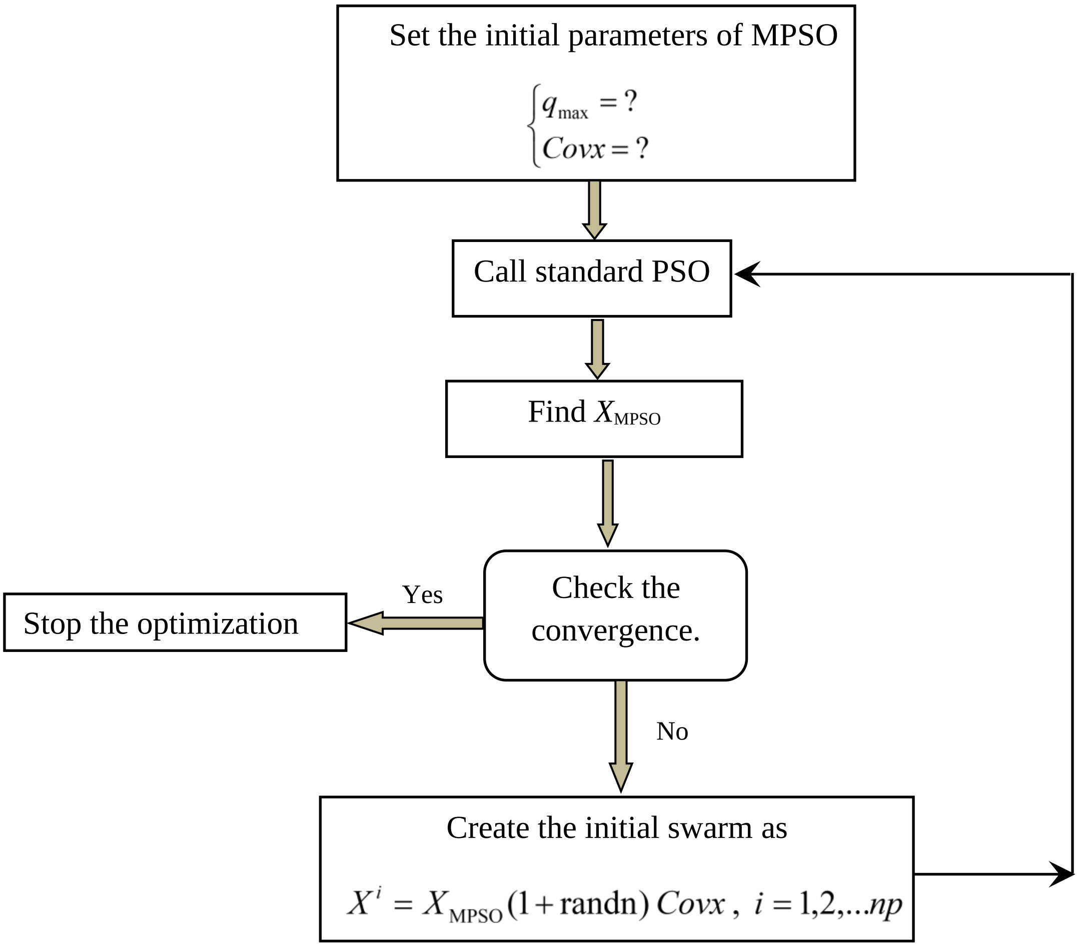

Fig. 2. MPSO algorithm flowchart.

Table 1. Initial parameters of the MPSO algorithm.

Parameters	Describtiom	Value
c_1	Cognitive parameter	2.00
c_2	Social parameter	2.00
ρ_{min}	Minimum of inertia weight	0.01
ρ_{max}	Maximum of inertia weight	0.90
np	Swarm size for examples 1–4, respectively	10, 10, 30, 20
k_{max}	Maximum number of PSO iterations for examples 1–4, respectively	40, 40, 60, 60
q_{max}	Maximum number of MPSO iterations for examples 1–4, respectively	5, 6, 5, 6
$Covx$	Variation coefficient	0.015

5.1. Thirteen-bar planar truss

The first example is a 13-bar planar truss, as shown in Fig. 3. The optimum shape design of the structure has been made by Wang et al. [12] under nodal displacement constraints. The structure is subjected to the vertical load of 200 kN at node 1. The maximum vertical displacement of nodes should be smaller than or equal to 1.168 mm. Young's modulus is $E = 2.1 \times 10^{11}$Pa, and the material density is 7800 kg/m^3. The cross-sectional area of all bars is equal to A = 10 cm^2. For shape optimization, nodes 3 and 7 in the horizontal direction and nodes 4, 5, and 6 in the vertical direction are allowed to move. During the optimization process, the structural symmetry must be maintained. So, with respect to the symmetry shape of the structure, the positions of nodes 5, 6, and 7 must be considered as the design variables.

Before the optimization, the structural weight was 71.4 kg. When the vertical load of 200 kN is applied at node 1, the vertical displacement of the node reaches 4.805 mm. Wang et al. [12], could reach the total weight of the truss from 71.4 kg to 78.6 kg, while the nodal displacement decreased from 4.805 mm to 1.168 mm. In this study, to demonstrate the performance of the MPSO, the structure is optimized, and the results are compared with those reported by Wang et al. [12] in Table 2.

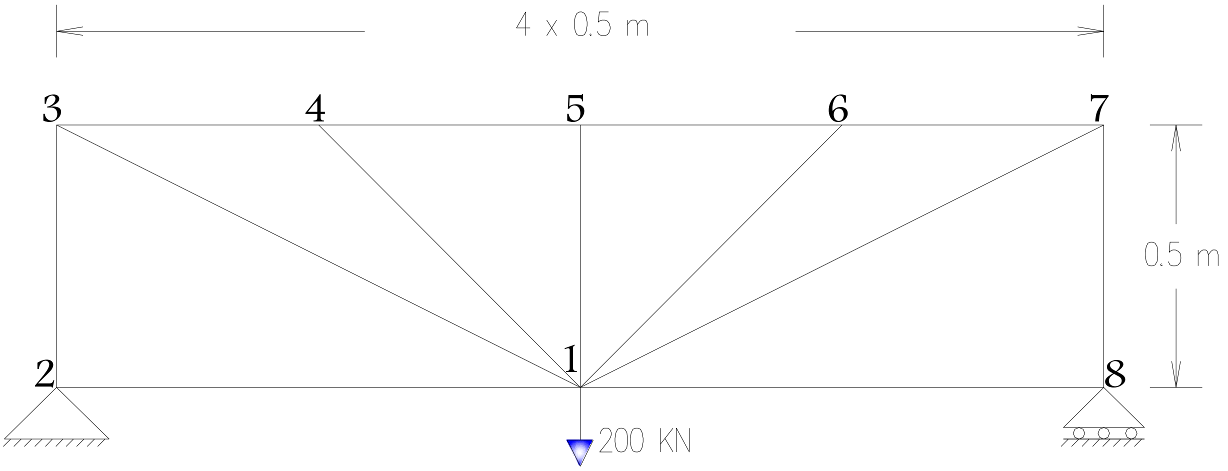

Fig. 3. Thirteen-bar planar truss.

As given in the table, the optimum weight obtained by MPSO is 73.068 kg, while the vertical displacement of node 1 is 1.168 mm. It can be concluded that the structure weight is reduced by 7% when compared with those obtained by Wang et al. [12]. The optimum shape of the structure obtained by MPSO is shown in Fig. 4.

Table 2. Optimal design comparison for the 13-bar planar truss.

Design variables(m)	Initial coordinates	Optimum coordinates [12]	Optimum coordinates MPSO
y_5	0.5	1.008	0.8911
y_6	0.5	0.867	0.745
x_7	1.0	0.848	0.756
Weight (kg)	71.40	78.6	73.068
δ_{max} (mm)	4.805	1.168	1.168

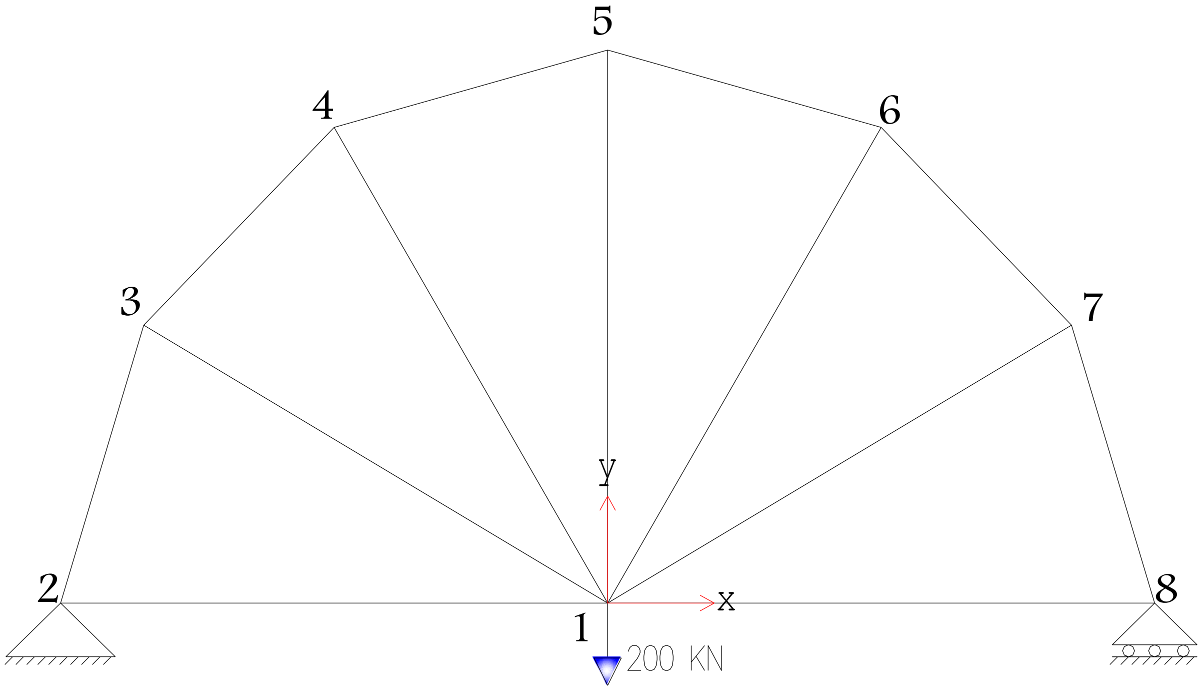

Fig. 4. Shape optimization of 13-bar planar truss obtained by MPSO.

The convergence history of optimization is shown in Fig. 5, where the objective function is represented in terms of the optimization stage. As can be seen, in each stage of optimization, the objective function increases to satisfy the displacement constraint. Fig. 6 shows the vertical displacement of node 1 in terms of the optimization stage.

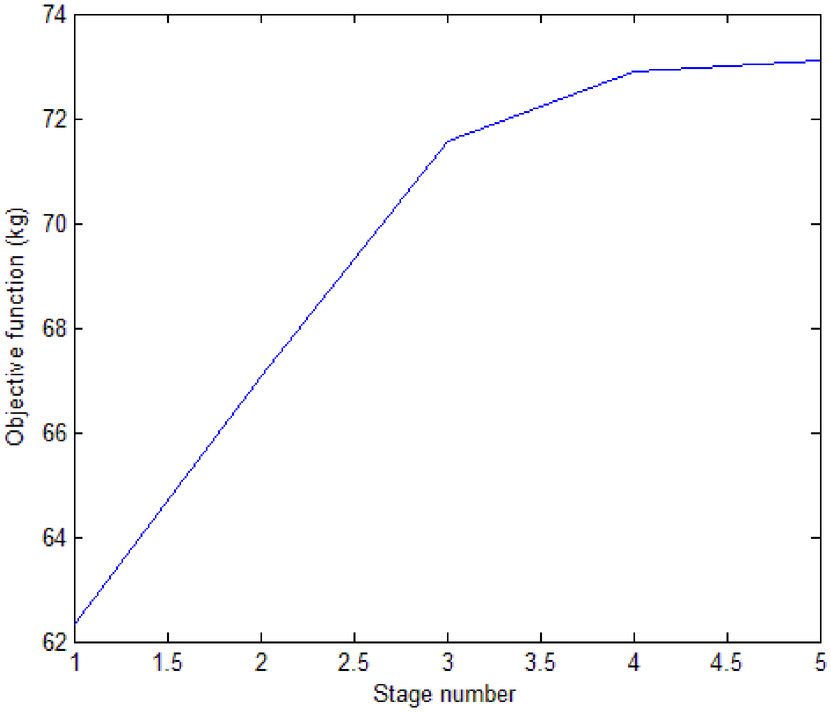

Fig. 5. The convergence history of MPSO for the 13-bar planar truss.

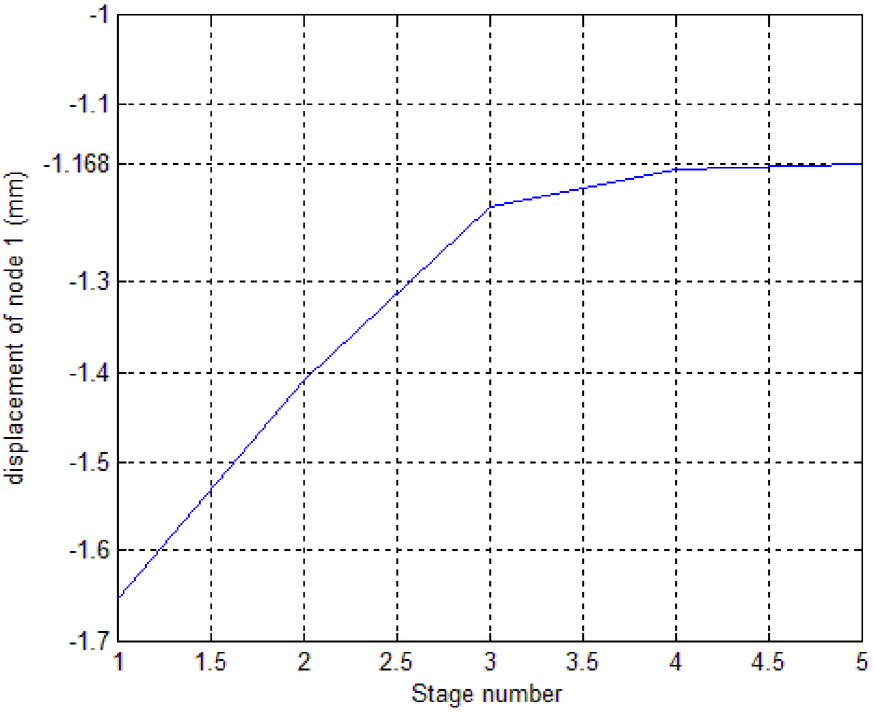

Fig. 6. Displacement variations of node 1 of the 13-bar planar truss for the MPSO algorithm.

5.2. Twenty-five-bar space truss

The shape optimization of a 25-bar space truss shown in Fig. 7 is considered as the second example [12]. The modulus of elasticity is $E = 6.89 \times 10^{10}$Pa and mass density is $\rho = 2768$ kg/m^3. The structure is subjected to two separate loading conditions as given in Table 3. Design constraints are considered to limit the vertical displacement of nodes to 8.89 mm. During the optimization process, the fully symmetric structure should be preserved. Therefore, nodes 4 and 8 are allowed to move along the *x*, *y*, *z*, and *x*, *y* axes, respectively, and the optimal design problem has four shape variables. In this example, the member areas are divided into two groups as listed in Table 4. The initial design variables of the truss, the best solution achieved by MPSO, and that reported by Wang et al. [12] are given in Table 5.

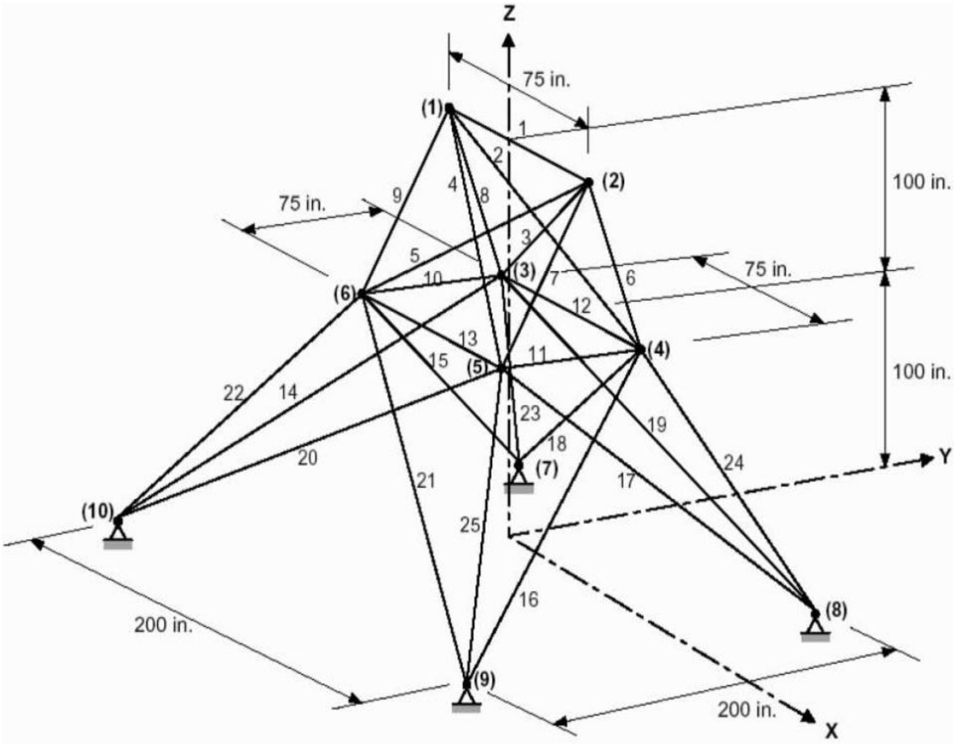

Fig. 7. The 25-bar space truss.

Table 3. Loading cases for the 25-bar space truss.

Node	Load case 1 (kN)			Load case 2 (kN)		
	Px (kN)	Py (kN)	Pz (kN)	Px (kN)	Py (kN)	Pz (kN)
1	4.4482	44.482	-22.241	0.0	88.964	-22.241
2	0.0	44.482	-22.241	0.0	-88.964	-22.241
3	2.2241	0.0	0.0	0.0	0.0	0.0
6	2.2241	0.0	0.0	0.0	0.0	0.0

Table 4. Member area grouping for the 25-bar space truss.

Group number	Truss elements	Area (cm^2)
1	A_1-A_9	4
2	A_{10}–A_{25}	5

Table 5. Optimal design comparison for the 25-bar space truss.

Design variables (m)	Initial coordinates	Optimum coordinates [12]	Optimum coordinates MPSO
X_4	0.952	0.608	0.3814
Y_4	0.952	1.957	1.8767
Z_4	2.54	2.756	3.0475
X_8	2.54	1.575	1.2948
Y_8	2.54	3.020	2.4490
Weight (Kg)	109.00	114.40	107.84
$\delta_{\max}$ (mm)	29.60	8.89	8.89

The initial structure weighs 109.0 kg, leading to a displacement of 29.60 mm for node 1. Wang et al. [12] reached the structural weight from 109.0 kg to 114.40 kg, while the nodal displacement of the joint changed from 29.6 mm to 8.89 mm. In fact, after optimization, the structural weight increased by 4.95% and the displacement decreased by 70%.

The MPSO could achieve a weight of 107.84 kg and nodal displacement of 8.89 mm. Compared with the primary shape of the structure, nodal displacement 70% reduced and the structural weight 1.06% reduced. Compared to the solution of Wang et al. [12], the displacement does not change, but the structural weight 5.7% reduced. The optimal shape of the structure is shown in Fig. 8. According to the results given in Table 5, reaching a reasonable configuration for the structure, the performance of the MPSO method can be realized.

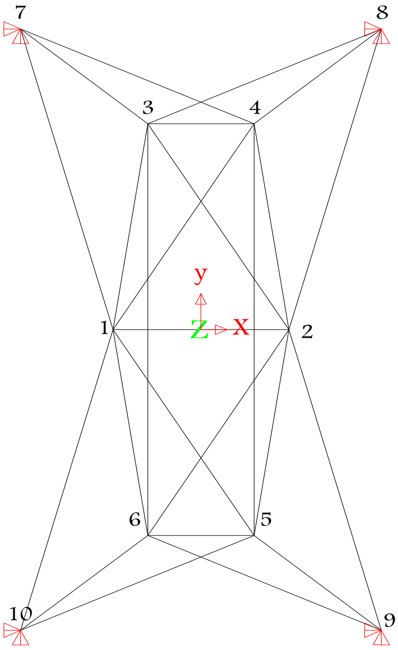

Fig. 8. Optimal design of 25-bar space truss obtained by the MPSO algorithm.

The convergence history of the optimization process for the 25-bar space truss is shown in Fig. 9. Fig. 10 also shows the maximum displacement of the truss nodes for two load cases in terms of optimization stage.

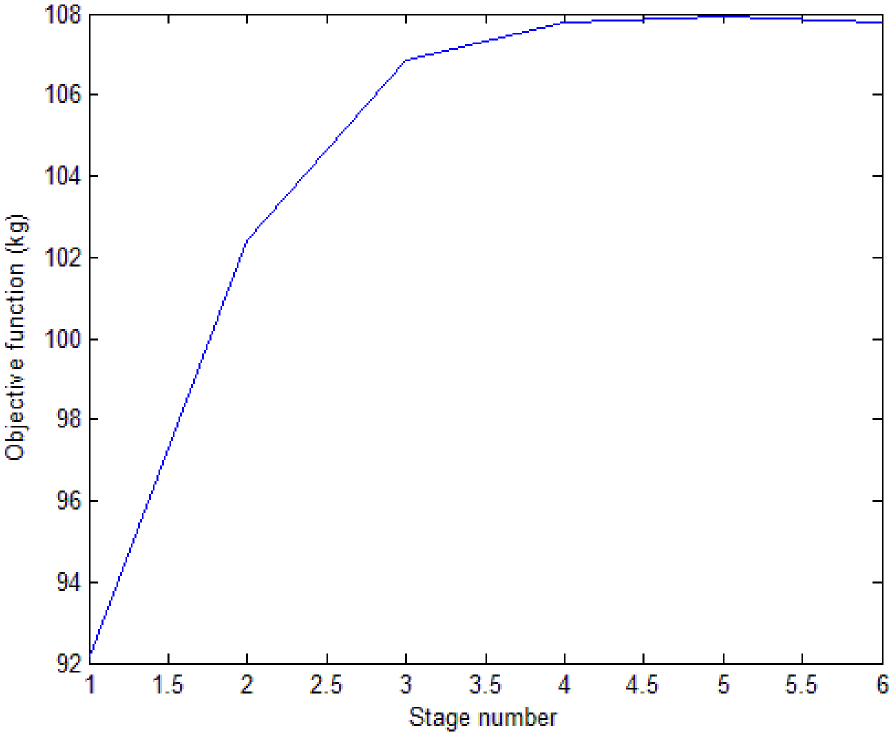

Fig. 9. Convergence history of MPSO for 25-bar space truss.

5.3. *Fifty-two-bar dome structure*

The third example is a 52-bar dome structure, as shown in Fig. 11 [12]. The structure is under four load cases given in Table 6. The modulus of elasticity and mass density of the structure are considered $E = 2.1 \times 10^{11}$Pa and ρ=7850 kg/m^3, respectively. Displacement of node 1 along the z axis is limited to 10 mm. During the optimization process, the axial symmetry for the dome structure should be preserved. Thus, the x and z coordinates of nodes 1, 2, and 6 are considered as design variables, and the optimization problem has six design variables related to the shape of the structure. In this example, the cross-section of all members is assumed to be 10 cm^2.

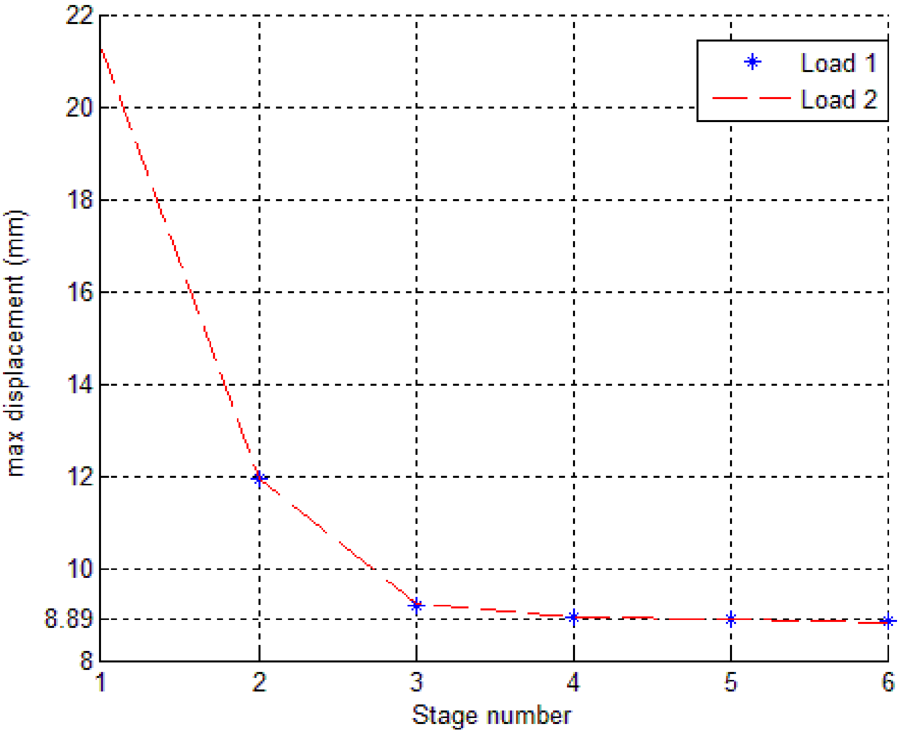

Fig. 10. Maximum displacement variations of the 25-bar space truss for two load cases.

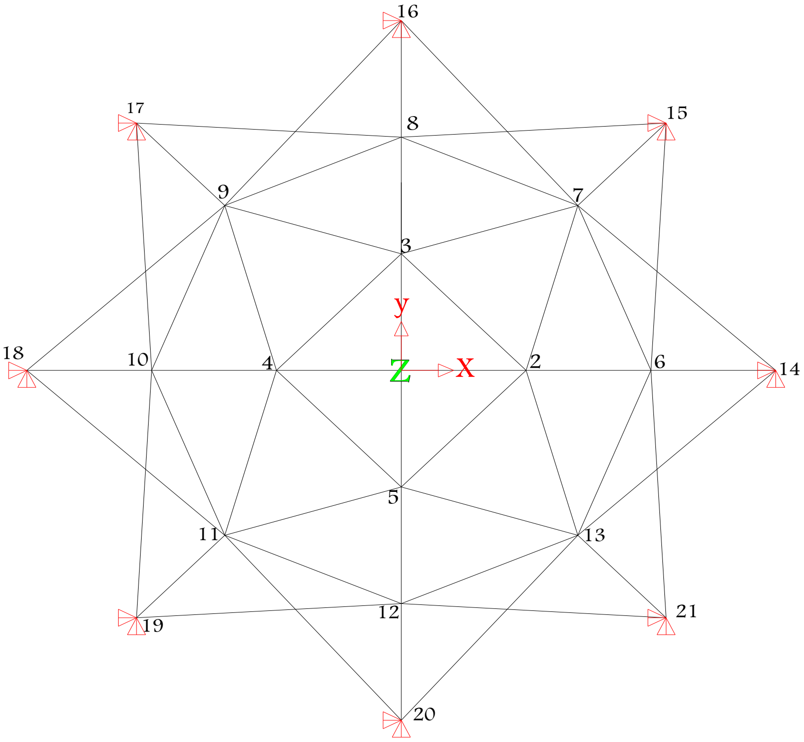

Fig. 11. Fifty-two-bar dome structure.

Table 6. Load cases for the dome structure.

Load cases	Node	P_z (kN)
1	1	300
2	1-13	300
3	1	150
	4-5	100
4	1	150
	2-4	70

The initial values of design variables, the best solution obtained by MPSO, and that reported by Wang et al. [12] are compared in Table 7.

Table 7. Optimal design comparison for the 52-bar dome structure.

Design variables (m)	Initial coordinates	Optimum coordinates [12]	Optimum coordinates MPSO
X_1	0.00	0.00	0.00
Z_1	9.25	9.62	8.3230
X_2	5.00	2.10	1.5666
Z_2	8.22	7.41	6.8363
X_6	10.0	7.21	5.5000
Z_6	5.14	4.08	4.3386
Weight (kg)	3459.2	3174.80	3104.50
δ_{max} (mm)	63.04	10	10

The initial structure weighs 3459.2 kg, leading to a maximum displacement of 63.04 mm for node 1. Wang et al. [12] reached the structural weight from 3459.2 kg to 3174.8 kg, so that the weight and maximum displacement of the structure 8.2% and 84%, respectively, were reduced. The MPSO achieved a weight of 3104.5 kg, leading to 1 cm for node 1. The displacement and weight 84% and 10.3 % have been reduced compared to the original shape. Compared with the solution of Wang et al. [12], structural weight 2.2% reduced. The optimum shape of the structure and the convergence history of optimization are shown in Figs. 12 and 13, respectively. Fig.14. shows displacement variations of node 1 for different load cases of the 52-bar space structure.

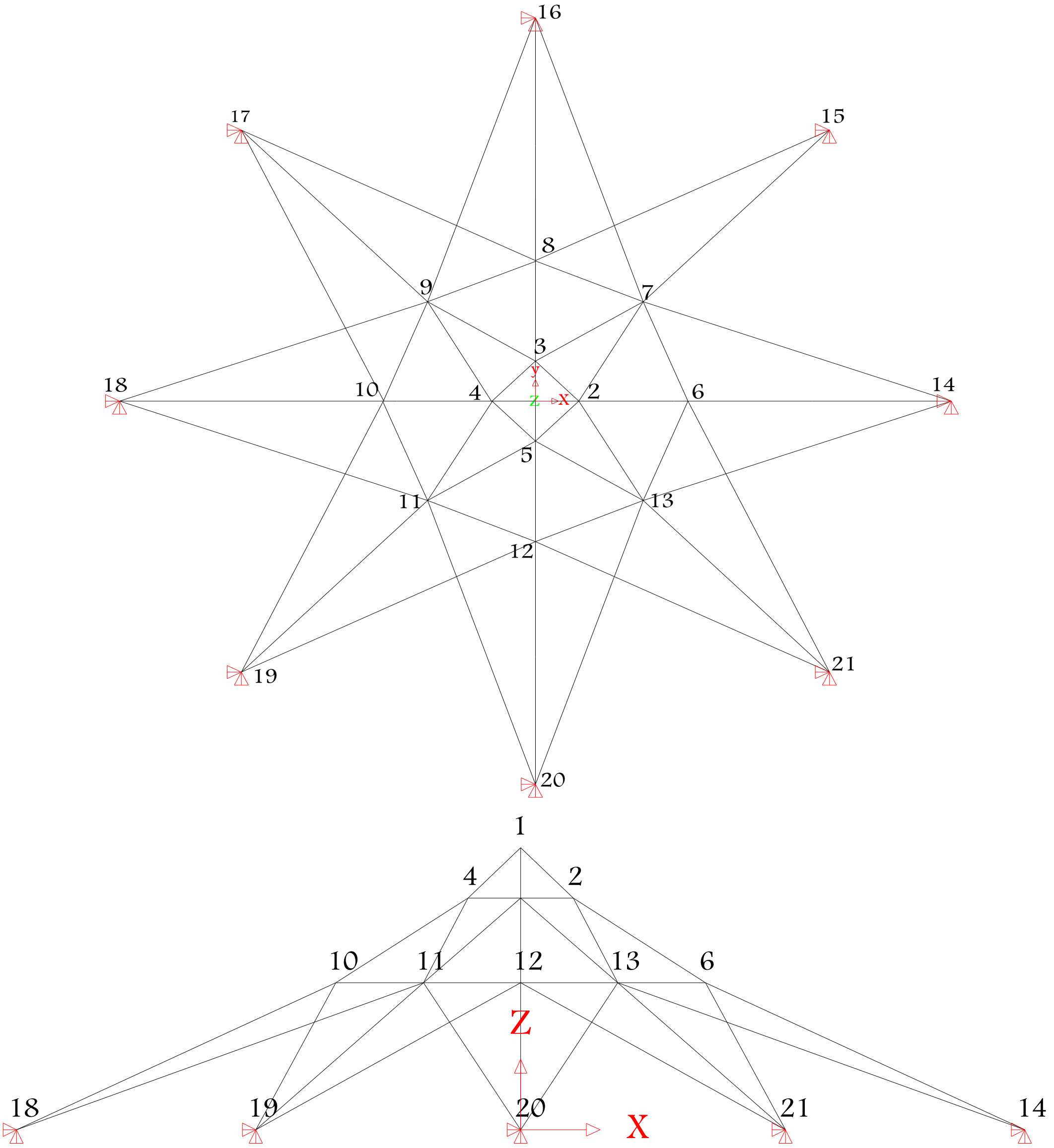

Fig. 12. Optimum configuration of the dome structure.

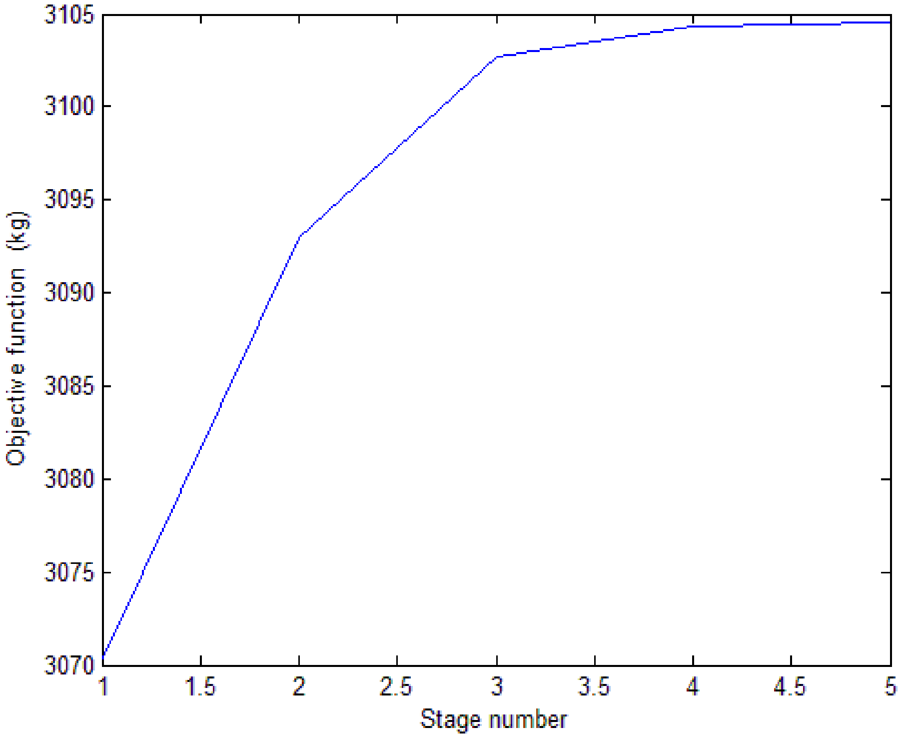

Fig. 13. The convergence history of MPSO for a 52-bar space structure.

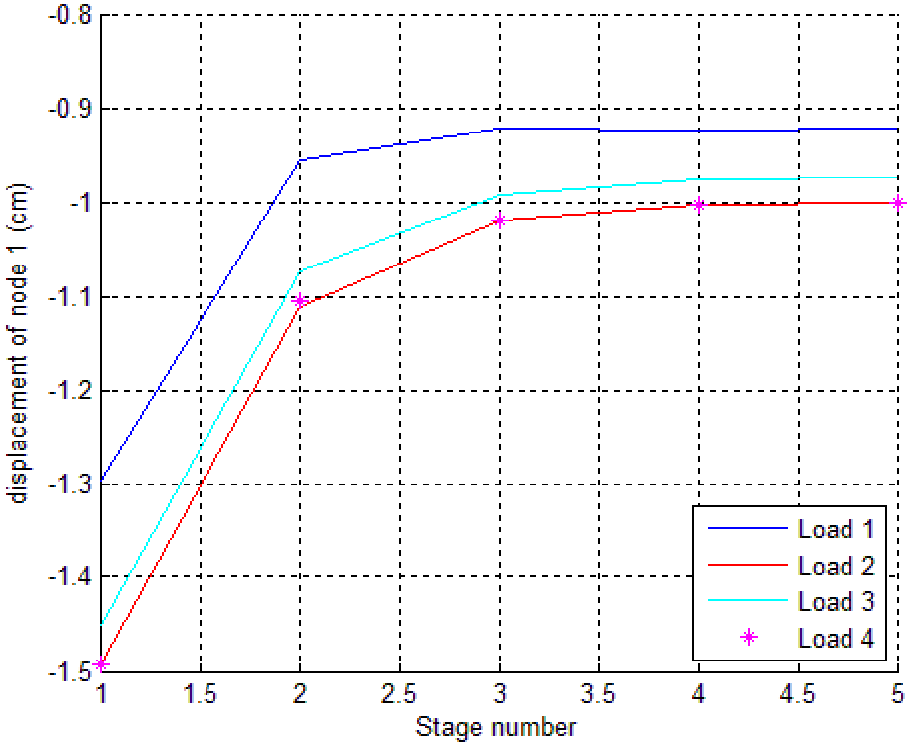

Fig. 14. Displacement variations of node 1 for different load cases of the 52-bar space structure.

5.4. Thirty-seven-bar planar truss

The last example is related to the optimization of the structure of a bridge, a 37-bar-planar truss as shown in Fig. 15. The truss structure is under two load cases given in Table 8. The modulus of elasticity is $E = 2.1 \times 10^{11}$Paand mass density is ρ=7800 kg/m^3. Vertical displacement of nodes 8 and 10 is limited to 10 mm. Bottom nodes of the bridge structure are kept constant, and top nodes are allowed to move along the y-axis. During the optimization process, the fully symmetric structures should be preserved. Thus, the y coordinates of nodes 3, 5, 7, 9, and 11 are considered here as the design variables. As shown in Fig. 15, the truss members are divided into two groups. Bottom members have a sectional area of 40cm^2, and the other members have a sectional area of 5cm^2. The initial values of design variables, the best solution obtained by MPSO, and the solution of Wang et al. [12] are given in Table 9.

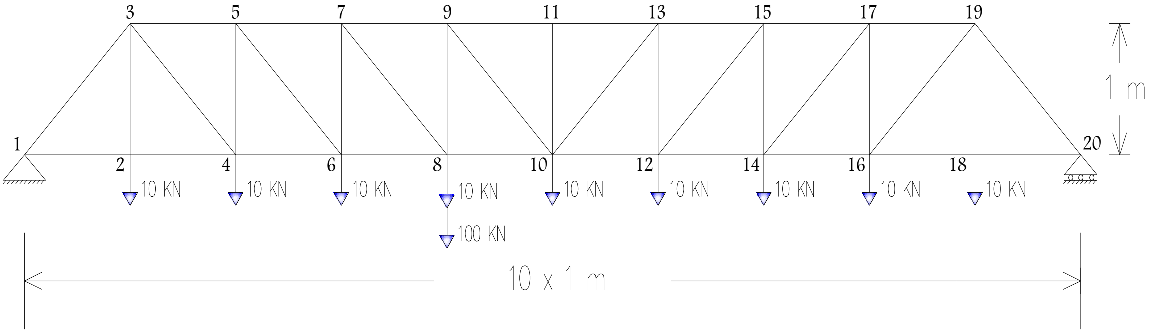

Fig. 15. Thirty-seven-bar bridge truss.

Table 8. Loading conditions for the 37-bar planar truss.

Load cases	P_y (kN)	Nodes
1	-10.0	2-4-6-8-10-12-14-16-18
2	-100	8

Table 9. Optimal design comparison for the 37-bar planar truss.

Design variables (m)	Initial coordinates	Optimum coordinates [12]	Optimum coordinates MPSO
Y_3	1.00	1.042	1.086
Y_5	1.00	1.646	1.6373
Y_7	1.00	2.172	2.1804
Y_9	1.00	2.449	2.4216
Y_{11}	1.00	2.544	2.4539
Weight (kg)	433.5	489.06	488.73
δ_{max} (mm)	32	10	10

The initial weight of the truss is 433.5 kg, leading to a maximum displacement of 32 mm at node 8. Wang et al. [12] reached the weight from 433.5 kg to 489.6 kg with 10 mm for nodal displacements. Indeed, the weight of the structures 13% increased while the displacement 69% reduced. In this study, the MPSO reached a weight of 488.73 kg while the maximum displacement of nodes reached 10 mm. It can be observed that the structural weight, 0.18% has decreased when compared with that obtained by Wang et al. [12].

The optimum shape of the structure is shown in Fig. 16. The convergence history of optimization is depicted in Fig. 17. All the results demonstrate the efficiency of the proposed MPSO for shape optimization of truss structures.

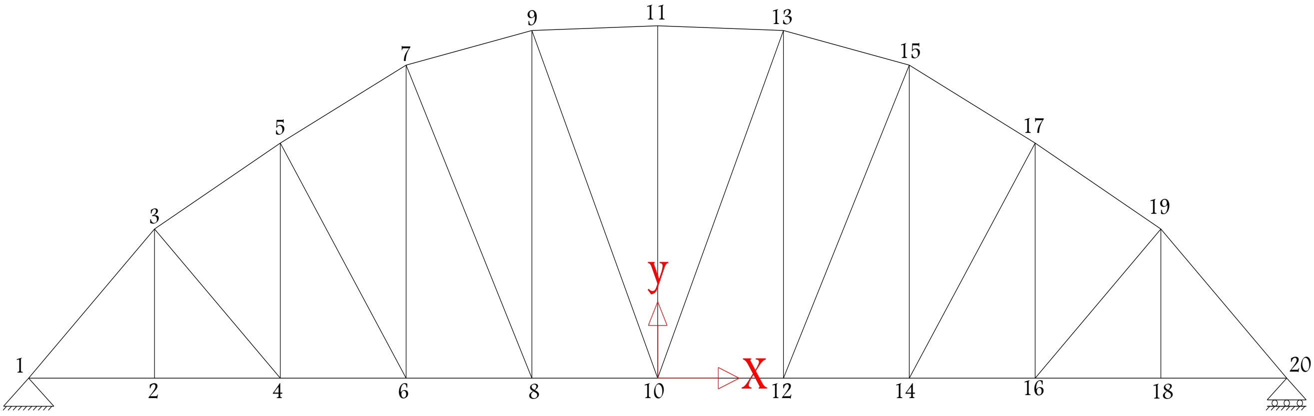

Fig. 16. Optimum configuration of simply supported bridge.

Fig.18. shows the vertical displacement variations of nodes 8 and 10 for two load cases of a 37-bar space structure for the MPSO algorithm, where the maximum displacement at node 8 and critical loading is loading 2.

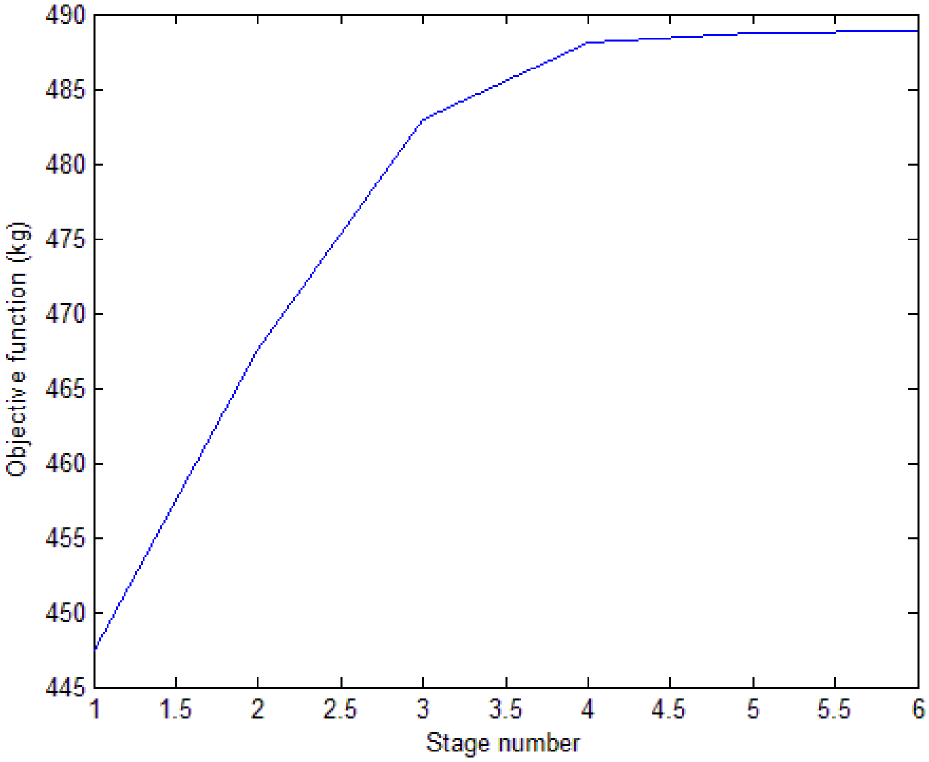

Fig. 17. The convergence history of MPSO for the 37-bar planner truss.

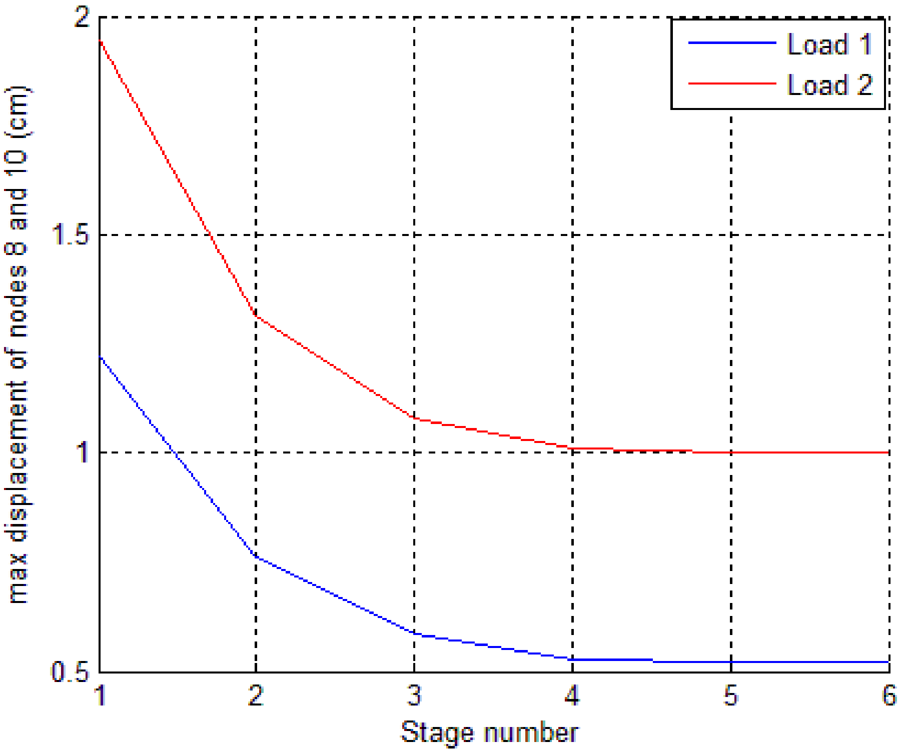

Fig. 18. Maximum displacement variation of nodes for two load cases of a 52-bar space structure.

6. Conclusion

In this study, a Modified Particle Swarm Optimization (MPSO) algorithm was developed for the shape optimization of truss structures under displacement constraints. The proposed method incorporates a multi-stage search strategy in which the final solution of each stage guides the initial population of the next, effectively improving convergence precision and reducing randomness. To evaluate the performance of the MPSO, four standard benchmark problems were investigated, including planar and spatial truss structures. The results demonstrate that the proposed MPSO achieves competitive or improved solutions in terms of structural weight reduction while satisfying displacement constraints, when compared with existing methods reported in the literature. In all examples, the MPSO not only attained feasible designs with lower structural weights but also showed a stable convergence trend with reduced computational effort. Overall, the MPSO algorithm proves to be an efficient and robust tool for solving shape optimization problems in truss structures, with strong potential for broader applications in structural engineering problems involving complex design constraints.

Statements & Declarations

Author contributions

Seyed Mohammad Seyedpoor: Conceptualization, Methodology, Supervision, Writing - Original Draft.

Morteza Pendashteh: Investigation, Visualization, Validation, Resources, Formal analysis.

Funding

The authors received no financial support for the research, authorship, and/or publication of this article.

Data availability

The data presented in this study will be available on interested request from the corresponding author.

Declarations

The authors declare no conflict of interes.

References

[1] Shemshaki, E., Haddad, M. H., Mashayekhi, M., Aghajanzadeh, S. M., Majdi, A., Noroozinejad Farsangi, E. A Novel Hybrid Metaheuristic MPA-PSO to Optimize the Properties of Viscous Dampers. Buildings, 2025; 15: doi:10.3390/buildings15081330.

[2] Lambora, A., Gupta, K., Chopra, K. Genetic Algorithm- A Literature Review. In: International Conference on Machine Learning, Big Data, Cloud and Parallel Computing (COMITCon); 2019 Feb 14-16; Faridabad, India. p. 380-384. doi:10.1109/COMITCon.2019.8862255.

[3] Babu, B. V., Jehan, M. M. L. Differential Evolution for Multi-Objective Optimization. In: The 2003 Congress on Evolutionary Computation; 2003 Dec 8-12; Canberra, Australia. p. 2696-2703. doi:10.1109/CEC.2003.1299429.

[4] Fourie, P. C., Groenwold, A. A. The Particle Swarm Optimization Algorithm in Size and Shape Optimization. Structural and Multidisciplinary Optimization, 2002; 23: 259-267. doi:10.1007/s00158-002-0188-0.

[5] Kaveh, A., Talatahari, S. A Hybrid Particle Swarm and Ant Colony Optimization for Design of Truss Structures. Asian journal of civil engineering, 2008; 9: 329-348. doi:10.1260/026635108786260956.

[6] Selvi, V., Umarani, R. Comparative Analysis of Ant Colony and Particle Swarm Optimization Techniques. International Journal of Computer Applications, 2010; 5: 1-6. doi:10.5120/908-1286.

[7] Mashayekhi, M., Shirpour, A., Sadeghi, R. Finding Optimum Parameters of Passive Tuned Mass Damper by PSO, WOA, and Hybrid PSO-WOA (HPW) Algorithms. Journal of Soft Computing in Civil Engineering, 2023; 7: 72-92. doi:10.22115/scce.2023.352340.1489.

[8] Lamberti, L. An Efficient Simulated Annealing Algorithm for Design Optimization of Truss Structures. Computers & Structures, 2008; 86: 1936-1953. doi:10.1016/j.compstruc.2008.02.004.

[9] Kirkpatrick, S., Gelatt, C. D., Vecchi, M. P. Optimization by Simulated Annealing. Science, 1983; 220: 671-680. doi:10.1126/science.220.4598.671.

[10] Rajeev, S., Krishnamoorthy, C. S. Discrete Optimization of Structures Using Genetic Algorithms. Journal of Structural Engineering, 1992; 118: 1233-1250. doi:10.1061/(ASCE)0733-9445(1992)118:5(1233).

[11] Goldberg, D. E. Genetic Algorithms in Search, Optimization, and Machine Learning. 1st ed. Boston (MA): Addison-Wesley; 1989.

[12] Wang, D., Zhang, W. H., Jiang, J. S. Truss Shape Optimization with Multiple Displacement Constraints. Computer Methods in Applied Mechanics and Engineering, 2002; 191: 3597-3612. doi:10.1016/S0045-7825(02)00297-9.

[13] Lee, K. S., Geem, Z. W. A New Structural Optimization Method Based on the Harmony Search Algorithm. Computers & Structures, 2004; 82: 781-798. doi:10.1016/j.compstruc.2004.01.002.

[14] Toğan, V., Daloğlu, A. T. Optimization of 3D Trusses with Adaptive Approach in Genetic Algorithms. Engineering Structures, 2006; 28: 1019-1027. doi:10.1016/j.engstruct.2005.11.007.

[15] Salajegheh, E., Mashayekhi, M., Khatibinia, M., Kaykha, M. Optimum Shape Design of Space Structures by Genetic Algorithm. International Journal of Space Structures, 2009; 24: 45-57. doi:10.1260/026635109788251502.

[16] Cheng, J. Optimum Design of Steel Truss Arch Bridges Using a Hybrid Genetic Algorithm. Journal of Constructional Steel Research, 2010; 66: 1011-1017. doi:10.1016/j.jcsr.2010.03.007.

[17] Kaveh, A., Talatahari, S. An Enhanced Charged System Search for Configuration Optimization Using the Concept of Fields of Forces. Structural and Multidisciplinary Optimization, 2011; 43: 339-351. doi:10.1007/s00158-010-0571-1.

[18] Kennedy, J., Eberhart, R. Particle Swarm Optimization. In: Proceedings of ICNN'95 - International Conference on Neural Networks; 1995 Nov 27- Dec 1; Perth, Australia. p. 1942-1948. doi:10.1109/ICNN.1995.488968.

[19] Seyedpoor, S. M., Gholizadeh, S., Talebian, S. R. An Efficient Structural Optimisation Algorithm Using a Hybrid Version of Particle Swarm Optimisation with Simultaneous Perturbation Stochastic Approximation. Civil Engineering and Environmental Systems, 2010; 27: 295-313. doi:10.1080/10286600902998526.

[20] Luh, G.-C., Lin, C.-Y. Optimal design of truss-structures using particle swarm optimization. Computers & Structures, 2011; 89: 2221-2232. doi:10.1016/j.compstruc.2011.08.013.

[21] Gholizadeh, S. Layout optimization of truss structures by hybridizing cellular automata and particle swarm optimization. Computers & Structures, 2013; 125: 86-99. doi:10.1016/j.compstruc.2013.04.024.

[22] Kaveh, A., Zolghadr, A. Democratic PSO for truss layout and size optimization with frequency constraints. Computers & Structures, 2014; 130: 10-21. doi:10.1016/j.compstruc.2013.09.002.

[23] Mortazavi, A., Toğan, V. Simultaneous size, shape, and topology optimization of truss structures using integrated particle swarm optimizer. Structural and Multidisciplinary Optimization, 2016; 54: 715-736. doi:10.1007/s00158-016-1449-7.

[24] Cao, H., Qian, X., Chen, Z., Zhu, H. Enhanced particle swarm optimization for size and shape optimization of truss structures. Engineering Optimization, 2017; 49: 1939-1956. doi:10.1080/0305215X.2016.1273912.

[25] Tsiptsis, I. N., Liimatainen, L., Kotnik, T., Niiranen, J. Structural optimization employing isogeometric tools in Particle Swarm Optimizer. Journal of Building Engineering, 2019; 24: 100761. doi:10.1016/j.jobe.2019.100761.

[26] Jafari, M., Salajegheh, E., Salajegheh, J. Optimal design of truss structures using a hybrid method based on particle swarm optimizer and cultural algorithm. Structures, 2021; 32: 391-405. doi:10.1016/j.istruc.2021.03.017.

[27] Seyedpoor, S. M., Salajegheh, J., Salajegheh, E., Gholizadeh, S. Optimal design of arch dams subjected to earthquake loading by a combination of simultaneous perturbation stochastic approximation and particle swarm algorithms. Applied Soft Computing, 2011; 11: 39-48. doi:10.1016/j.asoc.2009.10.014.

Civil Engineering and Applied Solutions, 2025; 1(3): 17–28

Civil Engineering and Applied Solutions

Research Article

journal homepage: ceas.journals.umz.ac.ir

Prediction of Rice Husk Ash-Based SCC Compressive Strength: Data-Driven Framework

Hamid Farrokh Ghatte [a*], Ali Nazari [b]

[a] *Department of Civil Engineering, University of Antalya Bilim, Antalya, Turkey*
[b] *Department of Civil Engineering, Sharif University of Technology, Tehran, Iran*

ARTICLE INFO

Keywords:
Prediction
Self-compacting concrete (SCC)
Gene expression programming (GEP)
Machine learning algorithms

Article history:
Received 07 July 2025
Accepted 13 July 2025
Available online 01 August 2025

ABSTRACT

The construction and upkeep of concrete structures have posed significant technical and financial challenges over the past decade. In response, self-compacting concrete (SCC) has gained attention due to its superior mechanical performance and reduced environmental footprint. This study investigates the application of gene expression programming (GEP) in developing a predictive model for estimating the compressive strength (CS) of self-compacting concrete incorporating rice husk ash (RHA). To assess the model's reliability, its predictions were benchmarked against those from two well-established machine learning methods: multiple linear regression (MLR) and artificial neural networks (ANN). A total of 651 experimental records related to RHA-based SCC were gathered from trustworthy references. The model's performance was then quantified using key statistical measures, including the correlation coefficient (R), root mean squared error (RMSE), and mean absolute error (MAE). The GEP model outperformed the ANN and MLR approaches, delivering greater accuracy and lower error levels. Additionally, the study introduced a gene expression-based formula derived from the GEP model for estimating compressive strength at different curing ages, achieving a correlation coefficient of 0.49 and error values ranging from 5 to 9 MPa, which highlights its strong predictive ability. This equation provides a practical tool for preliminary mix design and the quick assessment of SCC mixtures. Sensitivity analysis revealed that binder content was the most significant parameter influencing CS prediction.

1. Introduction

Self-compacting concrete (SCC) is regarded as one of the breakthroughs in modern concrete engineering practices. As a relatively recent innovation in construction materials, emerging over the past three decades, SCC was made possible by the development of superplasticizers as a new class of admixtures. SCC is a type of concrete with medium to high strength that can spread solely by the force of gravity, completely occupying the formwork without requiring external vibration [1]. In the early 1980s, the increasing complexity of construction projects in Japan, combined with the growing volume of reinforcement, led to poor compaction and decreased execution quality [2]. Given the rising global population and growing human needs, the generation of industrial and agricultural waste is increasing steadily. The construction industry presents a valuable opportunity to utilize such waste materials. This research investigates the application of rice husk a byproduct of agriculture and its ash, which serves as a pozzolanic substance abundant in reactive silica, for potential use in construction materials. Appropriately processed rice husk ash (RHA) has been shown to enhance the durability of concrete against aggressive environments, reduce reinforcement corrosion, and play a significant role in soil stabilization, cementitious block production, and the fabrication of lightweight insulating concrete and bricks [3, 4].

---

* Corresponding author.
E-mail addresses: ghatte@itu.edu.tr (H. Farrokh Ghatte).

https://doi.org/10.22080/ceas.2025.29625.1025
ISSN: 3092-7749/© 2025 The Author(s). Published by University of Mazandaran.
This article is an open access article distributed under the terms and conditions of the Creative Commons Attribution (CC-BY) license (https://creativecommons.org/licenses/by/4.0/deed.en)
How to cite this article: Farrokh Ghatte, H., Nazari, A. Prediction of Rice Husk Ash-Based SCC Compressive Strength: Data-Driven Framework. Civil Engineering and Applied Solutions. 2025; 1(3): 17-28. doi:10.22080/ceas.2025.29625.1025.

In recent years, the emergence of new materials and technologies has introduced a larger number of parameters into concrete mix design, sometimes doubling the number of influencing variables. Consequently, data-driven modeling approaches, particularly those built on experimental data, have attracted significant interest among researchers. Classical modeling methods such as multiple linear regression (MLR) and artificial neural networks (ANNs) have been widely used to solve problems in concrete technology. For instance, Chen and Pai [5] used MLR to predict compressive strength based on physical properties, analyzing various input variable combinations, and reporting results using statistical performance indicators. The capability of ANNs to predict concrete properties has also been assessed in several studies. Sonebi et al. [6] and Kalman Šipoš et al. [7] reported that ANN models could serve as effective alternatives to laboratory testing for estimating both fresh and hardened properties of concrete. Similarly, Wang et al. [8] applied both ANN and MLR methods to model the behavior of concrete and presented their results through statistical analyses.

However, classical data-driven methods often fail to provide explicit predictive equations from the model outputs. Therefore, modern modeling techniques like GEP, which can deliver accurate and interpretable mathematical expressions, have gained attention among researchers [9]. As an illustration, Gholampour et al. [10] utilized datasets related to recycled concrete to construct predictive models using GEP, aiming to estimate key mechanical properties such as compressive strength, tensile strength, and elastic modulus.

In recent years, while many studies have focused on applying machine learning techniques such as multiple linear regression and artificial neural networks for predicting the compressive strength of various types of concrete, limited research has been conducted on the use of GEP for modeling the compressive strength of self-compacting concrete incorporating rice husk ash. Moreover, previous studies have often relied on relatively small datasets or lacked explicit predictive equations that can be directly used for practical mix design. These limitations underscore the need for more comprehensive modeling approaches that provide both high predictive accuracy and interpretable formulations.

The novel contributions of the present study can be summarized as follows:

- Development of a GEP-based predictive model for estimating the compressive strength of SCC containing rice husk ash, trained and validated on an experimental dataset.
- Comprehensive comparison of GEP performance with conventional models (MLR and ANN) to highlight its advantages in terms of accuracy and interpretability.
- Derivation of an explicit mathematical equation from the GEP model to facilitate practical use in preliminary concrete mix design.
- Sensitivity analysis to identify the most influential parameters affecting compressive strength prediction.

2. Methodology

2.1. Multiple linear regression (MLR)

Regression analysis is a statistical approach used to explore how a dependent variable responds to changes in one or more independent variables, while holding others constant. This method provides insights into the nature and strength of these relationships. Typically, regression analysis aims to construct a mathematical model that relates independent variables to the prediction of a dependent variable’s value [11, 12]. Today, regression analysis is widely used for predictive modeling. Among various techniques available, linear regression and least squares regression are among the most commonly applied. According to Sobhani et al. [13] linear regression is a form of regression analysis that models the relationship between one or more independent variables and a dependent variable using a linear regression equation. In contrast, the goal of nonlinear regression is to find a suitable nonlinear equation that fits the relationship.

2.2. Artificial neural networks (ANNs)

The artificial neural network (ANN) model known as the perceptron was introduced by Frank Rosenblatt in 1958 [14]. These networks typically consist of three layers: input, hidden, and output. In feedforward neural networks, input signals propagate forward from the input layer through the hidden layers to the output layer [15]. The quantity of neurons in the input and output layers is directly aligned with the number of corresponding input and output variables. There is no definitive rule for determining the number of neurons in the hidden layer; this is generally determined based on problem complexity and through trial and error [16]. To minimize the error, the weights between neurons are updated in a backward direction from the output layer toward the input layer, and this process is repeated iteratively until the desired output is achieved.

2.3. Gene expression programming (GEP)

Gene expression programming (GEP), developed by Ferreira in 1999 [17], is a variant of genetic algorithms that evolves solutions by evaluating individuals through a fitness function and applying genetic operations via one or more operators. While similar in concept to genetic algorithms, which operate on binary strings, GEP differs in that it uses tree-based structures to generate optimal solutions [18]. Ferreira incorporated various operators in GEP, such as mutation and crossover. One of the key features of these operators is their ability to avoid producing invalid individuals by applying error-free operations. GEP utilizes different types of crossover mechanisms, including one-point, two-point, and gene crossover [17]. Among these, the two-point crossover is considered more effective as it enables more frequent activation and deactivation of non-coding regions within chromosomes. GEP represents various phenomena by employing predefined sets of functions and terminal symbols. In this study, the GeneXpro Tools 5.0 software was employed to implement the GEP model. To better illustrate the modeling approach employed in this research, a workflow diagram has been provided in Fig. 1. This flowchart depicts the key steps, including dataset compilation, preprocessing, selection of input parameters, model development using MLR, ANN, and GEP techniques, performance evaluation with statistical metrics, and sensitivity analysis to identify the most influential factors affecting compressive strength prediction.

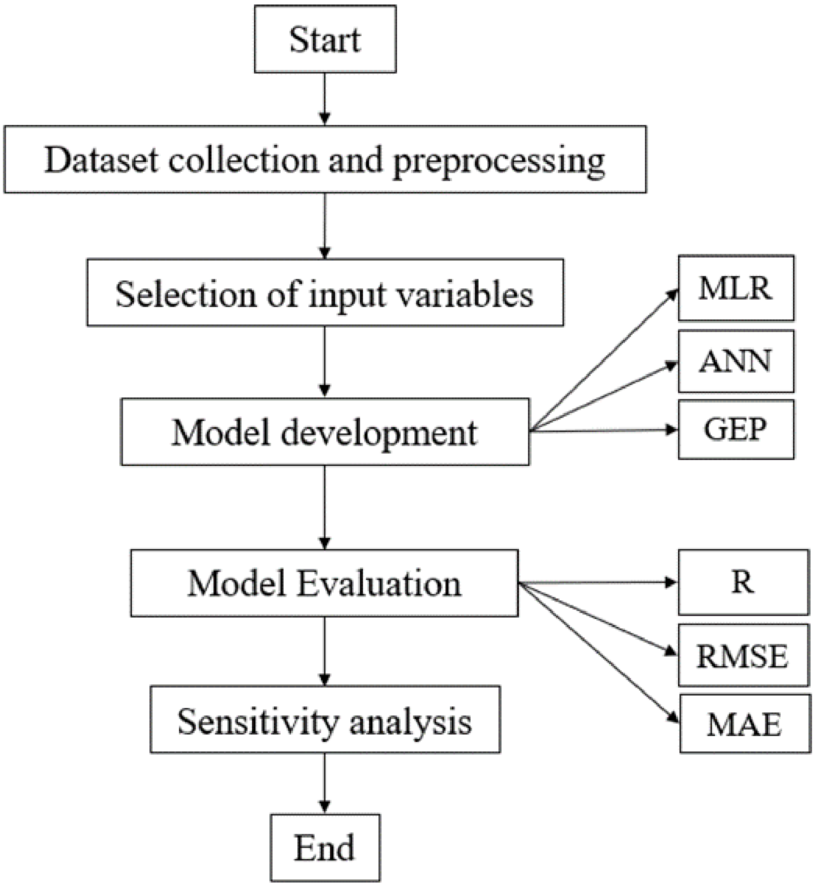

Fig. 1. Workflow of the computational modeling framework adopted in this study.

3. Dataset used in this study

To estimate the CS of SCC incorporating RHA using data-driven models, a comprehensive dataset was collected from various experimental studies. This dataset consists of 156 data points obtained from different laboratory tests related to the CS of SCC incorporating RHA, compiled from previous studies [19-22]. The dataset was split into training and testing subsets, with 75% allocated for model training and the remaining 25% reserved for evaluation. All samples were designed using different combinations of the following materials: fine aggregate (FA), coarse aggregate (CA), cement (C), rice husk ash (RHA), superplasticizer (SP), and water (W). The numerical surveys informed the success in simulating different problems using an ANN [23, 24]. On the other hand, the structural behavior of RC elements and beam-column joints, as well as retrofitting approaches by employing SCC and/or normal concrete, have been additionally investigated through cyclic or monotonic loadings [25-27].

To account for differences in mix proportions and testing conditions, the dataset includes concrete compressive strength values measured at 7, 28, and 90 days under standard curing conditions. The measured CS (MPa) served as the output variable (target), while the seven aforementioned components acted as the input variables. As this dataset was compiled from a variety of published research, it represents a valuable and credible source for modeling purposes. To assess the consistency and distribution characteristics of the data, statistical evaluations were carried out. Table 1 reports the range, mean, standard deviation, and coefficient of variation for each variable. Table 2 outlines the error metrics used to assess the models' predictive accuracy.

Table 1. Summary of descriptive statistics for the considered variables.

Variables	C	W	FA	CA	RHA	AS	SP	CS
Max	560	341	814	1319	135	90	7.33	106.5
Min	0	119	539	995	0	1	0	16.5
Mean	441.54	162.1	608.3	1250	53.1	59.19	4.68	28.92
std dev	58.9	13.95	100.28	92.8	37.1	23.8	93.2	33.89

Table 2. Applied performance evaluation metrics to the models.

No.	Equation
(1)	$R = \frac{\sum_{i=1}^{M}(O_i-\overline{O}).(P_i-\overline{P})}{\sqrt{\sum_{i=1}^{M}(O_i-\overline{O})^2\sum_{i=1}^{M}(P_i-\overline{P})^2}}$
(2)	$\text{RMSE} = \frac{\sum_{i=1}^{M}(P_i-O_i)^2}{M}$
(3)	$\text{MAE} = \frac{\sum_{i=1}^{M}\lvert P_i-O_i\rvert}{M}$

4. Comparison and evaluation of proposed models

To compare the performance of the proposed models during the training and testing phases, statistical indices including the correlation coefficient (R), root mean square error (RMSE), and mean absolute error (MAE) were used, as presented in Table 2. In these equations, Oi represents the observed values, Pi denotes the predicted values, $\overline{O}$ is the mean of observed values, $\overline{P}$ is the mean of predicted values, and M is the total number of data points.

Additionally, the developed models were compared and evaluated against other data-driven models reported by previous researchers. Specifically, the compressive strength prediction models of Belalia Douma et al. [28], Kaveh et al. [29], Inqiad et al. [30], and Siddique et al. [31] were examined, and their performance was compared with the GEP-based model proposed in this study.

5. Results and discussion

5.1. Determining the optimal input combination for developing predictive models

In this study, an effort was made to identify the best combination of input parameters for developing predictive models. Various combinations of input parameters were tested, and the proposed models were developed accordingly. It should be noted that the parameters were assessed both individually and in combination.

To determine the optimal combination, previous literature and experimental data were reviewed, and different groupings of parameters were analyzed. Based on model performance results, the following input configuration was selected as the best-performing scenario:

1. Compressive strength as the output, and the following as inputs:

Water (W), Cement (C), Fine aggregate (FA), Coarse aggregate (CA), Rice husk ash (RHA), and Superplasticizer (SP).

2. W/C, FA/C, CA/C, SP, and RHA content.

3. W/FA, FA/C, CA/C, SP, and RHA content.

4. W/CA, FA/C, CA/C, SP, and RHA content.

In this study, MLR was used to determine the best combination of input variables for predicting compressive strength. The goal was to select the optimal input set for model development using statistical regression techniques. MLR is known for its simplicity and interpretability and is widely used in preliminary modeling when dealing with real datasets.

The very low error associated with this method suggests that MLR can be reliably used in early-stage model selection before adopting more complex nonlinear algorithms. Among the four tested combinations (shown in Table 3), the fourth input set consisting of W/CA, FA/C, CA/C, SP, and RHA content resulted in the best prediction accuracy.

Table 3. Assessment of suggested scenarios for identifying the optimal set of input variables.

Imput	R	RMSE	MAE
Scenario -1	0.92	6.41	7.71
Scenario -2	0.9	7.49	8.1
Scenario -3	0.83	10.2	11.29
Scenario -4	0.86	9.31	9.6

This configuration achieved an R of 0.92 and the lowest RMSE of 6.41 MPa in predicting compressive strength, indicating its superior predictive performance. Furthermore, when this optimal input set was tested using the ANN and GEP models, the results confirmed its higher reliability compared to the other three input combinations, as illustrated in Fig. 2.

5.2. ANN model for predicting concrete strength

After identifying the best combination of input variables for estimating the CS of SCC with RHA, the ANN modeling process was initiated. A multilayer feedforward ANN architecture was utilized in this study. The quantity of neurons in the hidden layer significantly influences the model's overall performance. To identify the most suitable number of neurons, different values were tested in a trial-and-error process. In this study, a single hidden-layer architecture was used, as prior research has shown it to be sufficient for capturing complex nonlinear relationships [11-13].

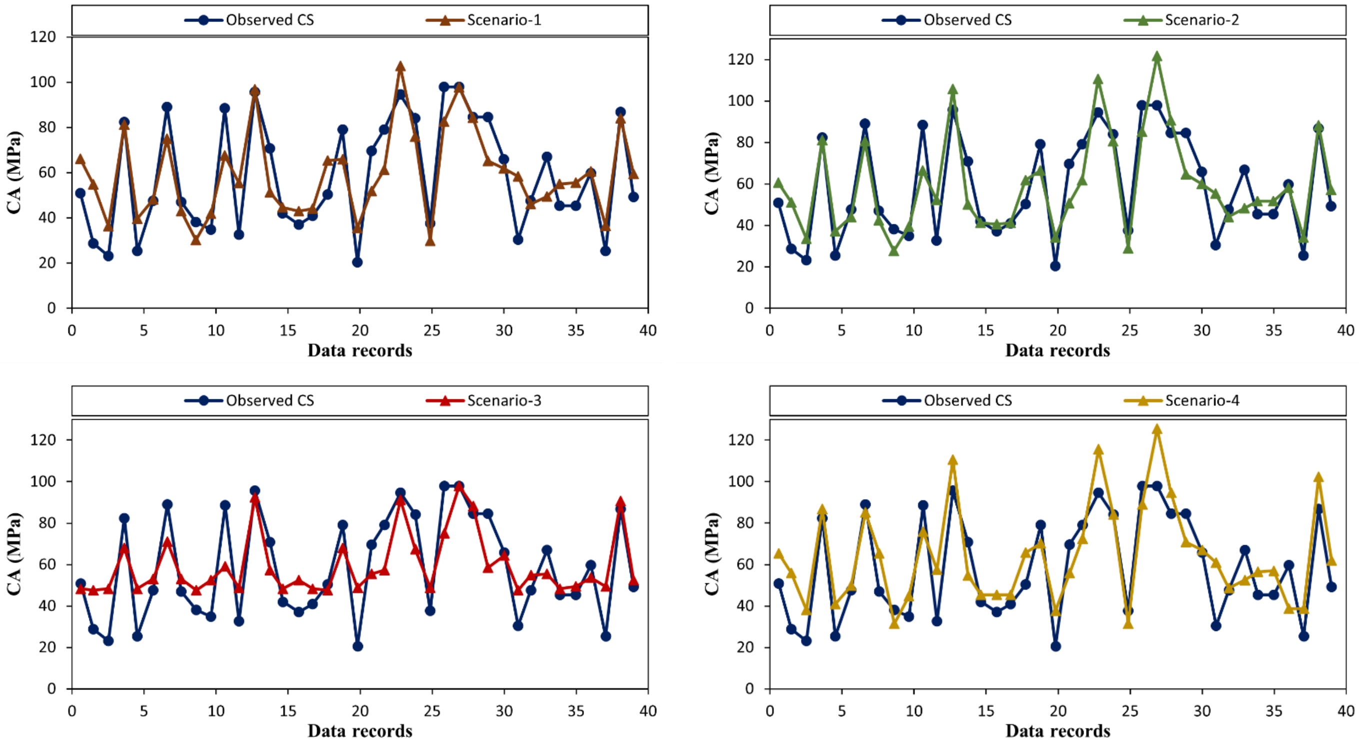

Fig. 2. Time series diagrams corresponding to the suggested alternatives.

The Levenberg–Marquardt (trainlm) algorithm was used for training, given its high efficiency and minimal prediction error. Additionally, the sigmoid transfer function was employed in both the hidden and output layers, which has proven effective in previous studies. For training and testing the networks, 90% (141 samples) and 20% (31 samples) of the data were used, respectively, and the performance of each phase is reported in Table 4. The performance of the ANN model during both phases was evaluated using the same statistical indicators (R, RMSE, and MAE). Fig. 3 illustrates the evaluation metrics for each artificial neural network model in a graphical format. Among the different configurations tested, the optimal ANN model had 5 neurons in the hidden layer, a learning rate of 0.01, a momentum coefficient of 0.9, and was trained for 2000 epochs. It is important to mention that increasing the number of neurons in the hidden layer beyond a certain limit led to overfitting and reduced generalization capability. The best-performing ANN model, as noted, consisted of a single hidden layer with 5 neurons and 2000 training iterations. In this study, ten different ANN configurations (ANN 1 to ANN 10) were developed by systematically varying the number of neurons in the hidden layer from 1 to 10. Each ANN model in Table 4 corresponds to a specific configuration with a distinct number of hidden neurons. This approach allowed us to evaluate the impact of the network complexity on prediction accuracy and to identify the optimal architecture providing the best performance metrics.

Table 4. Performance metrics of ANN models during training and testing phases.

Models	Training			Testing		
	R	RMSE	MAE	R	RMSE	MAE
ANN 1	0.69	15.6	16.6	0.6	15.6	16.6
ANN 2	0.73	11.2	12.8	0.79	13.3	14
ANN 3	0.94	5.3	5.9	0.92	7.5	8.3
ANN 4	0.95	4.5	5.1	0.93	5.1	5.6
ANN 5	0.92	5.4	5.8	0.92	6.4	6.9
ANN 6	0.93	5.8	6.7	0.92	6.9	7.5
ANN 7	0.94	4.9	5.4	0.9	7.1	7.9
ANN 8	0.92	6.46	7.5	0.85	9.9	10.2
ANN 9	0.93	6.34	7.6	0.86	8.5	9.5
ANN 10	0.86	9.76	10.9	0.83	1.9	11.5

5.3 GEP model for predicting concrete strength

In this study, GEP was used to predict the CS of self-compacting concrete containing RHA. The model was developed based on a set of initial input parameters, from which the algorithm started its search, and ultimately generated an explicit mathematical expression for the output. As presented in Table 5, the values assigned to each parameter in the GEP model are shown. This provides a straightforward and interpretable expression that connects mix design parameters with CS.

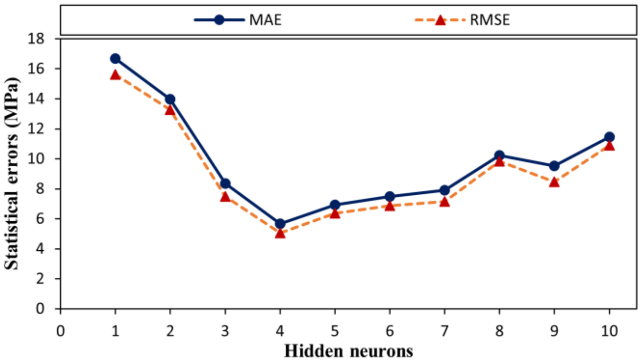

Fig. 3. Assessment of hidden layer neuron counts in ANN configurations.

The final equation, derived using the GEP approach, provides a reliable and practical tool for predicting the compressive strength of SCC incorporating rice husk ash. For the prediction of compressive strength of concrete containing rice husk ash, the optimal number of individuals per generation was set to 30 chromosomes, and the best fitness value achieved was 633.68. Fig. 4 presents the prediction deviations of the GEP model in comparison to the experimentally obtained CS values of self-compacting concrete. A higher model accuracy is indicated by data points clustering near the zero-error line. As shown, most of the errors lie within the interval of -8 to +8 MPa.

Table 5. Optimal configuration parameters for the GEP model.

Parameter details		Parameter details	
Function set	+, –, /, exp, power	Gene transposition rate	0.277
Mutation rate	0.044	Head size	7
Inversion rate	0.3	Number of genes	4
One/two-point recombination rate	0.3	Number of chromosomes	30
Gene recombination rate	0.1		

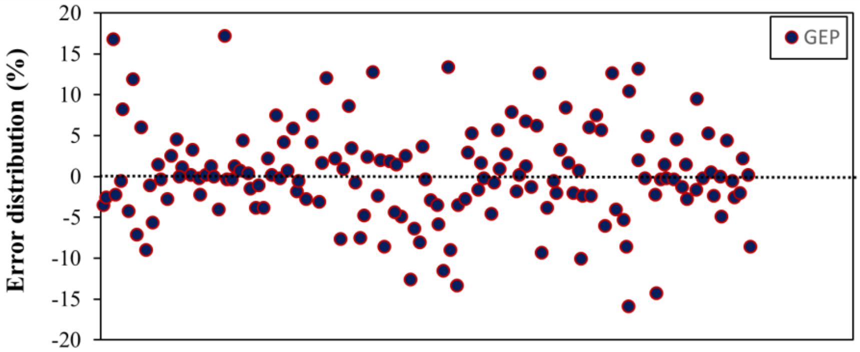

Fig. 4. Distribution of prediction errors in the GEP model.

Based on previous studies and through a process of trial and error, the optimal combination of input parameters for predicting the compressive strength of concrete containing rice husk ash was identified. According to Table 5 and the structure shown in Fig. 5, the GEP-based model was developed using a selection of parameters that significantly influence the target output. The notations used are: d0 = C, d1 = RHA, d2 = W, d3 = SP, d4 = FA, d5 = CA, and d6 = AS. The final input configuration selected C, W, RHA, SP, FA, CA, and AS, indicating that rice husk ash content, water-to-cement ratio, and superplasticizer dosage are the most influential variables, along with the type and size of aggregates and curing age.

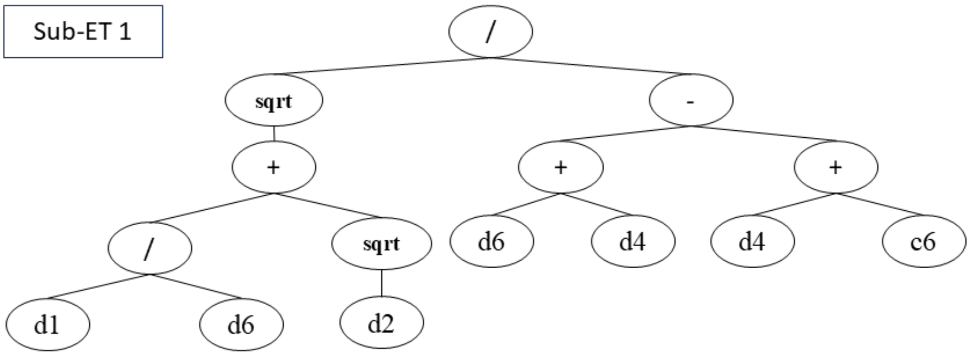

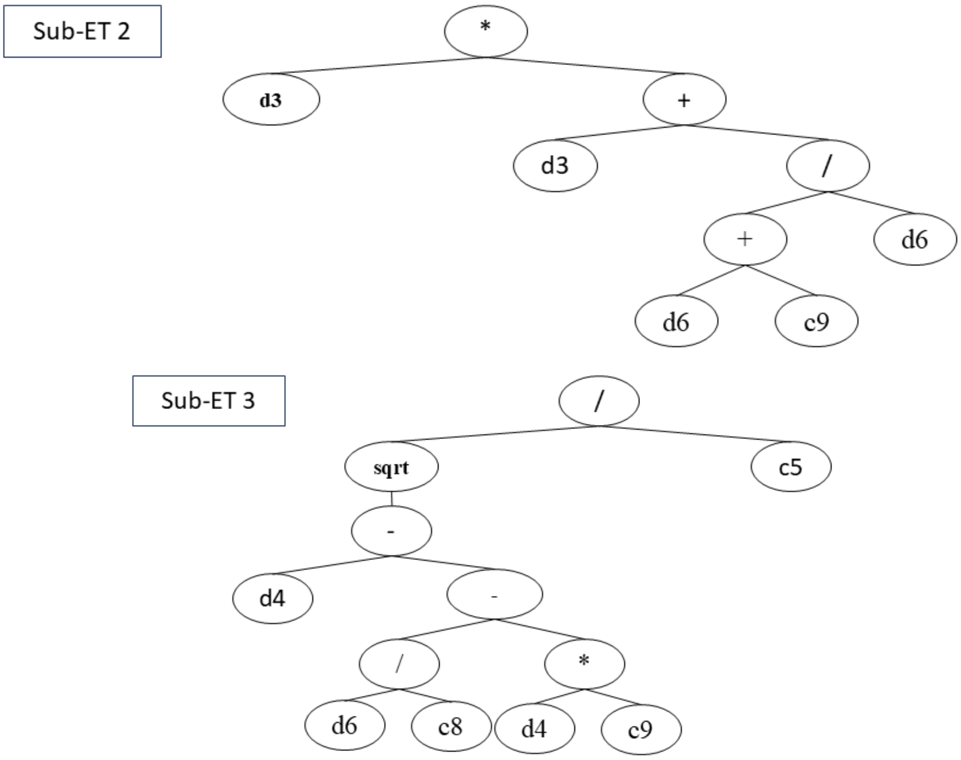

Fig. 5. Expression tree of GEP model.

Finally, the best predictive equation for estimating the CS of SCC with RHA, based on the optimal combination of input parameters, is expressed through Eq. (1).

$$\mathrm{CS} = \left\{\left(\left(\frac{RHA}{C}\right) + W^{0.5}\right)^{0.5} \times \left((AS+FA) - (FA+3.49)^{-1}\right)\right\} + \left\{SP \times \left(CA + (AS-7.26)\right)\right\} + \left\{\left(FA + \left(\frac{AS}{0.234}\right) - 7.9AS\right)^{0.5} + 6.8\right\} \tag{1}$$

As shown in Table 6, the R in the training phase for MLR, ANN, and GEP models was 0.92, 0.95, and 0.98, respectively. The RMSE values were 6.4, 4.5, and 3.9, and the MAE values were 7.8, 5.1, and 5.4, respectively. These results indicate that the GEP model outperformed ANN and MLR in terms of prediction accuracy.

The ranking of models based on error metrics shows that GEP had the highest accuracy and required less training time compared to ANN. This suggests that GEP is a more efficient and reliable approach, particularly when interpretability of the prediction model is important. Considering the mathematical structure of the GEP-derived equation and the strong consistency between predicted and observed values, it can be inferred that the GEP model delivers highly precise outcomes, with prediction errors remaining within acceptable limits.

Table 6. Comparative analysis of developed models for predicting the CS of SCC.

Models	Training			Testing		
	R	RMSE	MAE	R	RMSE	MAE
MLR	0.92	6.4	7.8	0.9	8.2	9.5
ANN	0.95	4.5	5.1	0.93	5.1	5.6
GEP	0.98	3.9	5.4	0.95	4.3	4.9
Belalia Douma et al. [28]	0.95	-	-	0.94	-	-
Kaveh et al. [29]- a	0.95	5.2	5.1	0.95	6.8	5.5
Kaveh et al. [29] - b	0.96	4.5	3.5	0.94	4.5	5.6
Inqiad et al. [30]	0.22	733	23.1	0.33	4.5	5.6
Siddique et al. [31]	-	-	-	0.91	4.43	5.6

In this study, Fig. 6 illustrates the observed and predicted compressive strength values, as estimated by the proposed MLR, ANN, and GEP models during the training phase. A comparative qualitative assessment shows that the GEP method more accurately tracks the observed compressive strength values. In contrast, the MLR model tends to diverge from the data points, especially in regions with high error. The GEP method exhibits greater consistency and lower dispersion around the regression line, focusing on a denser clustering of points near the actual values. The MLR model, on the other hand, displays a wider spread in the error range, indicating reduced accuracy in certain regions. Fig. 7 further confirms that the GEP model yields predictions that are more closely aligned with experimental results. Additionally, it was observed that during the testing phase, the GEP model achieved lower error values compared to ANN, highlighting the superior accuracy of gene expression programming over artificial neural networks in this case.

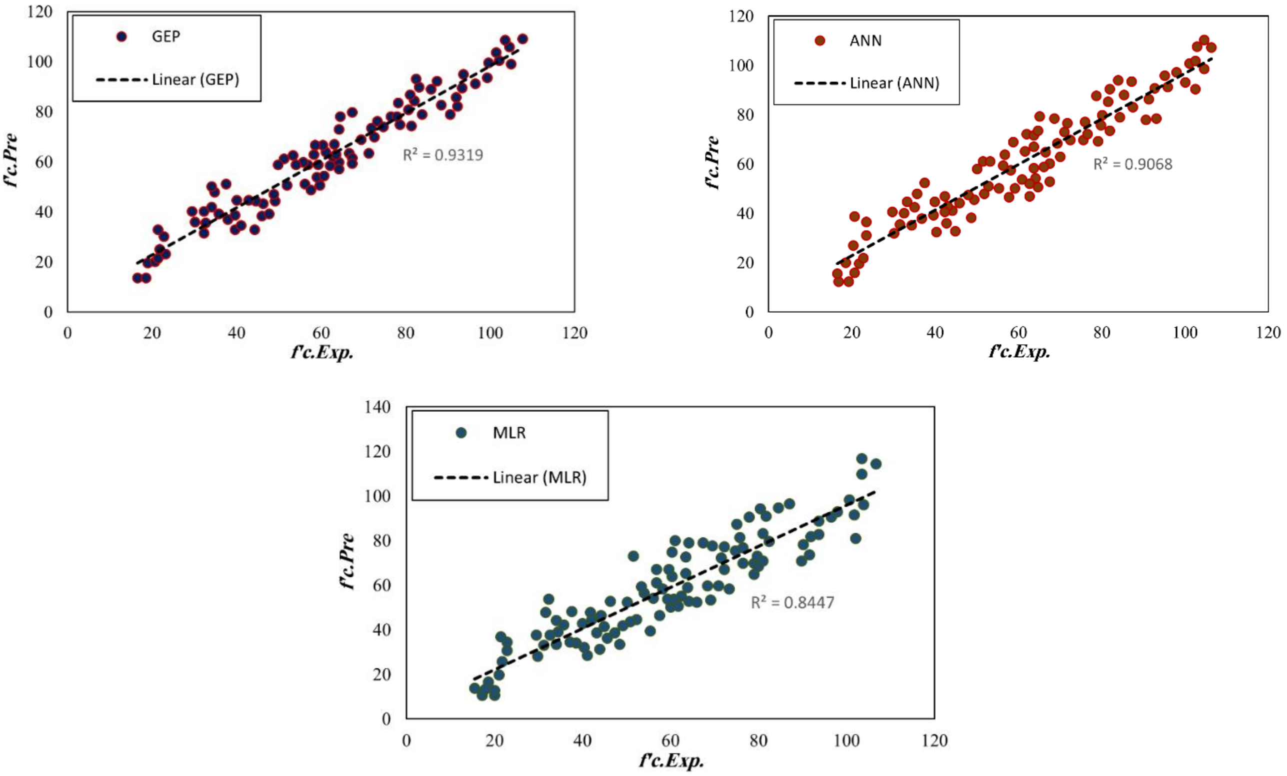

Fig. 6. Scatterplots of the developed models for training performance.

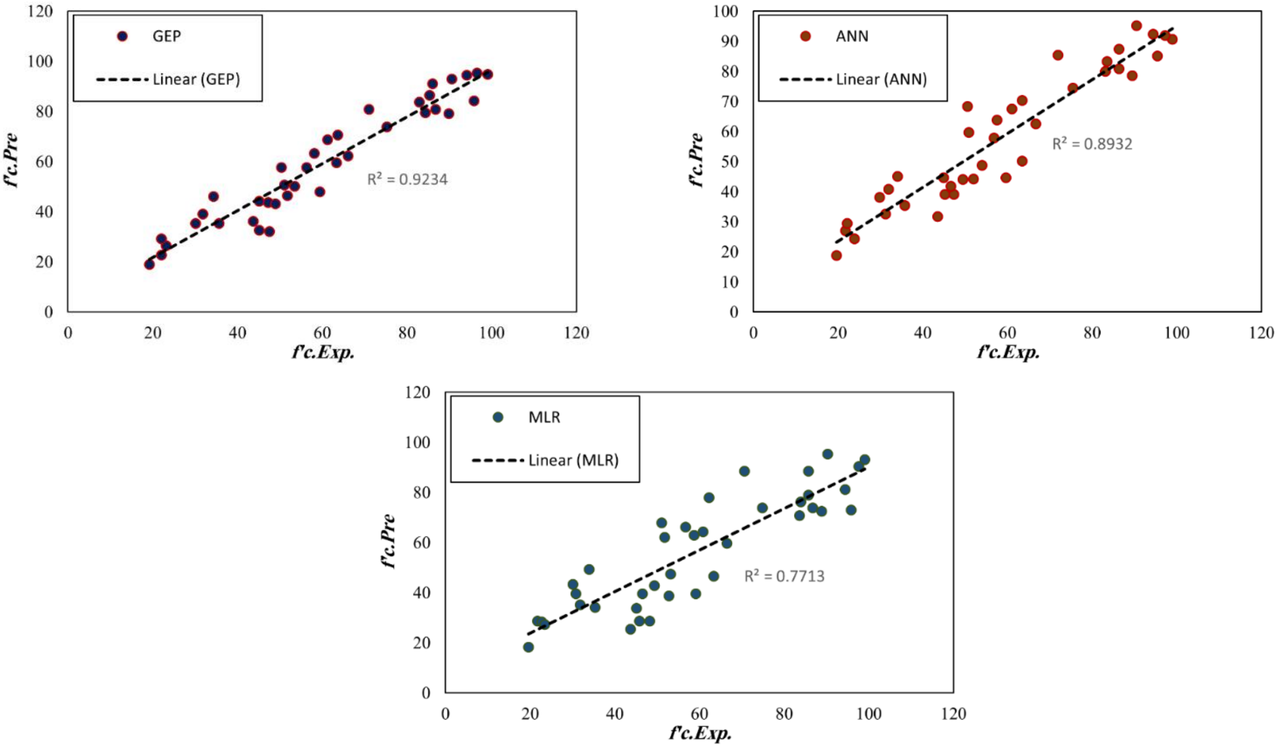

Fig. 7. Scatterplots of the developed models for testing performance.

Traditional approaches like ANNs and MLR were employed in this research to estimate the CS of SCC incorporating RHA. From a comparative standpoint, the quantitative evaluation results shown in Fig. 8 indicate that the proposed methods outperform traditional approaches. The GEP method, in particular, exhibited greater accuracy and lower error dispersion than the MLR model. Because linear regression cannot model intricate nonlinear patterns, it failed to reliably predict and generalize compressive strength values over the full spectrum of the dataset. On the other hand, the GEP-based model provided more accurate predictions and minimized the deviation from experimental results, especially when determining the influence of multiple variables. Additionally, previous studies [23] have emphasized that methods such as ANN are highly sensitive to the number of variables and input conditions, which may lead to instability in model behavior. Therefore, based on the results of Fig. 8, it can be concluded that the GEP method offers higher predictive performance for compressive strength estimation compared to both ANN and MLR.

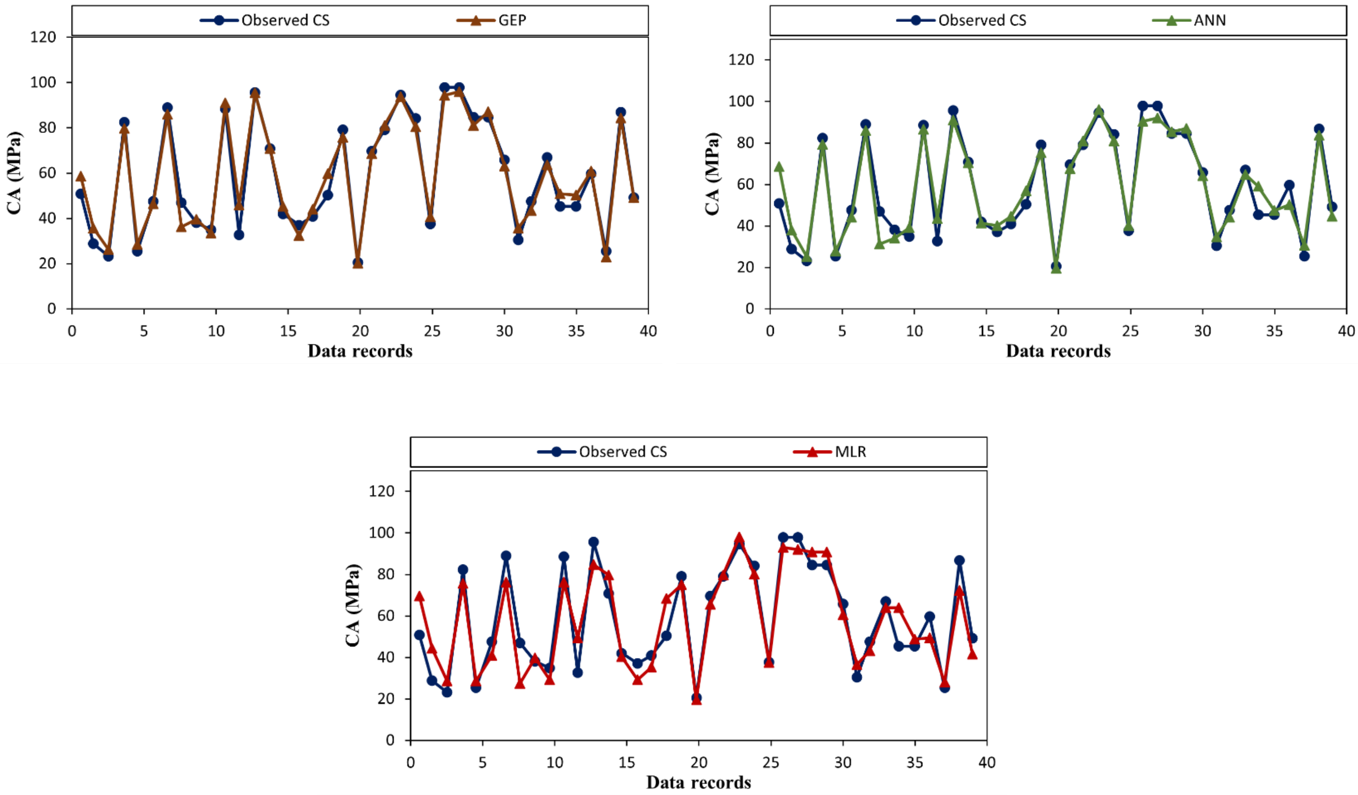

Fig. 8. Time series plots of model performance in the testing phase.

In this study, classical data-driven methods such as ANN and MLR encountered computational errors due to the trial-and-error nature of network optimization and their limited ability to address complex problems involving a large number of variables affecting the physical behavior of different systems [23]. Therefore, the use of metaheuristic algorithms has become essential for improving these methods and other predictive approaches. According to the timeline chart illustrated in Fig. 8, the CS predictions made using the MLR method demonstrated relatively weaker performance compared to the ANN and GEP models in predicting the CS of SC with RHA. The quantitative comparison shown in Fig. 8 confirms that the MLR method produced relatively inaccurate predictions and failed to effectively estimate both the maximum and minimum local values of compressive strength. The highest prediction errors were observed in the 40–60 MPa range, where the predicted values were generally lower than the experimentally measured compressive strengths. This highlights the MLR model's inability to capture the nonlinear relationships involved in concrete strength development when using supplementary cementitious materials like rice husk ash.

5.4. Assessment of the relevance of the developed regression models

To test the significance of the regression coefficients, statistical testing using the F-value can be employed as follows:

H_0: $\beta_1 = \beta_2 = \cdots = \beta_k = 0 \rightarrow$ the regression model is not significant.

H_1: $\beta_i \neq 0 : i = 1, 2, \ldots, k \rightarrow$ the regression model is significant.

If all the regression coefficients are equal to zero, this would indicate that there is no linear relationship between the independent variables and the dependent variable. In that case, the model would be deemed statistically insignificant. If the result of the test indicates that at least one coefficient differs from zero, the regression model is considered significant. To test the significance of the regression model, the confidence level must be determined first. In this study, a 95% confidence level was selected, which means the probability of rejecting the null hypothesis should be less than 0.05. The critical value for model significance evaluation using the Fisher test [24] is determined based on Table 7. It should be noted that the F-test results reported in Table 8 were obtained based on the training dataset. The F-statistic and p-values were calculated in Python using the statsmodels library, which provides an automated regression analysis. This library computes the regression sum of squares, residual sum of squares, mean squares, and finally the F-value, following standard statistical procedures. In the results of model significance testing, the p-value is reported. If the p-value is less than the significance level (0.05), the null hypothesis is rejected, and the model is considered statistically significant. Also, as shown in the Table of statistical analysis results, the reported p-values are all less than 0.05, which confirms the significance of the regression model. Furthermore, the F-value reported is higher than the critical value (9.16), indicating a strong model fit.

Table 7. F-test outcomes for the developed models.

Model	F-value	P-value
GEP	22.11	0.0088
ANN	15.1	0.02
MLR	8.4	0.38

5.5. Sensitivity analysis

Sensitivity analysis refers to the study of how the input variables of a statistical model influence its output. In other words, it is a systematic method of varying the inputs of a model to predict the effects of these changes on the model's output [25]. In this research, sensitivity analysis was conducted using the GEP approach, which showed the highest accuracy among all developed models to evaluate the impact of each input variable on the predicted CS of SCC incorporating RHA.

The results presented in Table 8 indicate that the parameter cement (C), with a correlation coefficient of R = 0.73 and other statistical indicators (RMSE = 10.4, MAE = 11.3), has the greatest influence on predicting the compressive strength of concrete. The parameter aggregate size (AS) also shows a high correlation with compressive strength, with a correlation coefficient of R = 0.93, and statistical indicators (RMSE = 4.2, MAE = 4.2) demonstrating its strong predictive influence.

Table 8. Sensitivity analysis of input variables for predicting CS.

Imput	R	RMSE	MAE
CS = *f*(W, SP, FA, CA, AS, RHA)	0.73	10.4	11.3
CS = f(C, SP, FA, CA, AS, RHA)	0.89	5.3	6.1
CS = f(C, W, FA, CA, AS, RHA)	0.92	4.2	4.2
CS = f(C, W, SP, CA, AS, RHA)	0.9	4.7	5.3
CS = f(C, W, SP, FA, AS, RHA)	0.79	9.7	10.4
CS = f(C, W, SP, FA, CA, RHA)	0.93	4.2	4.2
CS = f(C, W, SP, FA, CA, AS)	0.82	7.7	7.8

These findings confirm that cement and aggregate size are the two most influential parameters in determining the CS of SCC incorporating RHA [32-34]. In contrast, other input variables W, RHA, CA, FA, and SP had comparatively less influence. Overall, the sensitivity analysis revealed that cement and aggregate size are the dominant factors affecting the compressive strength of SCC with RHA.

6. Conclusion

In this study, one of the most advanced data-driven techniques, GEP, was employed to predict the CS of SCC incorporating RHA. To identify the most influential parameters affecting the compressive strength of this concrete type, four input scenarios were defined, and each case was evaluated using MLR. Ultimately, seven input parameters (C, AS, CA, FA, SP, W, and RHA) and one output parameter (concrete compressive strength) were used to develop the proposed models.

Based on the evaluation of the developed models, the following conclusions were drawn:

1. The performance of the proposed intelligent models was assessed for both training and testing phases using experimental data collected from previous studies. According to the statistical error indicators in the training phase, the GEP model (R = 0.97, RMSE = 3.364) outperformed the Artificial Neural Network model (R = 0.94, RMSE = 4.536) and the Multiple Linear Regression model (R = 0.91, RMSE = 6.762) in predicting the compressive strength of SCC. Furthermore, performance evaluation in the testing phase showed that the GEP model (R = 0.97, RMSE = 3.308) provided more accurate predictions under nonlinear formulations compared to the ANN (R = 0.92, RMSE = 5.136) and MLR (R = 0.89, RMSE = 9.212) models for the 21-day compressive strength of SCC containing RHA.

2. The GEP and ANN models, used as explicit equations for estimating the compressive strength of SCC, demonstrated significantly higher accuracy compared to traditional linear methods. In particular, GEP, with its capability to formulate precise output estimations, proved to be a powerful tool for prediction and data mining in engineering technologies, especially in concrete technology.

3. The statistical significance of the proposed models was verified using regression hypothesis testing through the Fisher test, showing that the F-values for all models were below the critical threshold and the confidence levels were less than 0.05, thereby validating the reliability of the developed models.

4. To assess the sensitivity of the output variable to the input variables, the GEP method was used. The results indicated that variable C had the most substantial effect on predicting compressive strength, whereas SP exhibited the least influence on the model’s output.

5. Based on the results of the sensitivity analysis and the performance of the developed models, the optimal RHA content for

achieving higher compressive strength in self-compacting concrete mixtures was found to be approximately 10–15% by weight of the binder.

Statements & Declarations

Author contributions

Hamid Farrokh Ghatte: Conceptualization, Validation, Visualization, Writing - review & editing.

Ali Nazari: Validation, Software, Resources, Methodology, Investigation, Formal analysis, Data curation, Writing - Original Draft.

Funding

The authors received no financial support for the research, authorship, and/or publication of this article.

Data availability

The data presented in this study will be available on interested request from the corresponding author.

Declarations

The authors declare no conflict of interes.

References

[1] Sandhu, R. K., Siddique, R. Influence of rice husk ash (RHA) on the properties of self-compacting concrete: A review. Construction and Building Materials, 2017; 153: 751-764. doi:10.1016/j.conbuildmat.2017.07.165.

[2] Ameri, F., Shoaei, P., Bahrami, N., Vaezi, M., Ozbakkaloglu, T. Optimum rice husk ash content and bacterial concentration in self-compacting concrete. Construction and Building Materials, 2019; 222: 796-813. doi:10.1016/j.conbuildmat.2019.06.190.

[3] Sutas, J., Mana, A., Pitak, L. Effect of Rice Husk and Rice Husk Ash to Properties of Bricks. Procedia Engineering, 2012; 32: 1061-1067. doi:10.1016/j.proeng.2012.02.055.

[4] Qu, J., Li, B., Wei, T., Li, C., Liu, B. Effects of rice-husk ash on soil consistency and compactibility. CATENA, 2014; 122: 54-60. doi:10.1016/j.catena.2014.05.016.

[5] Chen, L., Pai, T. Y. An ERAFNN Prediction of Concrete Compressive Strength Based on Physical Properties of Electric Arc Furnace Oxidizing Slag. Applied Mechanics and Materials, 2014; 627: 111-114. doi:10.4028/www.scientific.net/AMM.627.111.

[6] Sonebi, M., Grünewald, S., Cevik, A., Walraven, J. Modelling fresh properties of self-compacting concrete using neural network technique. Computers and Concrete, 2016; 18: 903-921. doi:10.12989/cac.2016.18.4.903.

[7] Kalman Šipoš, T., Miličević, I., Siddique, R. Model for mix design of brick aggregate concrete based on neural network modelling. Construction and Building Materials, 2017; 148: 757-769. doi:10.1016/j.conbuildmat.2017.05.111.

[8] Wang, B., Man, T., Jin, H. Prediction of expansion behavior of self-stressing concrete by artificial neural networks and fuzzy inference systems. Construction and Building Materials, 2015; 84: 184-191. doi:10.1016/j.conbuildmat.2015.03.059.

[9] Rezaei, F., Memarzadeh, A., Davoodi, M.-R., Dashab, M.-A., Nematzadeh, M. Mechanical features and durability of concrete incorporating recycled coarse aggregate and nano-silica: Experimental study, prediction, and optimization. Journal of Building Engineering, 2023; 73: 106715. doi:10.1016/j.jobe.2023.106715.

[10] Gholampour, A., Gandomi, A. H., Ozbakkaloglu, T. New formulations for mechanical properties of recycled aggregate concrete using gene expression programming. Construction and Building Materials, 2017; 130: 122-145. doi:10.1016/j.conbuildmat.2016.10.114.

[11] Nematzadeh, M., Nazari, A., Tayebi, M. Post-fire impact behavior and durability of steel fiber-reinforced concrete containing blended cement–zeolite and recycled nylon granules as partial aggregate replacement. Archives of Civil and Mechanical Engineering, 2021; 22: 5. doi:10.1007/s43452-021-00324-1.

[12] Nematzadeh, M., Tayebi, M., Samadvand, H. Prediction of ultrasonic pulse velocity in steel fiber-reinforced concrete containing nylon granule and natural zeolite after exposure to elevated temperatures. Construction and Building Materials, 2021; 273: 121958. doi:10.1016/j.conbuildmat.2020.121958.

[13] Sobhani, J., Najimi, M., Pourkhorshidi, A. R., Parhizkar, T. Prediction of the compressive strength of no-slump concrete: A comparative study of regression, neural network and ANFIS models. Construction and Building Materials, 2010; 24: 709-718. doi:10.1016/j.conbuildmat.2009.10.037.

[14] Rosenblatt, F. The perceptron: a probabilistic model for information storage and organization in the brain. Psychological review, 1958; 65: 386. doi:10.1037/h0042519.

[15] Augustino, D. S. Parametric Modelling of Fibre-Concrete Interface and Prediction of Compressive Strength of Concrete With Waste Tyre Steel Fibres Using Artificial Neural Network Model. Advances in Civil Engineering, 2025; 2025: 7678622. doi:10.1155/adce/7678622.

[16] Marimuthu, V., Ramasamy, A. Mechanical characteristics of waste-printed circuit board-reinforced concrete with silica fume and prediction modelling using ANN. Environmental Science and Pollution Research, 2024; 31: 28474-28493. doi:10.1007/s11356-024-33099-y.

[17] Ferreira, C. Gene expression programming: a new adaptive algorithm for solving problems. arXiv preprint cs/0102027, 2001; doi:10.48550/arXiv.cs/0102027.

[18] Shahmansouri, A. A., Akbarzadeh Bengar, H., Jahani, E. Predicting compressive strength and electrical resistivity of eco-friendly concrete containing natural zeolite via GEP algorithm. Construction and Building Materials, 2019; 229: 116883. doi:10.1016/j.conbuildmat.2019.116883.

[19] Sakr, K. Effects of silica fume and rice husk ash on the properties of heavy weight concrete. Journal of materials in civil engineering, 2006; 18: 367-376. doi:10.1061/(ASCE)0899-1561(2006)18:3(367).

[20] Ganesan, K., Rajagopal, K., Thangavel, K. Rice husk ash blended cement: Assessment of optimal level of replacement for strength and permeability properties of concrete. Construction and Building Materials, 2008; 22: 1675-1683. doi:10.1016/j.conbuildmat.2007.06.011.

[21] Bui, D. D., Hu, J., Stroeven, P. Particle size effect on the strength of rice husk ash blended gap-graded Portland cement concrete. Cement and Concrete Composites, 2005; 27: 357-366. doi:10.1016/j.cemconcomp.2004.05.002.

[22] Rodríguez de Sensale, G. Strength development of concrete with rice-husk ash. Cement and Concrete Composites, 2006; 28: 158-160. doi:10.1016/j.cemconcomp.2005.09.005.

[23] Shahmansouri, A. A., Yazdani, M., Hosseini, M., Akbarzadeh Bengar, H., Farrokh Ghatte, H. The prediction analysis of compressive strength and electrical resistivity of environmentally friendly concrete incorporating natural zeolite using artificial neural network. Construction and Building Materials, 2022; 317: 125876. doi:10.1016/j.conbuildmat.2021.125876.

[24] Shahmansouri, A. A., Yazdani, M., Ghanbari, S., Akbarzadeh Bengar, H., Jafari, A., Farrokh Ghatte, H. Artificial neural network model to predict the compressive strength of eco-friendly geopolymer concrete incorporating silica fume and natural zeolite. Journal of Cleaner Production, 2021; 279: 123697. doi:10.1016/j.jclepro.2020.123697.

[25] Ghatte, H. F. Evaluation of reinforcing bars ratio effects on SCC beam-column joint performance. Uludağ Üniversitesi Mühendislik Fakültesi Dergisi, 2019; 24: 141-152. doi:10.17482/uumfd.587505.

[26] Farrokh Ghatte, H. External steel ties and CFRP jacketing effects on seismic performance and failure mechanisms of substandard rectangular RC columns. Composite Structures, 2020; 248: 112542. doi:10.1016/j.compstruct.2020.112542.

[27] Farrokh Ghatte, H. Failure mechanisms and cracking performance of T-shaped SCC beam-column connections at top floor: Test results and FE modeling. Structures, 2020; 28: 1009-1018. doi:10.1016/j.istruc.2020.09.051.

[28] Belalia Douma, O., Boukhatem, B., Ghrici, M., Tagnit-Hamou, A. Prediction of properties of self-compacting concrete containing fly ash using artificial neural network. Neural Computing and Applications, 2017; 28: 707-718. doi:10.1007/s00521-016-2368-7.

[29] Kaveh, A., Bakhshpoori, T., Hamze-Ziabari, S. M. M5'and Mars based prediction models for properties of self-compacting concrete containing fly ash. Periodica Polytechnica Civil Engineering, 2018; 62: 281-294. doi:10.3311/PPci.10799.

[30] Inqiad, W. B., Siddique, M. S., Ali, M., Najeh, T. Predicting 28-day compressive strength of fibre-reinforced self-compacting concrete (FR-SCC) using MEP and GEP. Scientific Reports, 2024; 14: 17293. doi:10.1038/s41598-024-65905-5.

[31] Siddique, R., Aggarwal, P., Aggarwal, Y. Prediction of compressive strength of self-compacting concrete containing bottom ash using artificial neural networks. Advances in Engineering Software, 2011; 42: 780-786. doi:10.1016/j.advengsoft.2011.05.016.

[32] Zhang, W. G., Goh, A. T. C. Multivariate adaptive regression splines for analysis of geotechnical engineering systems. Computers and Geotechnics, 2013; 48: 82-95. doi:10.1016/j.compgeo.2012.09.016.

[33] Bluman, A. G. Elementary statistics: a step by step approach. 11th ed. New York (NY): McGram-Hill; 2019.

[34] Najafzadeh, M., Rezaie Balf, M., Rashedi, E. Prediction of maximum scour depth around piers with debris accumulation using EPR, MT, and GEP models. Journal of Hydroinformatics, 2016; 18: 867-884. doi:10.2166/hydro.2016.212.

Civil Engineering and Applied Solutions, 2025; 1(3): 29–47

Civil Engineering and Applied Solutions

Research Article

journal homepage: ceas.journals.umz.ac.ir

CEAS Civil Engineering and Applied Solutions

Cyclic Behavior of Embedded Column-to-Foundation Connections in Circular CFST Columns: An Experimental and Numerical Study

Saleh Mohammad-Ebrahimzadeh-Sepasgozar [a*], Morteza Naghipour [a]

[a] *Faculty of Civil Engineering, Babol Noshirvani University of Technology, Babol, Iran*

ARTICLE INFO

Keywords:
Embedded connection
CFST column
Cyclic behavior
Axial load
Seismic performance
Energy dissipation

Article history:
Received 08 July 2025
Accepted 21 July 2025
Available online 01 August 2025

ABSTRACT

This study investigates the cyclic performance of embedded column-to-foundation connections in circular concrete-filled steel tube (CFST) columns through experimental testing and numerical simulations. While base-plate connections are commonly used in composite structures, embedding the column into the foundation provides notable advantages, including increased strength, stiffness, and ductility under seismic loading. Experimental results confirmed that embedded connections are capable of fully transferring axial and lateral loads. Failure primarily occurred through plastic hinge formation at the column base, with no evidence of brittle fracture or pull-out. Increasing the embedment depth (Le) significantly enhanced flexural capacity, energy dissipation, and cyclic stability. An embedment depth equal to the column diameter (Le = D) was sufficient to achieve full moment transfer, while deeper embedments (Le > 1.2D) further improved hysteretic behavior and mitigated stiffness degradation at large displacements. The circular geometry of the column, combined with confinement from the surrounding concrete, generated an effective triaxial stress state (i.e., compressive stresses in all three directions) that enhanced mechanical interlock between the steel tube and the concrete core. Numerical simulations corroborated the experimental findings and provided additional insights into stress distribution, confinement effects, and shear transfer mechanisms. Increased friction and contact area within the interaction zone contributed to greater initial stiffness and improved post-yield strength. Parametric analyses revealed that an axial load ratio up to 0.2, particularly in conjunction with high-strength concrete, enhanced seismic performance. However, higher axial ratios (e.g., 0.3) led to local buckling and reduced ductility. For optimal seismic design, it is recommended to embed the column to a depth at least equal to its diameter and maintain the axial load ratio within the range of 0.1 to 0.2.

1. Introduction

Building structures must be capable of transferring both vertical (gravity) and lateral forces to the supporting elements. In most structural systems, the reinforced concrete foundation serves as the primary supporting component [1]. The column base connection is considered the most critical interface between the steel superstructure and the foundation. The performance of steel column base connection details is essential not only for transferring the imposed loads to the foundation but also for ensuring the temporary vertical stability of columns (without lateral bracing) during erection and wind loads encountered during construction. The placement of anchor bolts, as one of the key components for structural safety during erection and accurate positioning of the superstructure, is of vital importance and cannot be overlooked. Column base plates and their corresponding details typically represent the final elements to be designed, but the first to be installed during construction. Fig. 1 illustrates the typical components

---

* Corresponding author.
E-mail addresses: civil.sepasgozar@stu.nit.ac.ir (S. M. Ebrahimzadeh Sepasgozar).

https://doi.org/10.22080/ceas.2025.29629.1027
ISSN: 3092-7749/© 2025 The Author(s). Published by University of Mazandaran.
This article is an open access article distributed under the terms and conditions of the Creative Commons Attribution (CC-BY) license (https://creativecommons.org/licenses/by/4.0/deed.en)
How to cite this article: Ebrahimzadeh Sepasgozar, S. M., Naghipour, M. Cyclic Behavior of Embedded Column-to-Foundation Connections in Circular CFST Columns: An Experimental and Numerical Study. Civil Engineering and Applied Solutions. 2025; 1(3): 29–47. doi:10.22080/ceas.2025.29629.1027.

of a steel column base connection, including the base plate, anchor bars, stiffening gusset plates, welds, connection angles, and grout layer [2]. Many conventional steel base plates have sustained damage during major earthquakes, prompting revisions in design methodologies. Notable seismic events such as the 1978 Iso-Oshima and Miyagi-Ken-Oki earthquakes, as well as the 1995 Kobe earthquake, have highlighted these vulnerabilities.

Previous studies investigating steel column-to-foundation connections have primarily focused on evaluating stiffness, strength, and failure modes. Several notable contributions and research have been published in the literature in this field [3-7]. The widespread damage observed in steel base plates following the 1995 Kobe earthquake prompted Japanese researchers to revisit the design methodology of uncovered base connections. As a result, research efforts concentrated on connections that maintained their strength post-yielding to enhance seismic performance. Hitaka et al. [8], [9] focused specifically on improving the strength, stiffness, and ductility of exposed base connections. In 2004, Marson and Bruneau [10] examined the seismic response of circular CFST column base connections, highlighting the influence of tube cross-sectional geometry. Their specimens exhibited favorable hysteretic behavior and high energy dissipation capacity, with all specimens demonstrating good ductility.

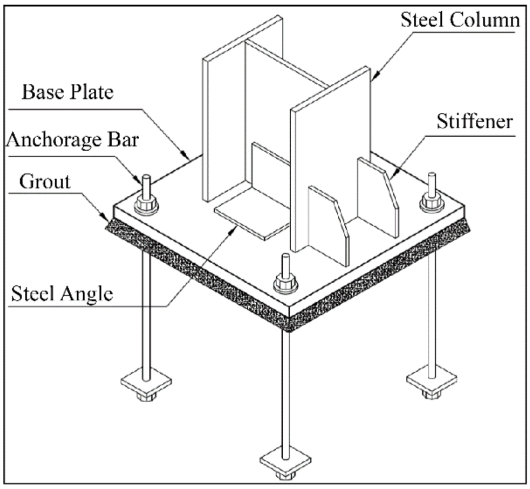

Fig. 1. Configuration of the base plate connection.

Zhang et al. [11] subjected CFST column base specimens encased in concrete to low-cycle seismic loading. Their findings revealed that low-cycle fatigue behavior strongly depended on the steel tube thickness. In 2010, Roeder Charles et al. [12] analyzed circular CFST columns under combined axial and bending loads. Their study presented an effective theoretical model for predicting the stiffness and strength of circular CFST columns, demonstrating that the plastic stress method offered a simple and efficient approach for assessing CFST behavior under combined loading. Between 2012 and 2013, Moon et al. [13], [14, 15] investigated circular CFST columns used in piles, piers, and bridge columns. Specimens were subjected to flexural loading in both experimental and numerical setups, and were evaluated for various diameter-to-thickness ratios. Later in 2013, Moon et al. [15] studied embedded circular CFST column-to-foundation connections under combined axial and flexural loads, followed by Lee et al. [16], who enhanced the punching shear resistance and ductility of foundations and connections using embedded shear-resisting elements. In 2016, Moon et al. [17] further conducted analytical evaluations of reinforced concrete column-to-steel pile connections. Their findings emphasized that embedment depth and the friction coefficient between the infilled concrete and steel pile had a significant impact on the seismic performance of bridge foundations.

While the seismic performance of CFST columns and connections has been rigorously studied in Iran over recent years, limited attention has been given to embedded base connections of CFST members. Despite past research efforts, current structural design literature lacks comprehensive guidelines for embedded base connection design. Furthermore, leading design codes, including Iran's national building regulations, part 10 [18] do not sufficiently address embedded base connection detailing, nor provide modern design provisions. Several studies [19-22] addressed the seismic response of exposed connections between the CFST column and foundation under cyclic loading. The findings demonstrated that the exposed connection failed in the form of concrete crushing, together with the yielding of the base plate and anchor bolt. Many investigations [23-27] examined the lateral shear capacity and load transfer mechanism in the column to foundation connections. The results demonstrated that despite a slight increase in the capacity to carry lateral loads, the energy absorption capacity increased significantly. Other similar research has been conducted on prefabricated column connections to the foundation with sockets, and the results of these studies also demonstrated that when the embedded depth of the column is sufficiently large, the connected members can present suitable hysteresis performance and ultimate failure mode [28, 29].

Other studies by Wang et al. [30] and Zhang et al. [31] on connections of the precast pier to the foundation or cap beam showed that when the embedded depth was 1.13 to 1.5 times the column diameter, plastic damage was concentrated at the bottom of the column. Si et al. [32] and Zhang et al. [33] investigated a novel connection between CFST column-RC footing with shear keys or socket reinforcement and found that the socket depth, longitudinal reinforcement ratio, and axial load ratio significantly affected the mechanical performance of socket connections compared with other parameters. The results demonstrated that damage to specimens was often concentrated at the base of the columns, and the loading capacity slightly increased.

This study aims to experimentally and numerically evaluate the cyclic performance of CFST column-to-foundation embedded connections. The focus lies in identifying and characterizing damage modes observed in specimens under cyclic loading, and tracking relative drift progression until complete failure. Failure scenarios include pull-out, tube yielding, local buckling, initial tearing, and full rupture.

2. Experimental program

2.1. Details of specimens

The experimental investigation was conducted on a circular concrete-filled steel tube (CFST) column embedded in a reinforced concrete foundation. The total height of the column from the top surface of the foundation to the point of lateral load application was 1200 mm. The outer diameter of the steel tube was 240 mm, with a wall thickness of 3.17 mm. The foundation block was constructed with dimensions of 1200 mm in length, 600 mm in width, and 400 mm in height.

The foundation was reinforced with longitudinal deformed bars of 16 mm diameter spaced at 100 mm, while transverse reinforcement was provided using 10 mm diameter stirrups at 100 mm spacing. In the embedded configuration, the bottom end of the CFST column was welded to a circular steel plate (ring-shaped) to ensure uniform transfer of axial and shear forces between the steel tube and the foundation concrete. Fig. 2 presents the construction details of the column-foundation assembly.

The reference specimen used in this study was constructed without internal stiffeners, and the embedment length of the steel tube into the foundation was designed as 1.2 times the outer diameter of the column ($1.2D$). This specimen served as the baseline for evaluating the structural performance of other configurations.

To ensure rotational and translational restraint of the foundation, a high-strength steel confinement frame was designed around it. Additionally, to mitigate potential stress concentrations in the corners and edges of the concrete foundation during loading, two U-shaped steel channels were welded to steel base members anchored to the laboratory floor .For applying cyclic lateral loads at the top of the column and preventing eccentricities or stress concentration during loading, two rigid steel plates were clamped to the column head using high-strength pre-tensioned bolts. Furthermore, to apply constant vertical compression and avoid local crushing at the column top, sufficient reinforcements were incorporated around the column head based on the size of the hydraulic actuator and column diameter, ensuring adequate stiffness. The steel cap plate at the column top had dimensions of (to be specified). The steel cap plate at the column top had dimensions of 400 mm in length, 300 mm in width, and 20 mm in thickness. The effective specimen height was measured from the point of lateral load application down to the top surface of the foundation.

Prior to casting, preparatory steps included leveling the concrete formwork, positioning the steel tube, assembling the reinforcement cage, and placing the concrete mold. To achieve the required embedment depth during casting, four L-shaped steel bars welded to the column base were used to anchor the steel tube within the foundation. Concrete was poured in layers to ensure adequate compaction and complete cavity filling. Since self-compacting concrete (SCC) was used for both the foundation and the steel tube infill, mechanical vibration was not required.

2.2. Material properties

The concrete used for both the column infill and the reinforced concrete foundation was a self-compacting concrete (SCC) mix. The mix proportions are detailed in Table 1. The water content was 190 l/m³, with 790 kg/m³ of sand, 420 kg/m³ of cement, 114 kg/m³ of limestone powder, 805 kg/m³ of coarse aggregate, and 5.5 l/m³ of high-range water-reducing admixture (superplasticizer). In addition, six standard cube specimens (100 mm × 100 mm × 100 mm) and six standard cylindrical specimens (dimensions to be defined) were cast from the same SCC batch to determine the compressive strength at 7 and 28 days. The results of these compressive strength tests are summarized in Table 2 provides a summary of specimen details. All material parameters presented in the table are based on the average values obtained from standardized measurements, as per the relevant test standards [34], and are shown in Fig. 3. The mechanical properties of SCC were determined using standard tests. Cylindrical compressive strength was measured as 39.95 MPa, while the cube compressive strength reached 48.73 MPa. The modulus of elasticity (E_c) was calculated to be 29,705 MPa, and the splitting tensile strength was 2.72 MPa.

Table 1. Mix design proportions for self-compacting concrete (SCC).

Water (l/m³)	Sand (kg/m³)	Cement (kg/m³)	Limestone powder (kg/m³)	Coarse aggregate (kg/m³)	Superplasticizer (l/m³)
190	790	420	114	805	5.5

Table 2. Mechanical properties of SCC.

Test type	Cylinder compressive strength (MPa)	Cube compressive strength (MPa)	Elastic modulus E_c (MPa)	Tensile strength (MPa)
SCC	39.95	48.73	29,705	2.72

The steel tube used in the CFST column was characterized by a yield strength (f_y) ranging from 304.11 MPa to 312.54 MPa, with an average value of 308.43 MPa. The ultimate tensile strength (f_u) ranged between 388.48 MPa and 398 MPa, with an average of 392.34 MPa. For the stress-strain behavior of the steel tube, three dog-bone tests were conducted, and the average mechanical properties were calculated. The three curves are presented in Fig. 3. The ultimate strain at failure (ε_u) was recorded at approximately 26.72%, indicating significant ductility of the steel material. For the A3-grade reinforcement bars used in the foundation, the yield strength was reported as 420 MPa, the ultimate tensile strength was 600 MPa, and the ultimate strain was 24%.

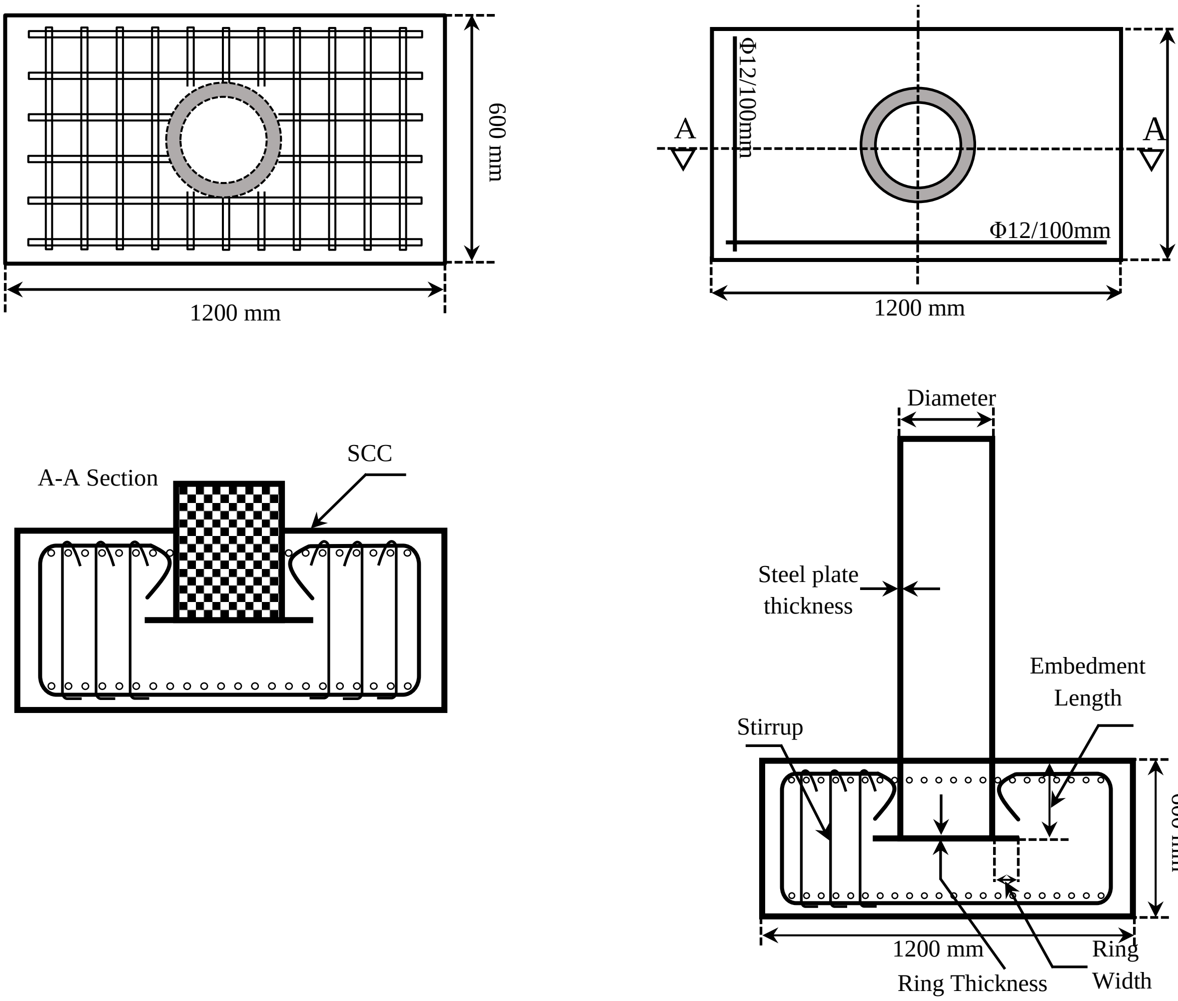

Fig. 2. Detailing and geometric dimensions of the CFST column-to-foundation connection in the embedded condition.

3. Experimental configuration and measurement systems

The tested column-to-foundation connection was subjected to a constant axial compressive load with a ratio of 0.2, alongside cyclic lateral displacement-controlled loading with increasing amplitude. The applied axial force ratio on the test specimen was calculated using the following formula.

$$n = p/p_n \tag{1}$$

In this equation, p represents the actual axial load applied to the top of the column, p_n is the nominal ultimate axial compressive bearing capacity, and n denotes the axial load ratio. The nominal compressive strength p_n of the circular CFST column was calculated in accordance with ACI 318 [34] provisions, as expressed by Eq. 2.

$$p_n = f_y \times A_s + 0.95f'_c \times A_c \tag{2}$$

In this equation, f'_c denotes the standard cylindrical compressive strength of concrete. According to ACI 318 [34] provisions, a conversion factor of 0.79 may be applied to estimate f'_c from compressive strength values obtained using standard cube specimens. The terms A_s and A_s represent the cross-sectional areas of the concrete core and steel tube, respectively. The slenderness ratio of the tested column (*D/t*) falls within the permissible range as defined by relevant design codes, including Iran's national building code [18], and AISC [35]. Following the experimental investigation, a parametric study was conducted, the details of which are presented in the finite element analysis section.

The experimental setup and the location of measurement instruments are depicted in Fig. 4. Axial loading was applied using a 1000 kN hydraulic jack, while the lateral cyclic load was imposed by another 1000 kN hydraulic jack. First, the axial load was applied at the column top to stabilize the specimen, followed by cyclic lateral displacement applied incrementally at the column head. To ensure accurate performance and alignment throughout the test, three hinged connections were incorporated:

- The first hinge was installed at the axial load application point atop the column,

- The second is at the interface of the lateral hydraulic jack and the column,

- And the third at the lateral jack's connection to the reaction frame.

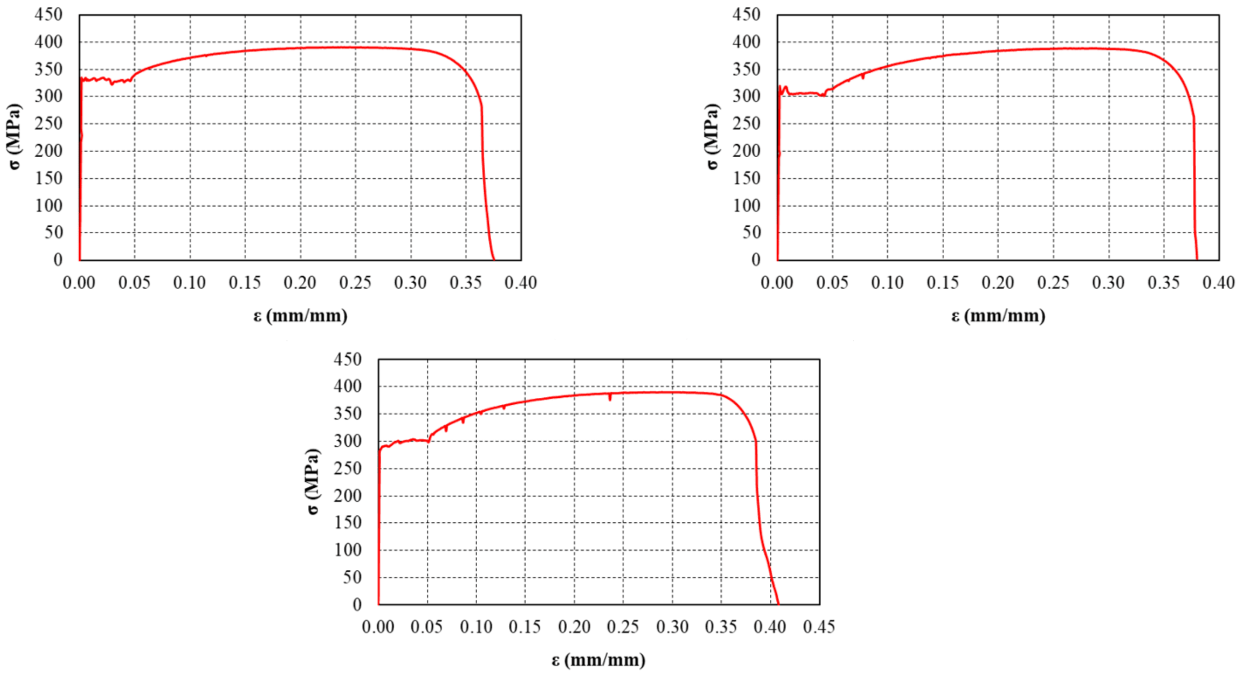

Fig. 3. Stress-strain curve from tensile test of steel tube.

Given that the axial jack was placed above the column, a sliding bearing was used at the interface between the jack and the reaction frame to eliminate unintended horizontal force components. Additionally, to prevent lateral slippage of the foundation during cyclic loading, steel bracing elements were anchored to the strong laboratory floor.

The connection was equipped with linear variable differential transformers (LVDTs) and strain gauges to monitor lateral displacement, support slippage, foundation uplift, and axial strains in the steel tube. The layout of the measurement instrumentation is illustrated in Fig. 4. Two LVDTs were positioned at the column head to measure lateral displacement at the point of load application. Displacement readings from these LVDTs were used to evaluate the hysteretic response of the specimen. Due to the potential for minor gaps between the loading head and the specimen surface, a sudden jump in LVDT values might occur. To counter foundation uplift and account for rotational movement, two additional LVDTs were installed at both ends of the foundation to capture any out-of-plane displacement, even with lateral bracing in place. To monitor localized buckling near the base of the column—a region especially prone to instability—two LVDTs were placed 50 mm above the foundation surface along the direction of lateral loading.

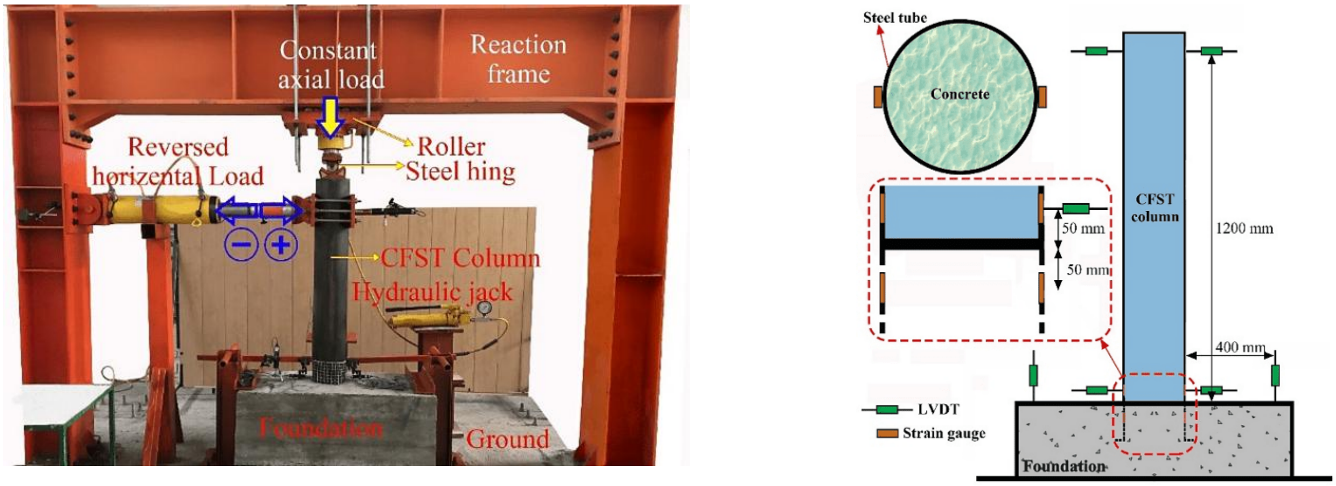

Fig. 4. Schematic of the rigid frame system: support conditions, loading actuators, and measurement systems.

A total of four strain gauges were attached to the steel tube. Two were located 50 mm above the foundation on the external tube surface, and the other two were embedded 50 mm below the surface within the foundation. All instrumentation positions are marked in Fig. 4.

4. Test procedure

Before the application of horizontal cyclic loading, the designated axial compressive load was applied to each specimen. In the initial stage, the axial load was increased at a constant rate of 2 kN/s using a 100 kN capacity axial hydraulic jack. The loading continued until the gap between the vertical loading jack piston and the top surface of the specimen was completely closed, ensuring that no eccentricity was introduced into the setup. Subsequently, a small lateral cyclic load was applied in several forward-reverse cycles to stabilize the test system. Once the setup was fully stabilized, the specimen was subjected to low-cycle lateral loading. The reversed cyclic loading protocol was implemented based on the AISC standard [35], which specifies a displacement-controlled loading scheme with increasing amplitudes and predetermined cycle counts. The applied loading protocol, illustrated in Fig. 5, consisted of incremental displacement cycles. In the first 18 cycles, the applied displacements were maintained below the yield displacement (Δ_y) of the column. Specifically, the first 6 cycles were performed at 0.00375Δ, followed by 6 cycles at 0.005, and then 6 cycles at 0.0075. Next, the displacement amplitude was increased to 0.01 and applied over 4 cycles. Thereafter, loading was continued in two-cycle increments with increasing amplitudes until failure. In the subsequent stages, the first two cycles were carried out at 0.015, followed by two cycles at 0.02. The displacement ratio was then increased by 1% in each stage, with two cycles applied at each level. The cyclic loading was continued until the lateral load-carrying capacity of the system degraded to 85% of its peak lateral strength.

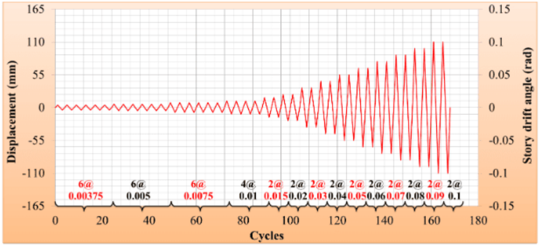

Fig. 5. Cyclic loading protocol.

5. Experimental observations

This section presents an evaluation of visual observations made during testing and the corresponding failure modes. In the tested specimens, plastic hinge formation was concentrated near the foundation at the base of the column. Fig. 6 presents a comparison of hysteresis curves obtained from experimental tests and numerical modeling. Table 3 summarizes the seismic performance parameters of the CFST specimens, comparing experimental and numerical results, including secant stiffness, yield load, maximum load, and yield displacement, ultimate displacement at 85% of peak load, ductility, and energy dissipation. The development of the plastic hinge led to outward bulging and local buckling of the steel tube, accompanied by concrete crushing within the steel tube. Local buckling at the column base was observed when the relative drift reached approximately 1.5% to 3%. At these drift levels, when the lateral load direction was reversed, local buckling in the tensile region tended to recover, while buckling persisted on the compression side. As lateral displacement increased further, local buckling intensified and became irreversible. Fig. 7 illustrates the observed failure patterns in the specimens. Due to the concentration of severe buckling and bulging at the column base, the plastic hinge was not distributed along the column height but was instead confined to a region approximately 25–75 mm above the foundation surface.

Visual inspection confirmed that the most critical damage zones were located within the column itself and not on the foundation surface, occurring at a measurable distance above the foundation. During cyclic testing, the specimens exhibited similar elastic behavior and maintained their ability to return to the original position after initial load applications. Upon entering the plastic stage and the onset of strain hardening, significant deformations appeared in the lower portion of the column near the connection zone. On the compression side, the steel tube showed gradual inward denting, while the tension side displayed signs of elongation and reduced curvature.

Columns with greater embedment depth exhibited smaller drift angles, indicating more stable and ductile flexural behavior. At peak lateral load, no signs of tensile failure or pull-out were observed at the column–foundation interface. The foundation surface also remained free of deep or through-thickness cracks, demonstrating the effectiveness of the embedded connection in transferring forces to the foundation. The use of bent or hooked reinforcement bars at the connection zone played a vital role in resisting tensile forces and maintaining connection integrity. Post-test inspection revealed that the plastic hinge had primarily formed close to the column base, indicating a ductile failure mechanism with gradual degradation. With increased embedment depth, this region shifted upward along the column, and a noticeable reduction in drift angle was recorded. Removal of the steel tube after testing showed minor vertical cracks on the surface of the concrete core and scattered horizontal cracks near the connection zone. These cracks were mainly concentrated near the shoulder or crown region of the cross-section, reflecting the concrete's response to cyclic loading. Overall, the use of embedded steel tubes in CFST columns proved effective in controlling localized deformations at the lower part of the column. However, the concrete core in some specimens exhibited relatively brittle behavior, underscoring the importance of incorporating internal reinforcement or appropriate transverse confinement to improve the cyclic performance of the column.

Table 3. Comparison of seismic performance parameters between experimental and numerical CFST specimens.

Specimen	Secant Stiffness	Yield Load	Maximum Load	Yield Displacement	Ultimate Displacement at 85% Peak Load	Ductility	Energy Dissipation
	K (kN/mm)	**P_y (kN)**	**P_{max} (kN)**	**δ_y (mm)**	**δ_u (kN)**	**μ**	**E (kN.mm)**
CCFC-Exp.	5.01	75.81	84.95	16.95	68.63	4.05	65472.88
CCFC - ABAQUS	5.33	78.80	86.72	16.27	69.38	4.27	68918.83
Percentage Difference	-6.36	-3.95	-2.09	4.01	-1.10	-5.32	-5.26

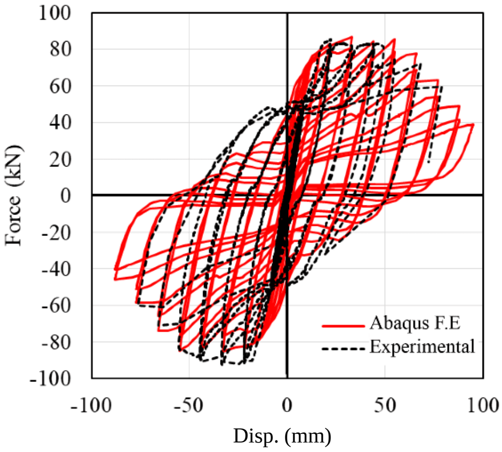

Fig. 6. Comparison of hysteresis curves: experimental vs. numerical model.

6. Numerical modeling

To investigate the nonlinear and cyclic behavior of embedded connections in circular concrete-filled steel tube (CFST) column foundations, the finite element software ABAQUS was employed. The finite element model comprised composite CFST columns, a reinforced concrete foundation, and the embedded connection zone. To improve computational efficiency and reduce analysis time, geometric symmetry with respect to the loading axis was utilized, and a half-symmetric model was developed accordingly.

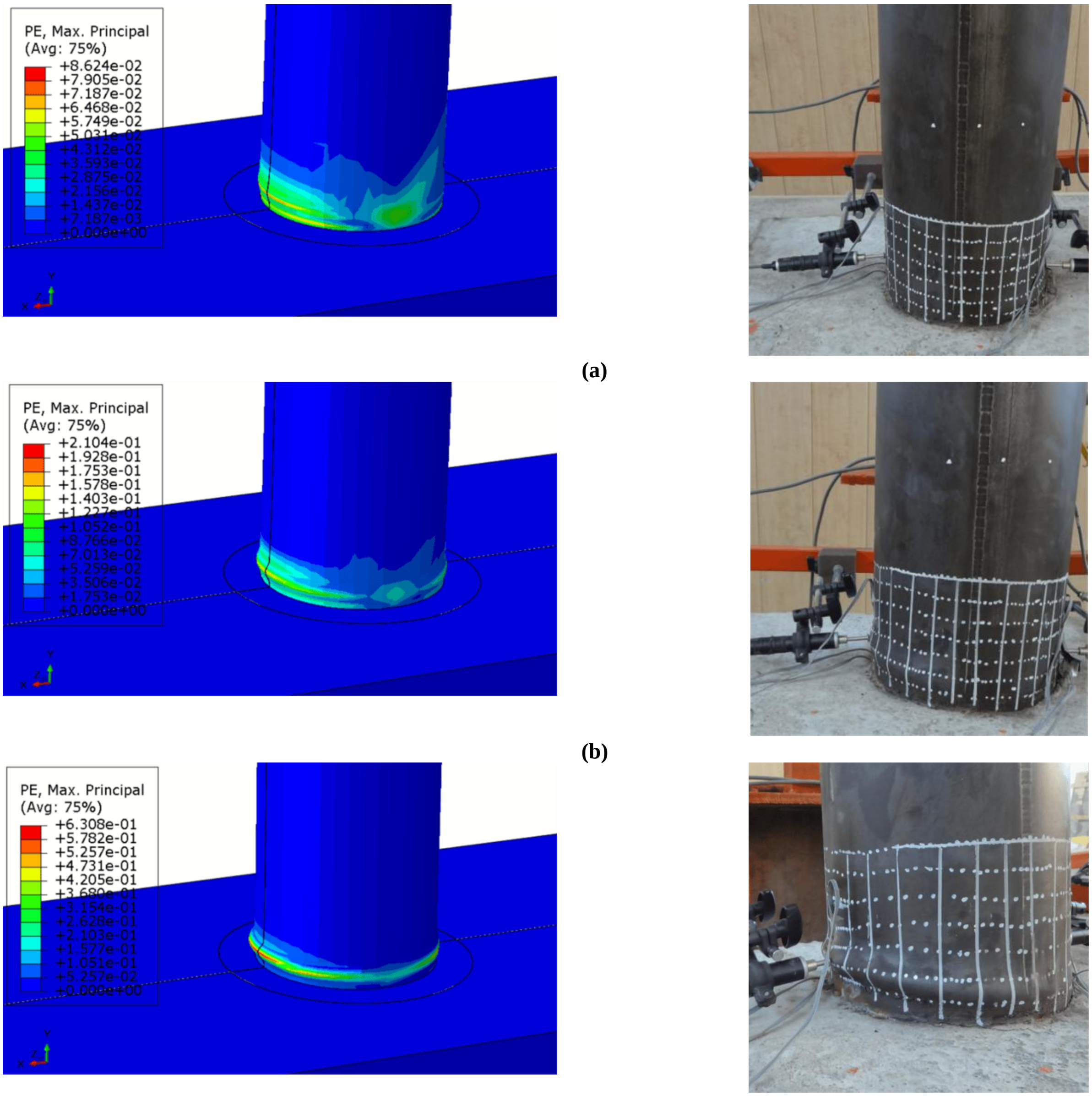

(a)

(b)

(c)

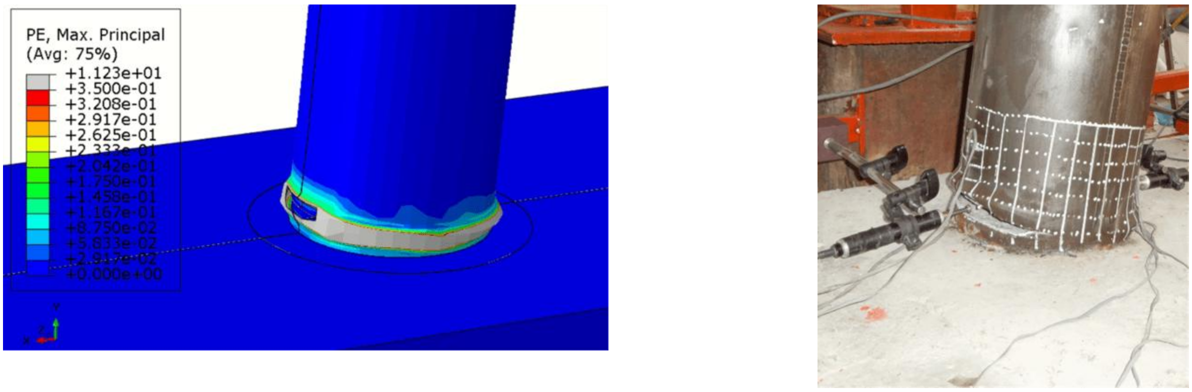

(d)

Fig. 7. Comparison of experimental and simulated damage states (cracking, yielding, and buckling) at incremental drift ratios: (a) 2%, (b) 4%, (c) 6%, (d) 8%.

The geometric model incorporated three types of elements: 8-node solid elements (C3D8R) for concrete, 4-node shell elements (S4R) for the steel tube, and 2-node truss elements (T3D2) for the reinforcement bars. To ensure analytical accuracy while maintaining numerical stability, a uniformly structured meshing scheme was adopted. A mesh size of 90 was assigned to the column and foundation components, while the reinforcement zone was modeled using a finer mesh size of 12. Table 4 presents the final meshing specifications.

In the model, the column–foundation interface was defined using hard contact in the vertical direction, while tangential behavior was governed by the Coulomb friction model with a friction coefficient of 0.3. Reinforcement bars were embedded within the concrete using the “Embedded Region” constraint to prevent relative slip between the reinforcement and surrounding concrete. Boundary conditions were applied as fully fixed (encastre) at the bottom of the foundation. Lateral loading was imposed as displacement-controlled at the column top in the horizontal direction, while vertical (gravity) loading was uniformly distributed and applied to both the concrete core and the steel tube. The numerical simulation was carried out using the Static, General analysis step in ABAQUS, which is well-suited for replicating quasi-static experimental procedures.

6.1. Material behavior models

To simulate concrete behavior under cyclic loading, the Concrete Damaged Plasticity (CDP) model was employed. The model parameters included a dilation angle of $\varphi = 30°$, a biaxial-to-uniaxial compressive strength ratio $\beta = 1.16$, a ratio of the second deviatoric stress invariant in tension to compression $K = 0.667$, a viscosity parameter $\mu = 0.005$, and eccentricity $e = 0.1$. The Poisson's ratio for concrete was assumed to be 0.22. In the concrete model, the compressive stiffness recovery was set to 0.6, and tensile stiffness recovery was assumed to be zero to prevent regaining tensile stiffness after cracking. The nonlinear behavior of the steel tube and reinforcement bars was modeled using a bilinear kinematic hardening model with isotropic strain hardening. In this model, the hardening modulus was taken as 0.01 times the initial elastic modulus.

Table 4. Finite element mesh details for different regions of the model.

Modeling region	Element type	Circumferential mesh division	Longitudinal mesh division
Steel Tube Wall (CFT)	S4R	40	20
Strengthened Zone of Column	S4R	40	10
Reinforced Concrete Foundation	C3D8R	60	20
Concrete Core of Column	C3D8R	40	10

6.2. Parametric study

The conducted parametric study focused on analyzing the influence of key parameters, namely, the axial load ratio and the compressive strength of concrete, on the behavior of circular concrete-filled steel tube (CFST) composite columns. The objective of this analysis was to evaluate how these variables affect structural performance indicators, including stiffness, strength, ductility, and energy dissipation capacity.

To ensure a clear and systematic presentation, a structured specimen naming convention was adopted in this study. The format “CCFC-X-Y” was used, in which “CCFC” stands for CFST Column-to-Foundation Connection, “X” represents the axial load ratio in decimal form, and “Y” indicates the concrete compressive strength in megapascals. For instance, the specimen labeled “CCFC-0-30” refers to a CFST column-to-foundation connection with a zero axial load ratio and a concrete compressive strength of 30 MPa.

6.3. Hysteresis curve analysis

Hysteresis curves are a fundamental tool for analyzing the dynamic behavior of structures under cyclic loading, such as seismic actions. The hysteresis and backbone curves of the specimens studied in the parametric analysis are presented in Figs. 8 and 9. These curves represent the relationship between the applied lateral force and corresponding lateral displacement throughout successive loading and unloading cycles. In the case of concrete-filled steel tube (CFST) column-to-foundation connections, hysteresis curves provide insights into stiffness, strength, ductility, and energy dissipation capacity. The shape of these curves typically reflects nonlinear behavior associated with plastic hinge formation at the column base. This nonlinear response indicates the structure's ability to undergo large deformations and absorb energy from seismic events. During the initial loading stages, the hysteresis curves exhibit steep slopes, corresponding to high initial stiffness of the connection. As lateral displacement increases, the curve slope decreases and becomes more rounded, signaling material yielding and entry into the plastic region. The hysteresis loops defined by the enclosed area between the loading and unloading paths serve as a metric for energy dissipation. With increasing displacement amplitude in each cycle, the area of these loops expands, reflecting enhanced energy absorption capacity, which is especially critical for seismic-resistant design, as energy dissipation mechanisms can help prevent structural collapse. Comparison of hysteresis curves across different specimens reveals that parameters such as embedment depth and axial load ratio significantly influence connection behavior. Greater embedment depth and higher axial load ratios (e.g., 0.3) can enhance connection stiffness and strength but may reduce ductility. Specimens subjected to higher axial loads exhibit increased load-bearing capacity; however, the hysteresis loop area at larger displacements tends to decrease, indicating reduced ductility. These findings highlight the importance of optimized design to achieve a balanced trade-off between stiffness, strength, and ductility, thereby maximizing the seismic performance of CFST connections. Table 5 summarizes the results of the parametric analysis on the seismic response of CFST column-foundation connections.

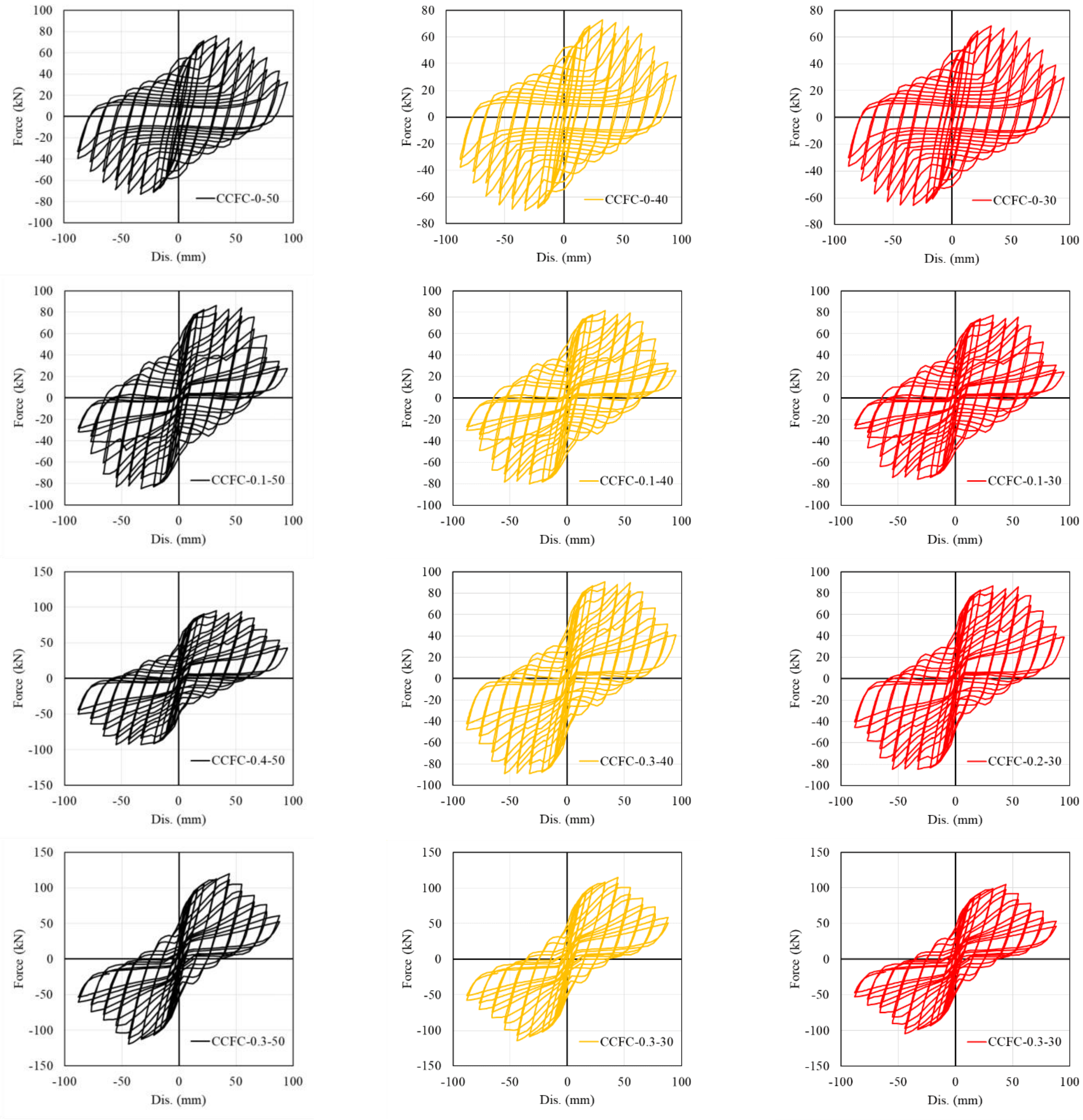

Fig. 8. Hysteresis curves of CFST column-foundation specimens in the parametric study.

6.4. Effect of concrete compressive strength

Based on the data presented in Table 6, the effect of increasing the compressive strength of concrete (30, 40, and 50 MPa) on the hysteretic performance of concrete-filled steel tube (CFST) column-to-foundation connections was examined through key parameters: secant stiffness (K), yield force (P_y), peak force (P_{max}), yield displacement (δ_y), displacement at 85% of peak capacity (δ_u), ductility (μ), and absorbed energy (E). Overall, increasing the concrete strength enhanced stiffness, strength, and energy dissipation capacity. However, its influence on ductility varied depending on the axial load ratio (0, 0.1, 0.2, and 0.3). This analysis explores the effects of concrete strength at three levels in combination with various axial load ratios. Fig. 10 illustrates how variations in concrete compressive strength affect the cyclic lateral load-displacement behavior and energy dissipation capacity of CFST column-to-foundation specimens.

At lower axial load ratios (0, 0.1, and 0.2), increasing the concrete strength from 30 MPa to 50 MPa resulted in an 8–14% improvement in K, an 11–14% increase in P_y, and an 11–14% rise in P_{max}. For instance, in specimens ranging from CCFC-0-30 to CCFC-0-50, stiffness increased from 4.06 to 4.39 kN/mm, yield force from 61.76 to 68.54 kN, and peak force from 68.27 to 75.94 kN. Additionally, the E rose notably by up to 10% demonstrating improved seismic energy dissipation. However, μ decreased with increasing concrete strength (from 4.12 to 3.85 at zero axial load), likely due to the more brittle behavior of higher-strength concrete. δ_y experienced a slight increase, while the δ_u reduced, indicating more concentrated plastic deformations.

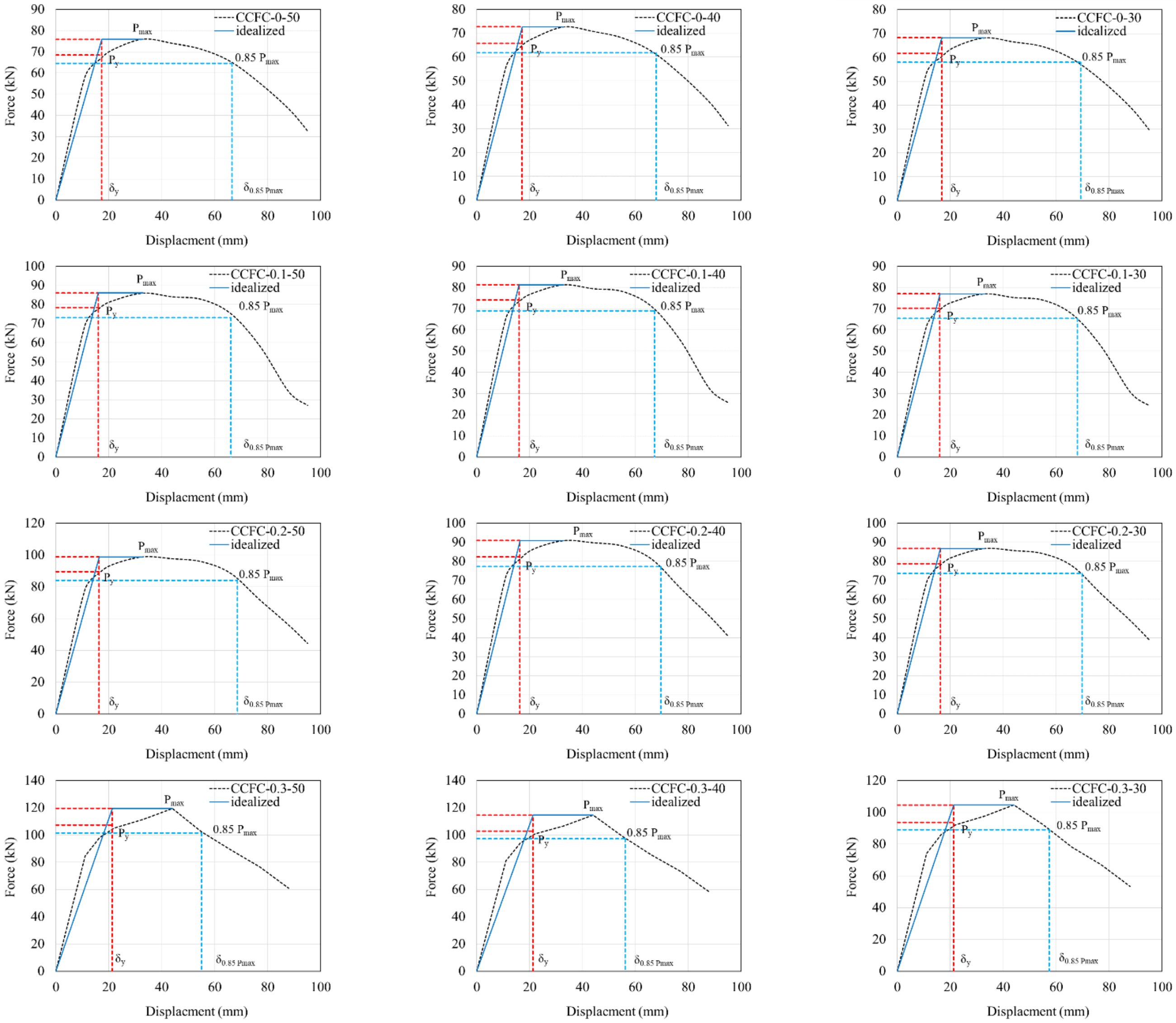

Fig. 9. Backbone curves of CFST specimens under cyclic loading in the parametric study.

At a higher axial load ratio (0.3), the influence of concrete strength on hysteresis behavior shifted. Increasing concrete strength from 30 to 50 MPa continued to enhance stiffness (from 4.93 to 5.63 kN/mm), yield force (from 93.73 to 107.39 kN), and peak force (from 104.69 to 119.60 kN). However, ductility noticeably declined (from 2.70 to 2.59). This reduction stems from the higher axial load, which induces a more brittle response due to the combined effects of compressive and flexural stresses. Although energy absorption increased by up to 14%, the hysteresis loop area at larger displacements diminished due to reduced ductility.

Table 5. Parametric study on the seismic performance indicators of CFST column-foundation connections.

Specimens	Initial stiffness	Yield load	Maximum load	Yield displacement	Ultimate displacement at 85% peak load	Ductility	Energy dissipation
	K (kN/mm)	P_y (kN)	P_{max} (kN)	δ_y (mm)	δ_u (kN)	μ	E (kN.mm)
CCFC-0-30	4.06	61.76	68.27	16.80	69.21	4.12	61797.22
CCFC-0-40	4.24	65.79	72.76	17.18	67.85	3.95	65386.92
CCFC-0-50	4.39	68.54	75.94	17.29	66.51	3.85	68244.33
CCFC-0.1-30	4.80	70.22	77.05	16.05	68.08	4.24	67779.60
CCFC-0.1-40	5.09	74.13	81.29	15.97	67.20	4.21	72496.53
CCFC-0.1-50	5.39	78.50	86.08	15.97	66.17	4.14	77234.42
CCFC-0.2-30	5.33	78.72	86.72	16.27	69.81	4.29	68918.80
CCFC-0.2-40	5.56	82.38	90.88	16.36	69.70	4.26	74128.00
CCFC-0.2-50	6.06	89.65	98.84	16.32	68.56	4.20	77634.65
CCFC-0.3-30	4.93	93.73	104.69	21.25	57.31	2.70	65599.25
CCFC-0.3-40	5.39	102.78	114.59	21.25	56.10	2.64	71841.24
CCFC-0.3-50	5.63	107.39	119.60	21.25	55.10	2.59	75065.42

These findings underscore that, in the design of CFST connections under high axial loads, any increase in concrete strength must be carefully balanced to maintain an optimal compromise between strength and ductility.

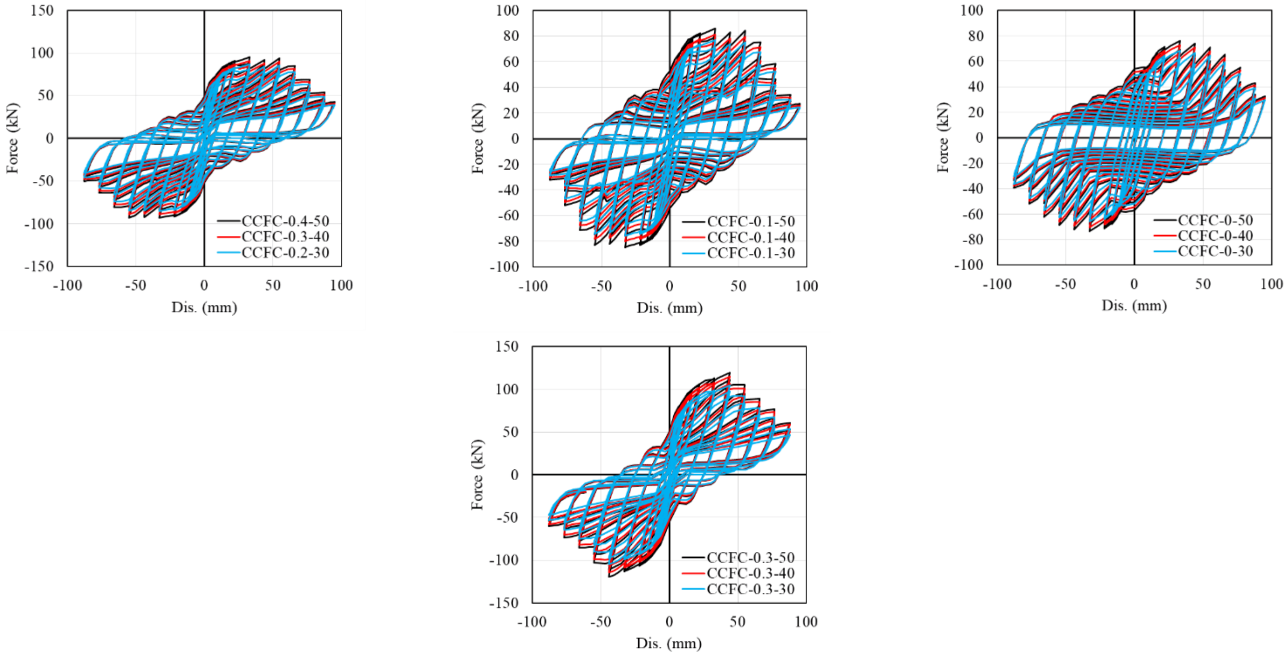

Fig. 10. Effect of concrete compressive strength on hysteresis response.

Table 6. Normalized comparison of key seismic performance indicators relative to the reference specimen (30 MPa concrete strength-I = 30, 40, 50).

Specimen	Stiffness ratio (K_i/K_{30})	Peak load ratio (P_i/P_{30})	Ductility ratio (μ_i/μ_{30})	Energy ratio (E_i/E_{30})
CCFC-0-30	1.00	1.00	1.00	1.00
CCFC-0-40	1.04	1.07	0.96	1.06
CCFC-0-50	1.08	1.11	0.93	1.10
CCFC-0.1-30	1.00	1.00	1.00	1.00
CCFC-0.1-40	1.06	1.06	0.99	1.07
CCFC-0.1-50	1.12	1.12	0.98	1.14
CCFC-0.2-30	1.00	1.00	1.00	1.00
CCFC-0.2-40	1.04	1.05	0.99	1.08
CCFC-0.2-50	1.14	1.14	0.98	1.13
CCFC-0.3-30	1.00	1.00	1.00	1.00
CCFC-0.3-40	1.09	1.09	0.98	1.10
CCFC-0.3-50	1.14	1.14	0.96	1.14

6.5. Effect of axial load

In the present parametric study, the influence of varying axial load ratios (0, 0.1, 0.2, and 0.3) on the hysteretic behavior of concrete-filled steel tube (CFST) column-to-foundation connections was evaluated. Hysteresis behavior, analyzed through load-displacement curves under cyclic loading, reflects key structural performance indices including K, P_y, P_{max}, δ_y, δ_u, μ, and E. The tabulated data indicate that increasing axial load ratio, particularly in the range of 0 to 0.3, leads to significant changes in these indicators. The influence of axial load ratio on the cyclic performance of CFST column-to-foundation connections is observed in Fig. 11. Corresponding normalized performance parameters, including stiffness, peak load, ductility, and energy dissipation, are presented in Table 7.

An increase in axial load ratio from 0 to 0.3 generally improves K, P_y, and P_{max}. For example, in specimens with a concrete compressive strength of 30 MPa, secant stiffness increased from 4.06 kN/mm in CCFC-0-30 to 4.93 kN/mm in CCFC-0.3-30, while peak force rose from 68.27 kN to 104.69 kN. However, this enhancement in axial load is accompanied by a notable reduction in μ, decreasing from 4.12 in CCFC-0-30 to 2.70 in CCFC-0.3-30. This decline signifies a restriction in the plastic deformation capacity of the connection under higher axial loads.

On the other hand, E tends to increase with axial load in most cases, particularly in specimen CCFC-0.2-50, which reached 77,634.65 kN·mm. However, at an axial load ratio of 0.3, the rise in energy absorption becomes more limited due to diminished ductility. These observations demonstrate that while higher axial loads enhance stiffness and strength, they may negatively affect ductility and plastic performance, highlighting the need for a carefully balanced design in seismic applications.

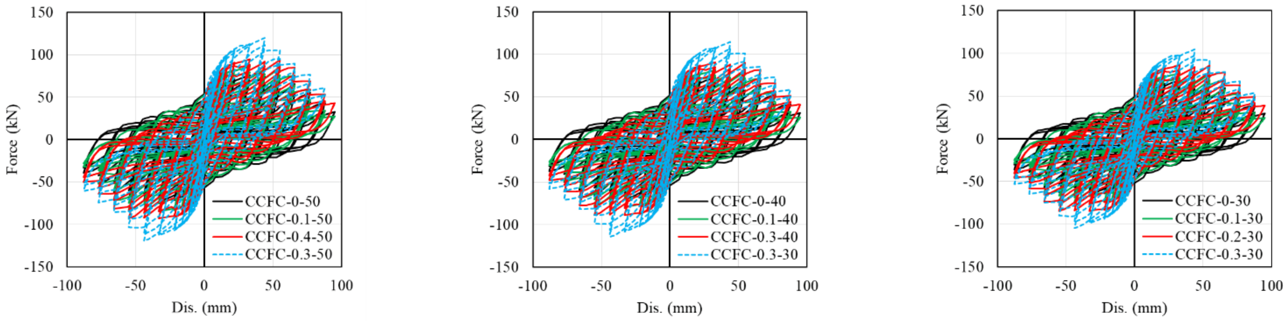

Fig. 11. Effect of axial load ratio on hysteresis behavior of CFST specimens.

The results for the 30 MPa concrete strength group illustrate the impact of increasing axial load ratios (0, 0.1, 0.2, and 0.3) on the hysteretic behavior of CFST column-to-foundation connections. As axial load increased, secant stiffness rose by up to 31.28% (from 4.06 to 5.33 kN/mm), and peak load improved by 53.35% (from 68.27 to 104.69 kN), indicating a substantial enhancement in load-carrying capacity and resistance to initial deformations. However, ductility at an axial load ratio of 0.3 dropped by 34.47% (from 4.12 to 2.70), reflecting a restriction in plastic deformation capacity and a reduced ability to accommodate large displacements. Absorbed energy increased by up to 11.50%, although this gain was more limited at higher axial load ratios due to reduced ductility. These findings highlight the importance of optimizing axial load to maintain a balanced performance in terms of stiffness, strength, and ductility for seismic design.

The specimens with 40 MPa concrete exhibited consistent behavioral trends as the axial load ratio increased from 0 to 0.3. Secant stiffness improved by up to 31.13% (from 4.24 to 5.56 kN/mm), and peak load increased by 57.52% (from 72.76 to 114.59 kN), emphasizing enhanced interaction between the steel tube and concrete infill. However, ductility dropped by 33.16% (from 3.95 to 2.64), accompanied by a 23.69% rise in yield displacement and a 17.32% reduction in the 85% capacity displacement—signifying more concentrated deformation zones. Energy absorption increased by 13.37%, but the observed reduction in ductility under higher axial loads again highlights the need for design caution to preserve plastic deformation capacity, especially in seismic applications.

In the 50 MPa concrete strength group, axial load increases led to even more pronounced gains: secant stiffness rose by 38.04% (from 4.39 to 6.06 kN/mm), and peak load increased by 57.49% (from 75.94 to 119.60 kN), signifying marked improvements in structural performance. However, ductility declined by 32.73% (from 3.85 to 2.59) at an axial load ratio of 0.3, indicating increased brittleness and reduced deformation capacity. While absorbed energy increased by up to 13.67%—the highest among the tested concrete strengths—this gain became limited under high axial load due to constrained ductility. These observations emphasize the necessity of carefully calibrating design parameters to balance stiffness and ductility under seismic loading, particularly when using high-strength concrete with elevated stiffness and strength potential.

6.6. Analysis of dissipated energy variations

The analysis E in concrete-filled steel tube (CFST) column-to-foundation connections, based on tabulated data, illustrates the effects of axial load ratio (0, 0.1, 0.2, and 0.3) and concrete compressive strength (30, 40, and 50 MPa) on the seismic energy dissipation capacity. As illustrated in Fig. 12, the cumulative energy dissipation increases significantly with improvements in axial load ratio and concrete strength, while variations in embedment depth show a more moderate effect. Dissipated energy—quantified by the area enclosed within the hysteresis loops of the force–displacement curves is a key indicator for evaluating seismic performance, as it reflects the structure's ability to dissipate cyclic energy and reduce dynamic earthquake effects. This analysis emphasizes the underlying scientific principles and engineering mechanisms influencing energy dissipation behavior.

Table 7. Parametric comparison of normalized seismic performance indicators relative to the baseline CFST specimen (i=0, 0.1, 0.2, 0.3).

Specimen	Stiffness ratio (K_i/K_0)	Peak load ratio (P_i/P_0)	Ductility ratio (μ_i/μ_0)	Energy ratio (E_i/E_0)
CCFC-0-30	1.00	1.00	1.00	1.00
CCFC-0.1-30	1.18	1.13	1.03	1.10
CCFC-0.2-30	1.31	1.27	1.04	1.12
CCFC-0.3-30	1.21	1.53	0.65	1.06
CCFC-0-40	1.00	1.00	1.00	1.00
CCFC-0.1-40	1.20	1.12	1.07	1.11
CCFC-0.2-40	1.31	1.25	1.08	1.13
CCFC-0.3-40	1.27	1.57	0.67	1.10
CCFC-0-50	1.00	1.00	1.00	1.00
CCFC-0.1-50	1.23	1.13	1.08	1.13
CCFC-0.2-50	1.38	1.30	1.09	1.14
CCFC-0.3-50	1.28	1.57	0.67	1.10

For 30 MPa concrete, dissipated energy increased from 61,797.22 to 68,918.80 kN·mm (an 11.50% rise) as the axial load ratio increased from 0 to 0.2. This improvement stems from enhanced interaction between the steel tube and the concrete core due to higher compressive stress, which leads to increased stiffness (up to 31.28%) and strength (up to 27.00%), thereby enlarging the hysteresis loops at intermediate displacement levels. However, at an axial load ratio of 0.3, energy decreased to 65,599.25 kN·mm (a lower 6.15% increase), primarily due to a 34.47% drop in ductility, where local buckling of the steel tube and crushing of the concrete core limited the energy dissipation at larger deformations.

For 40 MPa concrete, dissipated energy grew from 65,386.92 to 74,128.00 kN·mm (an increase of 13.37%) at an axial load ratio of 0.2, driven by enhanced shear resistance of concrete and a 31.13% gain in stiffness. However, at a ratio of 0.3, energy only rose to 71,841.24 kN·mm (9.85% increase), as ductility declined by 33.16% and excessive compressive stress induced more brittle behavior.

With 50 MPa concrete, the highest dissipated energy was observed at a 0.2 axial load ratio, 77,634.65 kN·mm (13.67% increase), thanks to the superior compressive strength and enhanced confinement provided by the steel tube. At a ratio of 0.3, energy decreased to 75,065.42 kN·mm (a 9.98% rise), with ductility dropping by 32.73% due to premature crushing of the concrete core under elevated compressive stresses, thereby limiting hysteresis loop expansion.

From a scientific and engineering standpoint, increasing the axial load ratio up to 0.2 improves confinement and enhances energy dissipation capacity. However, at 0.3, excessive axial stress accelerates local buckling and suppresses plastic behavior. Therefore, for seismic design of CFST connections, an axial load ratio of 0.2 is considered optimal to ensure a balanced performance between dissipated energy, stiffness, and ductility. Higher load ratios may require additional confinement or reinforcement strategies to prevent premature failure.

6.7. Analysis of axial and hoop strain variations at the column base

The variations in axial and hoop strains at the base of concrete-filled steel tube (CFST) columns connected to foundations are significantly influenced by the compressive strength of concrete (30, 40, and 50 MPa) and axial load ratios (0, 0.1, 0.2, and 0.3). As shown in Fig. 13, strain gauges were installed at the base of the CFST column near the column-foundation interface to monitor localized behavior. Fig. 14 presents the longitudinal load-strain response under cyclic loading, demonstrating the effects of concrete compressive strength at varying axial load ratios (n = 0 to 0.3). Axial strains mainly caused by compressive stresses from axial loading and flexural effects from cyclic excitation are concentrated at the column base, a critical region near the foundation. As the axial load ratio increases from 0 to 0.3, axial strains grow due to elevated compressive stresses in both the steel tube and the concrete core. This phenomenon is particularly amplified at 0.2 and 0.3 load ratios, where plastic hinge formation occurs at approximately 25–75 mm above the foundation surface. For 30 MPa concrete, increasing axial load to 0.2 enhances stiffness by 31.28% and dissipated energy by 11.50%, suggesting a favorable balance between axial strain and effective confinement. The hoop strains, resulting from the lateral pressure of the steel tube against the concrete core, help enhance ductile behavior in this range by delaying concrete cracking and increasing the plastic deformation capacity. This behavior is confirmed by higher ductility ($\mu = 4.29$ in CCFC-0.2-30) and larger hysteresis loops in the analyses. For higher-strength concrete (40 and 50 MPa), axial and hoop strain behavior under varying axial loads differs noticeably. At 40 MPa, raising the axial load to 0.2 improves stiffness (by 31.13%) and energy dissipation (by 13.37%), reflecting better confinement and reduced detrimental hoop strain. This is attributed to the concrete's enhanced capacity to withstand compressive stresses, which allows more uniform distribution of axial strains in the plastic zone and mitigates premature failure. However, at a 0.3 load ratio, axial strains become excessively exacerbated by a 23.69% increase in yield displacement while hoop strains lead to local buckling of the tube and concrete crushing under high stresses. These effects correspond to reduced ductility (by 33.16% in CCFC-0.3-40) and smaller hysteresis loops. A similar trend is observed for 50 MPa concrete, though performance metrics at a 0.2 load ratio show further improvements in stiffness, increasing by 38.04% and energy dissipation by 13.67% due to enhanced confinement. This controls hoop strain within an optimal range and promotes ductile behavior. Nevertheless, at a 0.3 axial load ratio, excessive axial strains and a 32.73% drop in ductility indicate greater brittleness and reduced plastic capacity.

At a 0.3 load ratio across all three concrete strengths, axial strains reach critical levels that accelerate concrete crushing and tube buckling, evidenced by a 17.32% reduction in ultimate displacement and up to 34.47% loss in ductility. In this state, hoop strains exceed optimal confinement thresholds, contributing to cracking and diminished energy dissipation capacity. Although the impact is less severe in 50 MPa concrete due to its higher compressive resistance, a notable ductility loss is still observed. From an engineering perspective, these observations suggest that an axial load ratio of 0.2 provides the optimal balance between axial and hoop strain behavior for all examined concrete strengths, resulting in maximum energy dissipation and sustained ductility. For seismic design, axial load ratios beyond 0.2 are discouraged unless additional confinement measures such as thicker steel tubes or external ring stiffeners are implemented to mitigate the adverse effects of excessive strain concentrations at the column base.

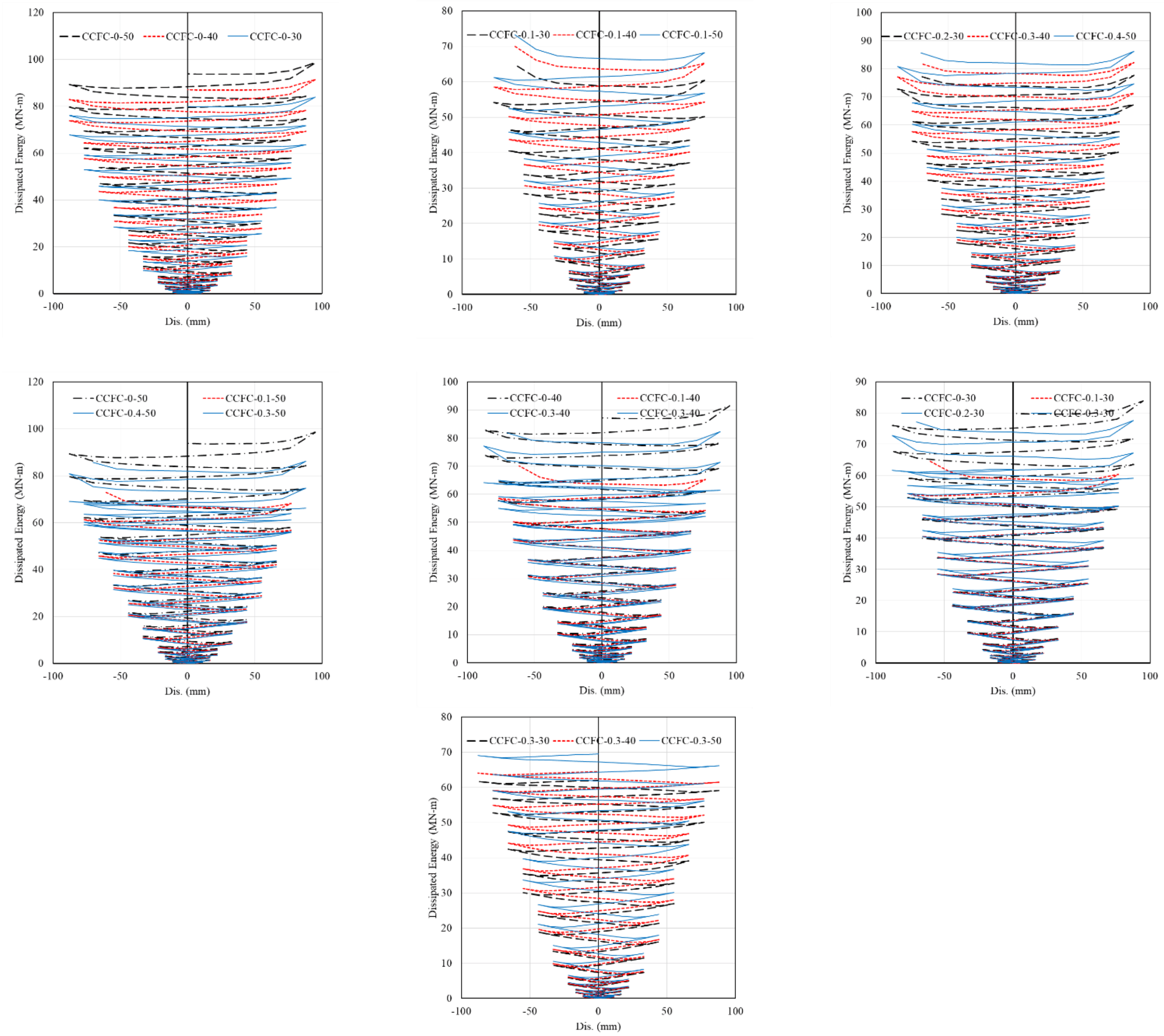

Fig. 12. Comparison of energy dissipation versus lateral displacement for various CFST column-foundation specimens.

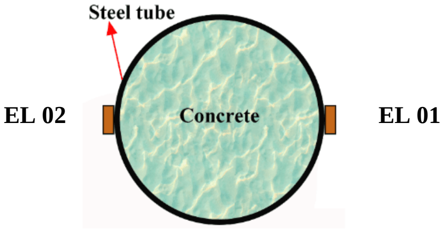

Fig. 13. Strain gauge locations at the base of the CFST column near the column-to-foundation interface.

7. Conclusion

Embedded connections between circular CFST columns and foundations exhibit robust performance under cyclic loading, making them a reliable structural solution with practical construction benefits. In this study, the cyclic behavior of such connections was evaluated through experimental testing and numerical simulation. The principal findings and conclusions are summarized as follows:

- The embedded connection effectively transfers both axial and lateral loads from the CFST column to the foundation while accommodating nonlinear deformations under severe loading. The dominant failure mechanism was plastic hinge formation at the column base. No signs of pull-out or brittle fracture at the interface were observed, confirming the connection's seismic reliability and ductility.
- The embedment depth (Le) was identified as the most influential parameter affecting connection behavior. Increasing Le led to improvements in flexural strength, energy dissipation capacity, and ductility. An embedment depth equal to the column diameter (D) was sufficient for full moment transfer and stable cyclic behavior; however, increasing the depth to 1.2D or beyond further enhanced hysteretic performance and mitigated stiffness degradation under large deformations.
- Due to the circular geometry of the column and the confining effect of the surrounding foundation concrete, a quasi-triaxial compressive state developed at the interface. This confinement enhanced the mechanical interlock between the steel tube and concrete core, preventing premature crushing and localized failure.
- The numerical simulations supported the experimental trends and provided valuable insights into stress distribution, confinement effects, and shear transfer mechanisms at the connection. The results highlighted that increased side friction and contact area between the column and foundation significantly enhance initial stiffness and post-yield strength.
- To ensure plastic hinge formation occurs within the column rather than at the connection, a minimum embedment depth based on internal force equilibrium and shear stress distribution is recommended. Additionally, a design expression for the minimum concrete thickness beneath the embedded region is proposed to prevent punching shear failure.
- Axial and hoop strain analyses at the base of CFST columns revealed that concrete compressive strength (30, 40, and 50 MPa) and axial load ratio (0, 0.1, 0.2, and 0.3) significantly influence seismic performance. Increasing axial load up to 0.2, particularly with 50 MPa concrete, enhanced stiffness (by up to 38.04%), strength (up to 57.49%), and energy dissipation (up to 13.67%) due to improved confinement and favorable strain distribution. However, at an axial load ratio of 0.3, excessive axial and hoop strains triggered local buckling and concrete crushing, leading to reduced ductility (up to 34.47%) and limited energy dissipation capacity.
- These findings, confirmed through ABAQUS simulations and experimental observations, underscore the importance of optimizing the axial load ratio within the range of 0.1 to 0.2 to achieve a balanced design in terms of stiffness, strength, and ductility. For seismic applications, it is recommended that CFST connections be reinforced, e.g., via increased tube thickness or ring stiffeners at the column base to mitigate the adverse effects of excessive strains under high axial load and ensure optimal structural performance.

Critically, embedment depth (Le), particularly at or beyond the column diameter (D), significantly enhances hysteretic performance, while optimal concrete compressive strength and axial load ratios (0.1-0.2) boost stiffness, strength, and energy dissipation by promoting favorable stress distribution and confinement within the composite section. Conversely, excessive axial load (0.3) can severely compromise ductility due to premature buckling and concrete crushing, underscoring the necessity for balanced design and localized reinforcement.

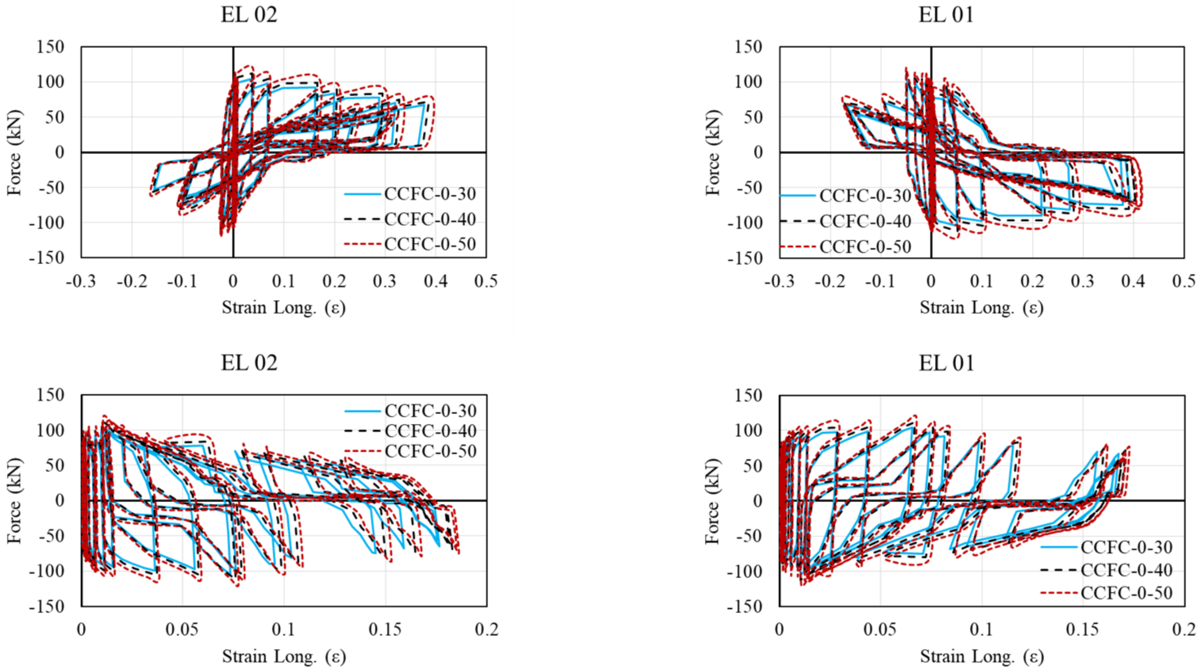

(a) Effect of concrete compressive strength (n = 0)

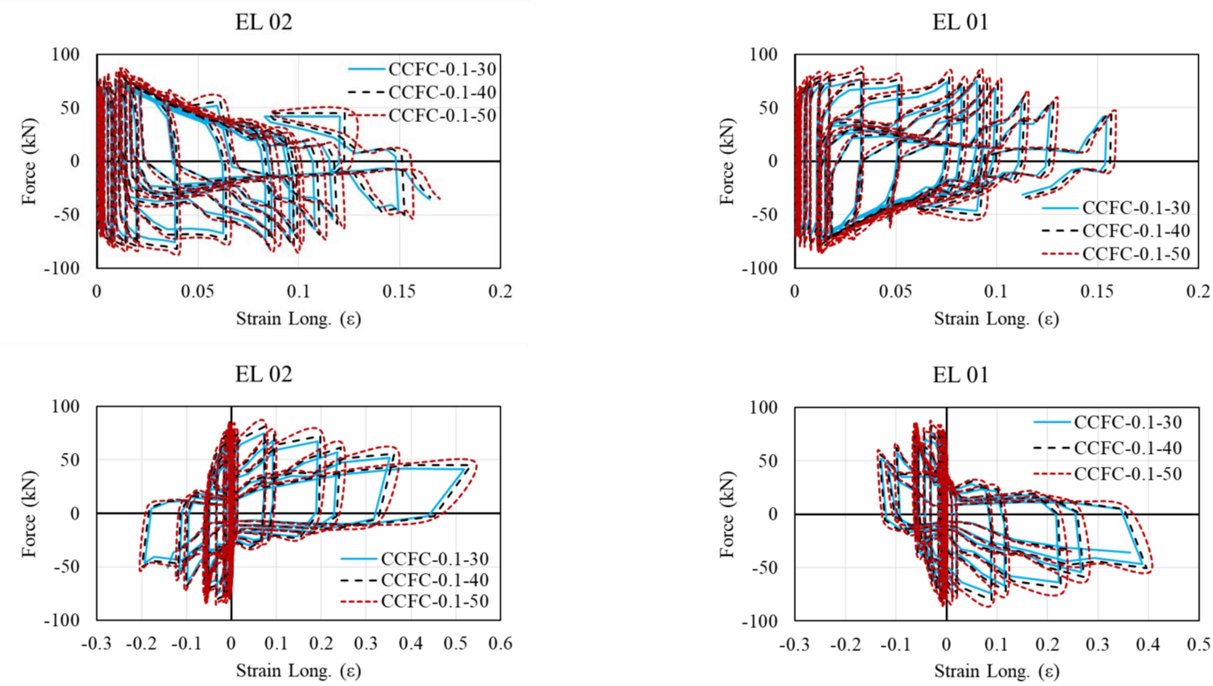

(b) Effect of concrete compressive strength (n = 0.1)

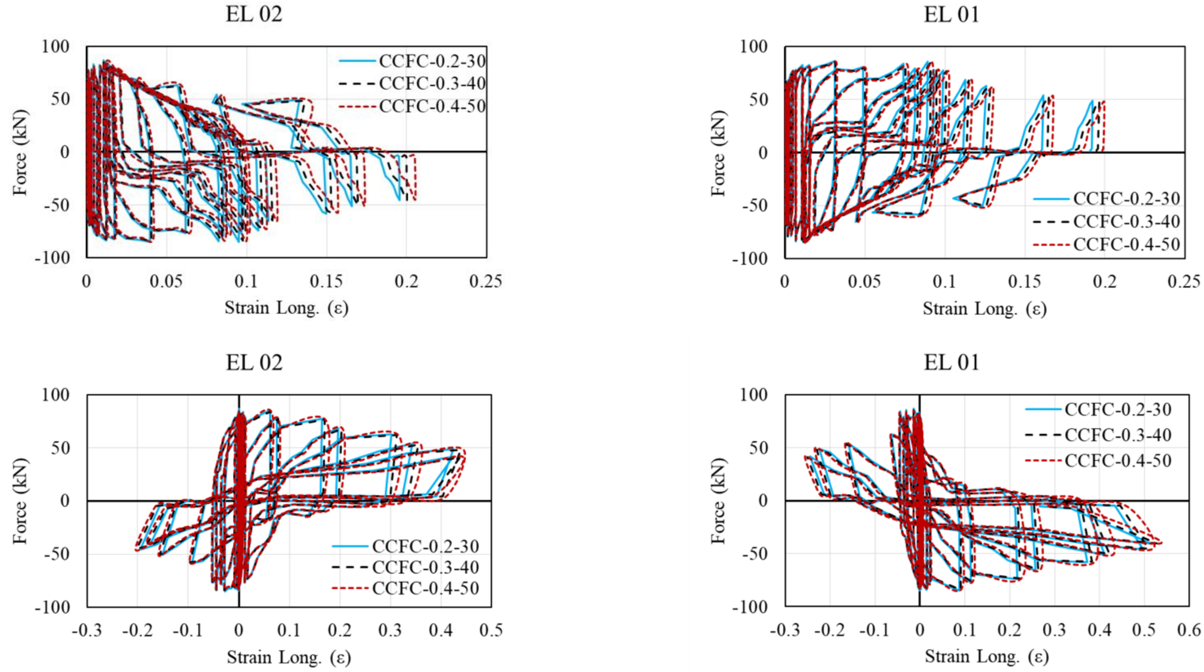

(c) Effect of concrete compressive ctrength (n=0.2)

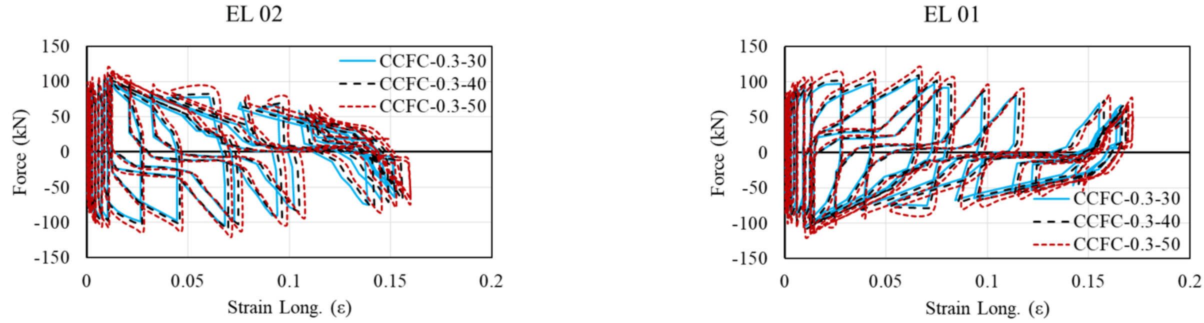

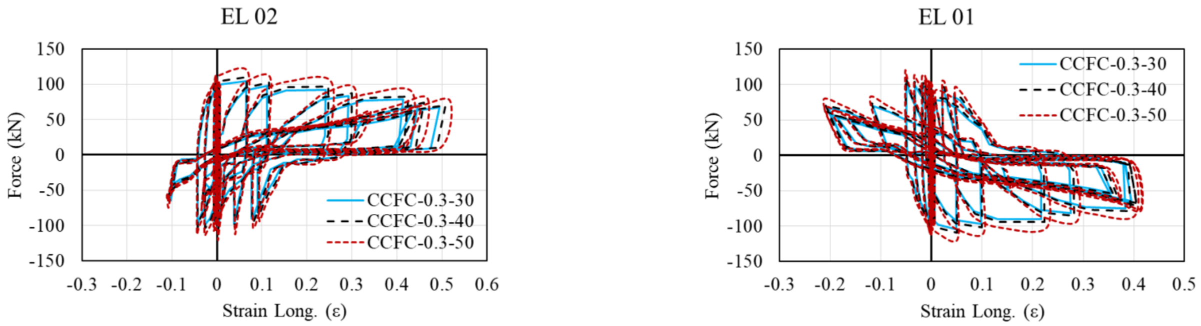

(d) Effect of concrete compressive strength (n = 0.3)

Fig. 14. Longitudinal load–strain response of CFST column-foundation connections under cyclic loading.

Statements & Declarations

Author contributions

Saleh Mohammad-Ebrahimzadeh-Sepasgozar: Conceptualization, Investigation, Methodology, Formal analysis, Resources, Writing - Original Draft, Writing - Review & Editing.

Morteza Naghipour: Conceptualization, Methodology, Formal analysis, Project administration, Supervision, Writing - Review & Editing.

Funding

The authors received no financial support for the research, authorship, and/or publication of this article.

Data availability

The data presented in this study will be available on interested request from the corresponding author.

Declarations

The authors declare no conflict of interes.

References

[1] He, J. C. W., Clifton, G. C., Ramhormozian, S., Hogan, L. S. Numerical and analytical study of pinned column base plate connections. Journal of Constructional Steel Research, 2023; 204: 107846. doi:10.1016/j.jcsr.2023.107846.

[2] Nawar, M. T., Matar, E. B., Maaly, H. M., Alaaser, A. G., El-Zohairy, A. Assessment of Rotational Stiffness for Metallic Hinged Base Plates under Axial Loads and Moments. Buildings, 2021; 11: doi:10.3390/buildings11080368.

[3] Khodaie, S., Mohamadi-shooreh, M. R., Mofid, M. Parametric analyses on the initial stiffness of the SHS column base plate connections using FEM. Engineering Structures, 2012; 34: 363-370. doi:10.1016/j.engstruct.2011.09.026.

[4] Grauvilardell, J. E., Lee, D. Synthesis of Design, Testing and Analysis Research on Steel Column Base Plate Connections in High-Seismic Zones. Minneapolis (MN): Department of Civil Engineering, University of Minnesota; 2005. Report No.: ST-04-02.

[5] Camacho, J. Seismic performance of exposed column base plates (Phase I). In: 2007 Earthquake Engineering Symposium for Young Researchers, Multi-Disciplinary Center for Earthquake Engineering Research (MCEER); 2007 Nov 1; Buffalo, United States. p. 52-69.

[6] Abejide, O. S. Effectiveness of Base Plate Thickness Design Criteria in Steel Columns. Research Journal of Applied Sciences, 2007; 2: 1207-1217. doi:rjasci.2007.1207.1217.

[7] Kanvinde, A. M., Jordan, S. J., Cooke, R. J. Exposed column base plate connections in moment frames — Simulations and behavioral insights. Journal of Constructional Steel Research, 2013; 84: 82-93. doi:10.1016/j.jcsr.2013.02.015.

[8] Hitaka, T., Suita, K., Kato, M. CFT column base design and practice in Japan. In: Proceedings of the International Workshop on Steel and Concrete Composite Construction; 2003 Oct 1; p. 8-9.

[9] Hitaka, T., Matsui, C., Sakai, J. i. Cyclic tests on steel and concrete-filled tube frames with Slit Walls. Earthquake Engineering & Structural Dynamics, 2007; 36: 707-727. doi:10.1002/eqe.648.

[10] Marson, J., Bruneau, M. Cyclic Testing of Concrete-Filled Circular Steel Bridge Piers having Encased Fixed-Based Detail. Journal of Bridge Engineering, 2004; 9: 14-23. doi:10.1061/(ASCE)1084-0702(2004)9:1(14).

[11] Zhang, G., Xiao, Y., Kunnath, S. Low-Cycle Fatigue Damage of Circular Concrete-Filled-Tube Columns. ACI Structural Journal, 2009; 106: doi:10.14359/56353.

[12] Roeder Charles, W., Lehman Dawn, E., Bishop, E. Strength and Stiffness of Circular Concrete-Filled Tubes. Journal of Structural Engineering, 2010; 136: 1545-1553. doi:10.1061/(ASCE)ST.1943-541X.0000263.

[13] Moon, J., Roeder, C. W., Lehman, D. E., Lee, H.-E. Analytical modeling of bending of circular concrete-filled steel tubes. Engineering Structures, 2012; 42: 349-361. doi:10.1016/j.engstruct.2012.04.028.

[14] Moon, J., Lehman Dawn, E., Roeder Charles, W., Lee, H.-E. Strength of Circular Concrete-Filled Tubes with and without Internal Reinforcement under Combined Loading. Journal of Structural Engineering, 2013; 139: 04013012. doi:10.1061/(ASCE)ST.1943-541X.0000788.

[15] Moon, J., Lehman, D. E., Roeder, C. W., Lee, H.-E. Evaluation of embedded concrete-filled tube (CFT) column-to-foundation connections. Engineering Structures, 2013; 56: 22-35. doi:10.1016/j.engstruct.2013.04.011.

[16] Lee, S.-S., Moon, J., Park, K.-S., Bae, K.-W. Strength of Footing with Punching Shear Preventers. The Scientific World Journal, 2014; 2014: 474728. doi:10.1155/2014/474728.

[17] Moon, J., Lehman, D. E., Roeder, C. W., Lee, H.-E., Lee, T.-H. Analytical Evaluation of Reinforced Concrete Pier and Cast-in-Steel-Shell Pile Connection Behavior considering Steel-Concrete Interface. Advances in Materials Science and Engineering, 2016; 2016: 4159619. doi:10.1155/2016/4159619.

[18] Building and Housing Research Center. Part 10: National Building Regulations of Iran – Part 10: Steel Structures. Tehran (IR): Ministry of Roads and Urban Development; 2024 (In Persian).

[19] Kenarangi, H., Bruneau, M. Experimental Study on Composite Action in Reinforced Concrete–Filled Steel-Tube Shaft Foundations. Journal of Bridge Engineering, 2019; 24: 04019060. doi:10.1061/(ASCE)BE.1943-5592.0001407.

[20] Liu, J., Xu, T., Wang, X. Seismic Behavior and Design of Concrete-Filled Thin-Walled Steel Tube Column-to-Foundation Connections. Journal of Structural Engineering, 2021; 147: 04021072. doi:10.1061/(ASCE)ST.1943-541X.0003037.

[21] Xu, T., Zhang, S., Liu, J., Wang, X., Guo, Y. Seismic behavior of carbon fiber reinforced polymer confined concrete filled thin-walled steel tube column-foundation connection. Composite Structures, 2022; 279: 114804. doi:10.1016/j.compstruct.2021.114804.

[22] Chen, Z., Xu, J., Zhou, T., Su, J. Seismic research on column base joint of L-shaped CFST columns under cyclic loading. Structures, 2022; 45: 1212-1224. doi:10.1016/j.istruc.2022.09.095.

[23] Zhou, X., Xu, T., Liu, J., Wang, X., Chen, Y. F. Seismic performance of concrete-encased column connections for concrete filled thin-walled steel tube piers. Engineering Structures, 2022; 269: 114803. doi:10.1016/j.engstruct.2022.114803.

[24] Di, J., Han, B., Zhou, X., Hu, L., Qi, Y., Qin, F. Experimental investigation into cyclic working performances of prefabricated CFST columns with improved column-footing connections. Journal of Building Engineering, 2022; 46: 103772. doi:10.1016/j.jobe.2021.103772.

[25] Benjamin L. Worsfold, J. P. M., John, F. S. Moment Transfer at Column-Foundation Connections: Physical Tests. ACI Structural Journal, 119: doi:10.14359/51734799.

[26] Liu, B., Zhang, L., Sun, H., Feng, M., Dou, K. Side shear strength and load-transfer mechanism of corrugated steel column–foundation socket connection. Case Studies in Construction Materials, 2022; 17: e01377. doi:10.1016/j.cscm.2022.e01377.

[27] Cogurcu, M. T., Uzun, M. Experimental investigation of a new precast column-foundation connection under cyclic loading. Journal of Building Engineering, 2022; 50: 104245. doi:10.1016/j.jobe.2022.104245.

[28] Haraldsson Olafur, S., Janes Todd, M., Eberhard Marc, O., Stanton John, F. Seismic Resistance of Socket Connection between Footing and Precast Column. Journal of Bridge Engineering, 2013; 18: 910-919. doi:10.1061/(ASCE)BE.1943-5592.0000413.

[29] Mohebbi, A., Saiidi, M. S., Itani Ahmad, M. Shake Table Studies and Analysis of a PT-UHPC Bridge Column with Pocket Connection. Journal of Structural Engineering, 2018; 144: 04018021. doi:10.1061/(ASCE)ST.1943-541X.0001997.

[30] Wang, Z., Li, T., Qu, H., Wei, H., Li, Y. Seismic Performance of Precast Bridge Columns with Socket and Pocket Connections Based on Quasi-Static Cyclic Tests: Experimental and Numerical Study. Journal of Bridge Engineering, 2019; 24: 04019105. doi:10.1061/(ASCE)BE.1943-5592.0001463.

[31] Zhang, G., Han, Q., Xu, K., Du, X., He, W. Experimental investigation of seismic behavior of UHPC-filled socket precast bridge column-foundation connection with shear keys. Engineering Structures, 2021; 228: 111527. doi:10.1016/j.engstruct.2020.111527.

[32] Si, X., Wen, J., Zhang, G., Jia, Z., Han, Q. Seismic performance of precast double-column pier with UHPC-filled socket connections. Engineering Structures, 2023; 285: 115618. doi:10.1016/j.engstruct.2023.115618.

[33] Zhang, G., Han, Q., Xu, K., Song, Y., Li, J., He, W. Numerical analysis and design method of UHPC grouted RC column- footing socket joints. Engineering Structures, 2023; 281: 115755. doi:10.1016/j.engstruct.2023.115755.

[34] American Concrete Institute (ACI). ACI 318-19: Building Code Requirements for Structural Concrete and Commentary. Farmington Hills (MI): ACI; 2019. doi:10.14359/51716937.

[35] American Institute of Steel Construction (AISC). AISC 360-22: Specification for Structural Steel Buildings. Farmington Hills (MI): AISC; 2022.

Civil Engineering and Applied Solutions
Research Article
journal homepage: ceas.journals.umz.ac.ir

Evaluation of Setting Behavior in Slag-Based Geopolymer Concrete using Ultrasonic Pulse Velocity under Varying Mix Proportions

Nader Sabeti [a*]

[a] *Department of Civil and Architectural Engineering, KTH Royal Institute of Technology, Stockholm, Sweden*

ARTICLE INFO

Keywords:
Sustainable development
Geopolymer concrete
Slag-based binder
Setting time
Ultrasonic pulse velocity (UPV) method
Freshcon mold system

Article history:
Received 03 July 2025
Accepted 23 July 2025
Available online 01 August 2025

ABSTRACT

In response to the growing environmental crisis and the urgent need to curb carbon emissions and improve waste management, slag-based geopolymer concrete has emerged as a low-energy, sustainable alternative to ordinary Portland cement. This study investigates the initial and final setting behaviour of ground-granulated blast-furnace slag (GGBFS) geopolymer concrete using the ultrasonic pulse velocity (UPV) technique alongside a Freshcon mold system. Key variables examined include the molarity and type of alkaline activator, the alkali-to-slag ratio, and the proportion of slag within the concrete matrix. UPV traces delineate three distinct stages of induction (dormant), polymerization onset (activation), and network consolidation (hardening), each typified by its signature "S-shaped" profile. In this study, increasing the concentration of the alkaline activator and the proportion of ground granulated blast-furnace slag (GGBFS) was found to dramatically shorten both initial and final setting times of slag-based geopolymer mixtures; however, beyond an optimal activator concentration and solution-to-slag ratio, these accelerating effects attenuate and polymerization kinetics become disrupted. Notably, whereas ordinary Portland cement exhibits an induction period over 240 minutes, geopolymer samples activated at 6M complete their induction phase in under 30 minutes, a 6–8 fold increase in initial setting rate. Such rapid setting, while advantageous for expediting placement cycles, poses challenges in mass concrete pours by heightening the risk of cold joints and imposing stringent formwork time constraints. Conversely, this accelerated hardening can be leveraged as a significant asset in future investigations into precast concrete elements and tunnel-lining shotcrete applications.

1. Introduction

Geopolymer concrete, as a pioneering innovation in sustainable construction materials, has been developed to reduce greenhouse gas emissions and make optimal use of industrial by-products [1-3]. CO_2 emissions from Portland cement production amount to approximately 0.8–1.0 tonnes per tonne of cement, representing over 7–8% of total global emissions [4, 5]. In contrast, life-cycle assessments of blast-furnace slag–based geopolymer concrete show that its CO_2 emissions are 65–75% lower than those of Portland cement concrete [6]. Moreover, the use of slag as a precursor converts steelmaking waste into a valuable source of silica and calcium, thereby reducing industrial residues and conserving natural resources [1, 7]. In other words, geopolymer concrete not only exhibits a reduced carbon footprint but also contributes effectively to CO_2 sequestration and energy savings during material production [3, 4]. Recent studies have demonstrated that, during the alkaline activation process, recovering waste heat energy and maximizing the sodium silicate-to-hydroxide ratio can further reduce carbon emissions by up to 80%. This exceptional environmental potential renders geopolymer concrete an attractive option for low-carbon structural projects and climate-sensitive regions [1, 2].

The chemical behavior of blast-furnace slag–based geopolymer concrete is governed by geopolymerization reactions [8-10].

---

* Corresponding author.
E-mail addresses: sabeti@kth.se (N. Sabeti).

https://doi.org/10.22080/ceas.2025.29600.1023
ISSN: 3092-7749/© 2025 The Author(s). Published by University of Mazandaran.
This article is an open access article distributed under the terms and conditions of the Creative Commons Attribution (CC-BY) license (https://creativecommons.org/licenses/by/4.0/deed.en)
How to cite this article: Sabeti, N. Evaluation of Setting Behavior in Slag-Based Geopolymer Concrete using Ultrasonic Pulse Velocity under Varying Mix Proportions. Civil Engineering and Applied Solutions. 2025; 1(3): 48–61. doi:10.22080/ceas.2025.29600.1023.

Iron-smelting slag comprises a mixture of glassy and crystalline phases, namely C_2S, C_3S, the Mg–Fe solid solution, and various silicate phases [7]. In the presence of strong alkaline activators and alkali silicates, the amorphous silica–alumina network rapidly dissolves, releasing SiO_4^{4-} and AlO_4^{5-} monomers [10-13]. These anions then coordinate with Na^+ or K^+ cations in solution to form densely cross-linked –Si–O–Al–O– polymer chains, which evolve into N–A–S–H gels within the macromolecular matrix [9, 11, 14]. Concurrently, the abundant Ca^{2+} in the slag fosters the co-precipitation of C–A–S–H alongside N–A–S–H, yielding a dual-gel microstructure with enhanced mechanical performance [15, 16]. The Si/Al and Ca/Si ratios critically influence polymerization kinetics, pore structure, and crystalline phase development [17]. Moreover, the silicate modulus (Na_2SiO_3/NaOH ratio) and the activator concentration dictate the gel's microstructural characteristics: a higher silicate modulus promotes increased silica chain length and network connectivity, thereby reducing permeability [18, 19].

The rheological properties and setting time of fresh concrete are critical factors that influence its workability, durability, early-age bond strength, and suitability for various construction applications, including mass concrete pouring, precast element fabrication, and shotcrete use for tunnel support [20-22]. Traditional shotcrete formulations, for example, typically rely on Portland cement with a high clinker content to achieve the rapid setting required for effective shotcrete tunnel lining [22]. However, the use of Portland cement often necessitates the application of thicker layers, leading to increased consumption and a subsequent rise in environmental impacts [5, 6]. Consequently, there is a pressing need for further research to identify and develop sustainable alternative materials, such as geopolymers, which can deliver comparable performance while mitigating environmental effects [3].

Previous studies have demonstrated that the setting time of geopolymer concrete is influenced by a range of factors, including the type of raw material, the type of alkaline activator, the molar concentration of the activator, the alkali-to-raw material ratio, ambient temperature during mixing, and several other variables [23-25]. Both the type of alkali activator (NaOH vs. KOH) and its concentration profoundly affect paste behavior [18, 24]. Specifically, increasing the molarity of hydroxide solutions elevates mixture viscosity and thereby reduces workability, while simultaneously accelerating the polymerization rate in fly-ash–based geopolymers [26]. Comparative analyses indicate that KOH, owing to the larger ionic radius of K^+, enhances the dissolution of aluminosilicate species and generates a more open gel network, which translates into comparatively better initial flowability than NaOH-activated systems. In addition, raising the sodium silicate content markedly increases viscosity and diminishes the flowability of the fresh geopolymer paste [15].

Determination of initial and final setting times in geopolymer concrete conventionally follows ASTM C403, which employs a series of standardized penetrometer measurements [27]. However, needle-penetration methods are inherently operator-sensitive and exhibit diminished reliability under elevated curing temperatures [28]. To overcome these limitations, ultrasonic pulse-velocity (UPV) monitoring has been advanced as a non-destructive, high-precision alternative [29, 30]. In UPV testing, time-resolved records of decreasing ultrasonic wave velocity and concomitant increases in material stiffness reflect the progression of geopolymerization and delineate both the initial and final set points [23, 29]. This technique has demonstrated exceptional repeatability and sensitivity, particularly at temperatures above ambient and when assessing the influence of varied alkali activator chemistries, thereby enabling more accurate characterization of setting kinetics in geopolymer systems [24, 28].

Given that previous investigations have employed ultrasonic pulse-velocity (UPV) solely to evaluate the setting kinetics of ordinary Portland cement and no systematic data exist on how varying alkali-activator concentrations affect the setting behavior of slag-based geopolymers, this study applies UPV to accurately characterize the initial and final setting times of fresh geopolymer concrete.

2. Experimental preparation

2.1. Material properties

Fine and coarse aggregates used for specimen preparation were sourced from a nearby fluvial deposit and rigorously characterized per the applicable standards. Particle-size distribution curves, obtained via sieve analysis per ASTM C136 [31], are shown in Fig. 1. The fine aggregate exhibited a saturated surface dry (SSD) bulk specific gravity of 2.65, a fineness modulus of 3.7, and a maximum nominal particle size of 12 mm. The coarse aggregate displayed an SSD bulk specific gravity of 2.64 and was thoroughly washed on-site to remove adhering fines and impurities prior to mix preparation [32].

Blast-furnace slag used in this study is the by-product of the basic oxygen furnace (BOF) steelmaking process. In the BOF route, molten iron derived from iron ore or scrap is charged into the furnace together with fluxing agents such as lime or dolomite. High-pressure oxygen is then blown in to oxidize impurities, which separate as gaseous species and metallic oxides. Upon tapping of the purified steel, the residual slag, composed predominantly of silicates and metal oxides (CaO, SiO_2, Al_2O_3), is recovered. Chemically analogous to Portland cement, this solidified material finds widespread application in the production of slag cements, concrete aggregates, railroad ballast, road subbases, and refractory products.

In this study, Type II Portland cement obtained from a domestic cement works and BOF slag procured from a regional steel producer were employed. The precise chemical compositions of both materials are listed in Table 1, and Fig. 2 presents photographs of the slag alongside the ceramic powder utilized.

In the formulation of geopolymer concretes, the selection of alkali activator, either NaOH or KOH, exerts a profound effect on the microstructure and mechanical properties of the hardened matrix. Although both Na^+ and K^+ possess the same charge, the smaller ionic radius of Na^+ promotes tighter ion-pairing with silicate oligomers, leading to accelerated geopolymerization kinetics but a comparatively less dense gel network.

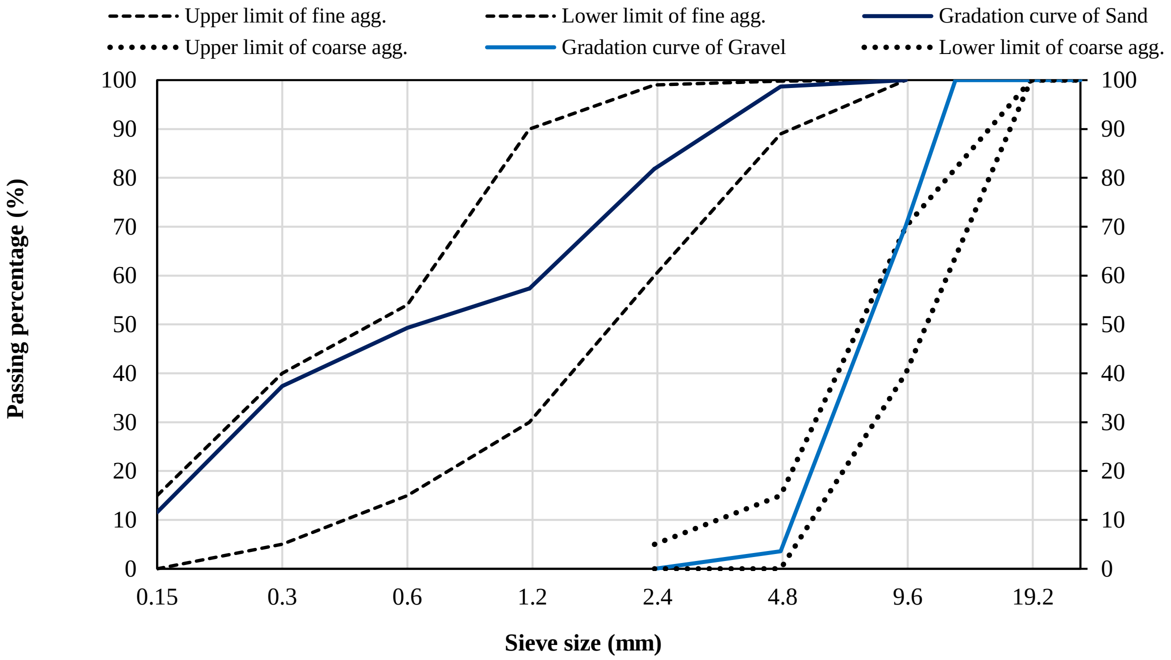

Fig. 1. Grading graph of the fine and coarse aggregates.

Table 1. Chemical analysis of cementing materials.

Type	Chemical Compound (%)										
	CaO	SiO_2	Al_2O_3	Fe_2O_3	SO_3	MgO	Na_2O	K_2O	TiO_2	MnO	L.O.I
Slag	38.32	32.09	15.12	1.23	2.28	7.75	0.42	0.47	1.23	0.99	0.02
Portland cement	64.79	19.99	4.95	3.43	3.12	1.72	0.39	0.61	0.7	-	0.96

Conversely, the larger K^+ favors the formation of bulkier silicate oligomers and thus a denser gel phase, which enhances compressive strength [33].

Fig. 2. Photographs of the (a) blast-furnace slag, and (b) ceramic powder used in the geopolymer concrete mixtures.

Nevertheless, balancing economic and processing considerations, a NaOH concentration of 4–8 M is generally identified as optimal; concentrations above ~10 M not only plateau strength gain but can also induce efflorescence and embrittlement in the geopolymer matrix. Furthermore, a SiO_2/Al_2O_3 molar ratio in the range of 3.3–6.5 is recommended to establish an ideal three-dimensional aluminosilicate network [23]. Figs. 3 and 4 show the NaOH and KOH activator solutions employed in this study.

Fig. 3. Sodium hydroxide (NaOH) flakes used as the alkaline activator in the geopolymer concrete formulation.

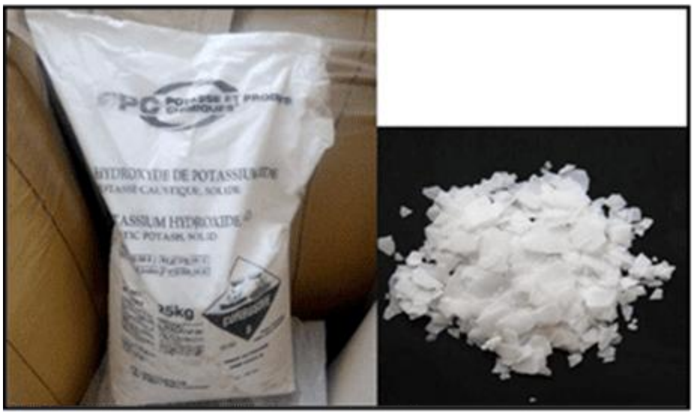

Fig. 4. Potassium hydroxide (KOH) flakes used as the alkaline activator in the geopolymer concrete formulation.

The most critical characteristic of sodium silicate solution (water glass) is its SiO_2/Na_2O molar ratio, which in commercial products typically ranges from 1.5 to 3.2. In general, higher-ratio silicates are more suitable for chemical bonding because the siliceous fraction more readily reacts with cations. However, to maintain a high alkaline concentration while activating pozzolanic materials, lower-ratio silicates are recommended [34]. In the present study, a sodium silicate solution with an SiO_2/Na_2O molar ratio of 2.45 was employed for geopolymer synthesis.

2.2. Mix design

The mix design for the geopolymer concrete series was established by maintaining a fixed sodium silicate-to-caustic soda (NaOH) mass ratio of 2.5. Three alkali-to-slag ratios, 0.4, 0.45, and 0.5, were selected to elucidate the effect of activator dosage on fresh-state rheology and hardened-state strength. In parallel, NaOH solution molarities of 4 M, 6 M, and 8 M were employed to investigate the influence of hydroxide concentration on geopolymerization kinetics and microstructural development. The proportions for the control ordinary Portland cement concrete mix are tabulated in Table 2, while the corresponding geopolymer formulations appear in Table 3.

To assess the impact of mixing sequence on geopolymer performance, two distinct protocols were implemented:

- Simultaneous-addition protocol (Protocol I): The NaOH and sodium silicate solutions were thoroughly blended before their introduction to the slag binder.
- Staged-addition protocol (Protocol II): The NaOH solution was first combined with the slag and allowed to interact for a predefined induction period; subsequently, the sodium silicate was incorporated, and finally, the resulting paste was mixed with the aggregate fraction.

Compressive strength testing at 28 days revealed no statistically significant difference between Protocol I and Protocol II. This finding corroborates the mechanistic understanding that initial alkali attack on the aluminosilicate framework cleaves Al–O–Si bonds to release reactive oligomers, which then condense into a cohesive C–A–S–H–type gel upon contact with silicic species from the sodium silicate [17]. Nonetheless, the staged-addition approach is recommended in practical applications to avoid direct, prolonged exposure of aggregates to high-pH activator solutions, thereby mitigating the risk of deleterious alkali–aggregate reactions and ensuring an optimal interfacial transition zone between binder and aggregate.

Table 2. Mix proportions of OPC specimens.

Mix ID	Component					
	Coarse agg. (kg/m^3)	Fine agg. (kg/m^3)	Cement (kg/m^3)	Water (kg/m^3)	W/C	Slump (mm)
OPC-Code-01	519	1209	400	180	0.4	95
OPC-Code-02	506	1182	400	200	0.5	108

3. Experimental procedure

3.1. Setting time characterization of fresh geopolymer concrete

The early-stage development of the geopolymer's microstructure exerts a decisive influence on its mechanical performance, physical integrity, and long-term durability. Geopolymerization commences when alkaline activators react with aluminosilicate precursors, forming a cohesive inorganic polymer network that dictates the material's behavior in the initial hours post-mixing. In this fresh state, the geopolymer paste exhibits high plasticity and workability, facilitating critical operations such as mixing, transportation, and placement.

Table 3. Mix proportions of geopolymer concrete specimens.

Mix ID	Component											
	Coarse agg. (kg/m^3)	Fine agg. (kg/m^3)	NaOH	KOH	Activator water	Na_2SiO_3	Slag (kg/m^3)	Alk/Slag	Extra water	Molarity	SH/SS	Ceramic (kg/m^3)
AAS.1	519	1209	16.4	-	98	45.7	400	0.4	65	4	2.5	-
AAS.2	519	1209	23.4	-	90.9	45.7	400	0.4	65	6	2.5	-
AAS.3	519	1209	30	-	84	45.7	400	0.4	65	8	2.5	-
AAS.4	512	1196	18.4	-	110.2	51.4	400	0.45	65	4	2.5	-
AAS.5	512	1196	24.4	-	102.2	51.4	400	0.45	65	6	2.5	-
AAS.6	512	1196	33.7	-	94.9	51.4	400	0.45	65	8	2.5	-
AAS.7	506	1182	20.4	-	122.5	57.2	400	0.5	65	4	2.5	-
AAS.8	506	1182	29.3	-	113.6	57.2	400	0.5	65	6	2.5	-
AAS.9	506	1182	37.5	-	105.4	57.2	400	0.5	65	8	2.5	-
AAS.11	506	1064	29.3	-	113.6	57.2	400	0.5	65	6	2.5	118.2
AAS.12	519	1209	-	22.3	92	45.7	400	0.4	65	4	2.5	-
AAS.13	512	1196	-	25.1	103.5	51.4	400	0.45	65	4	2.5	-
AAS.14	506	1182	-	27.9	115	57.2	400	0.5	65	4	2.5	-
AAS.15	529	1235	25.7	-	99.4	50	350	0.5	65	6	2.5	-
AAS.16	484	1128	33	-	127.8	64.3	450	0.5	65	6	2.5	-

As polymerization advances, the paste undergoes progressive stiffening—a phenomenon referred to as setting. The initial setting time defines the duration during which the material retains adequate plasticity and deformation capacity, whereas the final setting time marks the onset of rigidity and the development of measurable mechanical strength. Precise determination of these intervals is essential for optimally scheduling formwork installation, compaction, surface finishing, and formwork removal, as well as for the judicious selection of chemical admixtures (accelerators or retarders) tailored to project requirements. Standardized test methods for quantifying setting behavior in fresh geopolymer and cementitious systems include the Vicat needle penetration test (ASTM C191 [35]), the penetration resistance method (ASTM C403 [27]), and ultrasonic pulse velocity monitoring (BS 1881 [36]).

In the ultrasonic pulse-velocity method, the setting progression of fresh geopolymer concrete (or hydration in Portland cement) can be delineated by the S-shaped velocity-time curve (Fig. 5) and corresponding schematic microstructural illustrations (Fig. 6) across three distinct phases:

Dormant Phase (A → B): Immediately after mixing, pulse velocity remains low and nearly constant (below ~600 m/s), as cement grains or aluminosilicate precursors are dispersed within the aqueous medium and entrapped gas bubbles (Fig. 6a). Up to point B, gradual dissolution of fine particles and surface coating of larger grains commences, giving rise to nascent solid clusters (Fig. 6b), yet no continuous propagation path exists for the ultrasonic waves.

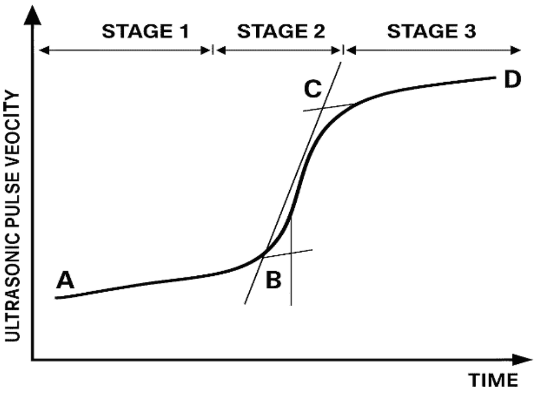

Fig. 5. Schematic illustration of UPV monitoring during the setting stages of fresh geopolymer concrete [37].

Acceleration Phase (B → C): With the formation of aluminosilicate gel products (e.g., ettringite analogues) and the development of an interconnected structural network (Fig. 6c), pulse velocity rapidly increases from approximately 600 m/s to more than 3,500 m/s—corresponding to the onset of measurable mechanical strength.

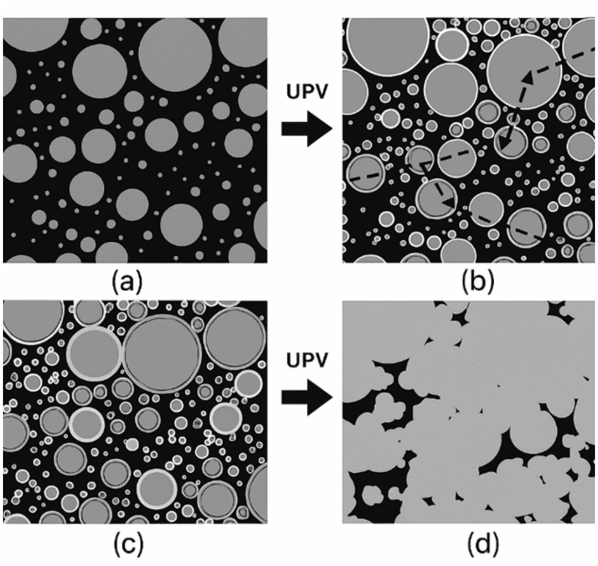

Fig. 6. Microstructural evolution from dispersed particles to a continuous solid network.

Deceleration Phase (C → D): Upon the completion of particle binding and the filling of capillary pores with hydrated reaction products (Fig. 6d), the pulse velocity gradually approaches its asymptotic maximum, signifying the near-end of major structural reactions.

3.2. Fabrication of the ultrasonic setting test mold

The apparatus used to determine concrete setting time by the ultrasonic method—allowing wave-velocity measurements at arbitrary intervals immediately after casting was built by the system introduced by Reinhardt and Grosse [38], first realized at the University of Stuttgart in 2000 (see schematic in Fig. 7). The so-called “Freshcon” mold consists of two PMMA (acrylic) plates, each measuring 15 × 200 × 500 mm, mounted parallel to one another at a separation of 120 mm utilizing four steel shafts. To ensure that ultrasonic pulses do not bypass the specimen at the edges, the plates are sufficiently long, and a U-shaped rubber sponge (30 × 120 × 500 mm) is inserted between them; this sponge minimizes wave scattering inside the mold. Each plate is drilled at its center to accommodate the transmitting and receiving ultrasonic transducers, which are inserted through these holes and brought into contact with the plate surfaces. Ultrasonic measurements were then carried out using a PUNDIT device (fundamental frequency 54 kHz) every 5 minutes during the first hour after casting, and subsequently at 15-minute intervals.

The transmitting transducer was placed in direct contact with the Plexiglas plate and aligned through the full thickness of the concrete specimen, as shown in Fig. 7. After traversing the concrete, the ultrasonic vibrations were captured by the receiving transducer, which was similarly coupled to the opposite Plexiglas surface. The receiver measured the transit time of the pulsed waves through the specimen; by dividing the known path length (i.e., the straight-line distance between the transducers) by this measured time, the ultrasonic pulse velocity was obtained. This technique is applicable not only for determining setting characteristics, compressive strength, and elastic modulus of concrete, but also for assessing durability parameters—such as crack detection and damage evaluation.

Ultrasonic pulse velocities were recorded using a PUNDIT system following BS 1881 [36]. Fig. 8 illustrates the laboratory arrangement of the PUNDIT apparatus, equipped with 54 kHz transducers and a calibrated Plexiglas reference cylinder. The geometrical and acoustic properties of this cylinder are precisely known, and it is employed before each test to zero the instrument via the variable-delay control unit.

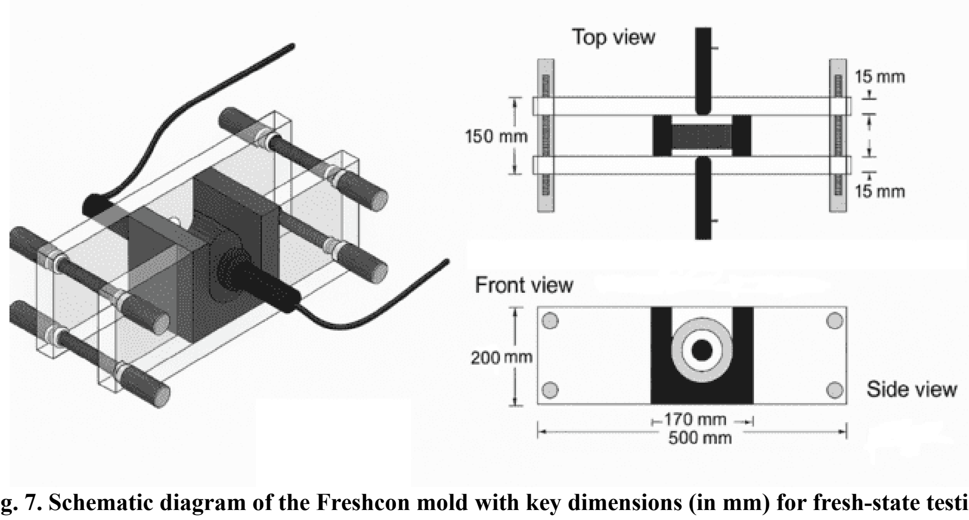

Fig. 7. Schematic diagram of the Freshcon mold with key dimensions (in mm) for fresh-state testing.

The pulse velocity, V, was calculated using Eq. 1:

$$V = \frac{L}{\Delta \mathrm{t}} \tag{1}$$

where L is the distance between transducer faces and Δt is the measured transit time.

Fig. 8. Calibration of the PUNDIT device.

4. Results and discussions

As illustrated in Fig. 9, ultrasonic waves are transmitted from one probe into the fresh concrete mold and received by the opposing probe. The wave transit time is recorded at predetermined intervals with microsecond precision. Using Eq. 1, the pulse velocity is then calculated. Finally, the velocity–time profile is plotted for each concrete sample, enabling a non-destructive rheological assessment of the concrete's structural evolution over time.

According to the UPV curves in Figs. 10 to 12, raising the NaOH molarity from 4 M to 8 M markedly accelerates the early hardening of geopolymer concrete. For example, at an alkali-to-slag ratio of 0.4 (Fig. 10), the 30-minute UPV values for AAS.1 (4 M), AAS.2 (6 M), and AAS.3 (8 M) were all approximately 600 m/s. After 120 minutes, these rose to roughly 970 m/s, 1,700 m/s, and 2,500 m/s, respectively, and by 180 minutes reached 1,240 m/s, 2,800 m/s, and 3,550 m/s. By 360 minutes, AAS.2 and AAS.3 approached their plateau velocities of about 4,200–4,280 m/s, whereas AAS.1 attained only ≈2,000 m/s. The steeper velocity increases with higher OH^- concentration reflect more rapid aluminosilicate dissolution and N–A–S–H gel formation, confirming hydroxide concentration as the principal factor in shortening both initial and final setting phases [7, 39].

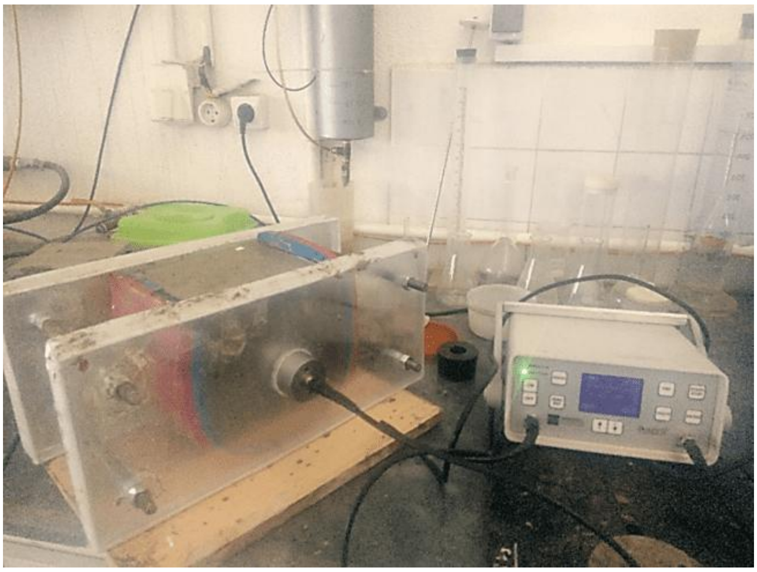

Fig. 9. UPV testing of fresh concrete using the Freshcon mold and PUNDIT device.

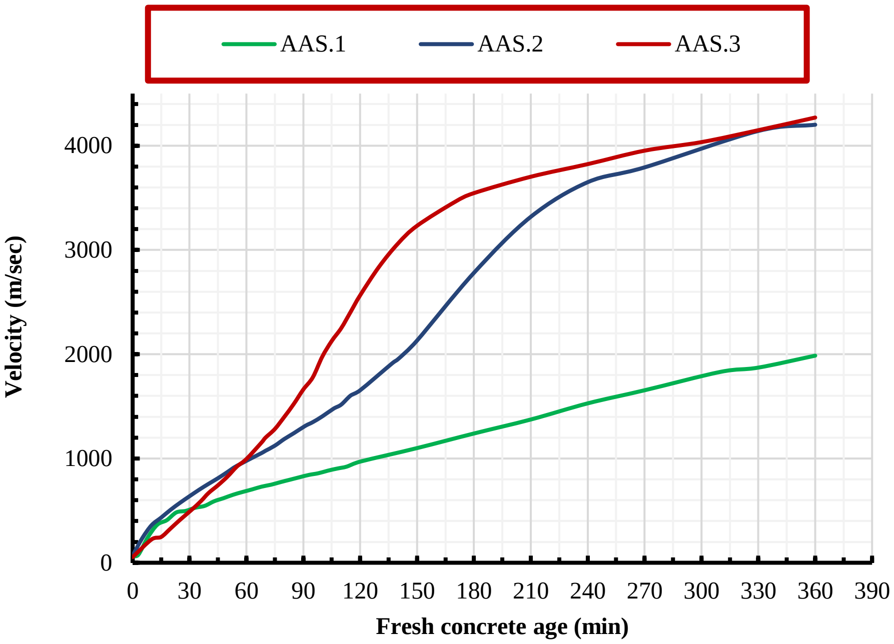

Fig. 10. Effect of NaOH solution molarity on the setting-time curve of concrete with an alkali-to-slag ratio of 0.4.

In Figs. 13 to 15, increasing the total dosage of the alkaline activator accelerates the heat evolution reaction and shortens the induction period, indicating more rapid slag dissolution and earlier formation of C–(A)–S–H gels [40]. This behavior is mechanistically attributed to the expedited removal of Ca^{2+} ions from the pore solution, which amplifies the concentration gradient between the slag surface and the aqueous phase, thereby promoting further slag dissolution and faster gel precipitation [41]. Meanwhile, by maintaining a constant silica-to-alkali modulus (SiO_2/Na_2O) across all tests, the study isolates the effect of total alkali and silicate ion content on reaction kinetics [40, 42].

Fig. 16 compares the setting-time profiles of geopolymer concretes activated with 4 M NaOH versus 4 M KOH. The markedly accelerated setting observed in the KOH-activated system can be attributed to the distinct physicochemical properties of the K^+ ion: its lower hydration enthalpy (≈–322 kJ/mol compared to –406 kJ/mol for Na^+) results in a more labile hydration shell that releases OH^- more readily for C–(A)–S–H gel formation. Furthermore, the larger ionic radius of K^+ (1.38 Å vs. 1.02 Å for Na^+) reduces the structuring of its solvation sphere and lowers the viscosity of the activator solution, thereby enhancing the diffusivity of alkali and dissolved slag species [43]. This increased ionic mobility expedites the depolymerization of the aluminosilicate network and the nucleation of gel phases, culminating in a pronounced reduction of both initial and final setting times.

Fig. 17 illustrates the effect of varying ground-granulated blast-furnace slag (GGBFS) dosages on the setting behavior of geopolymer concrete mixtures. As anticipated, increasing the slag content from 350 kg/m³ (AAS.15) to 450 kg/m³ (AAS.16) accelerates hydration reactions and reduces both initial and final setting times. This enhancement is driven by the additional calcium provided by the slag, which markedly promotes C–S–H and C–A–S–H gel formation. Consequently, higher slag proportions yield more rapid gel nucleation and growth, resulting in faster stiffening of the geopolymer matrix.

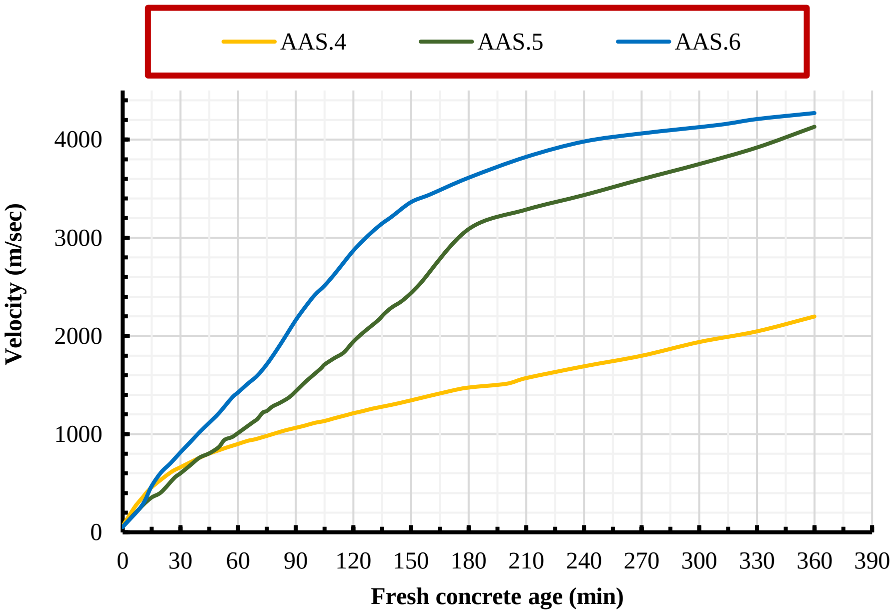

Fig. 11. Effect of NaOH solution molarity on the setting-time curve of concrete with an alkali-to-slag ratio of 0.45.

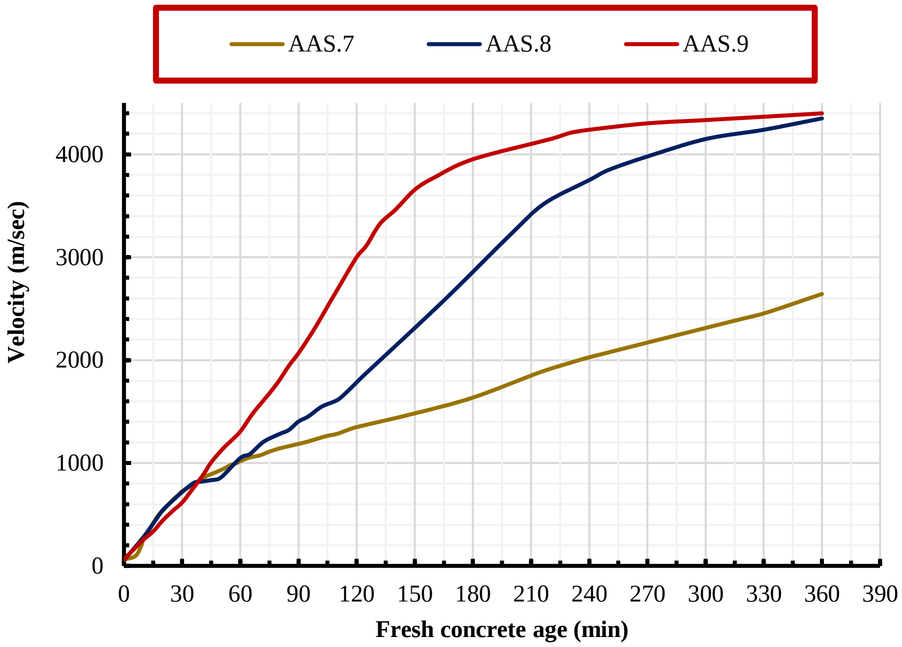

Fig. 12. Effect of NaOH solution molarity on the setting-time curve of concrete with an alkali-to-slag ratio of 0.5.

Fig. 18 examines the effect of substituting 10 wt.% of natural fine aggregate with ceramic tile waste powder in the geopolymer blend. The results demonstrate that this level of replacement exerts no discernible influence on the setting kinetics of the geopolymer concrete.

Fig. 19 presents a comparative analysis of the setting behavior of the investigated geopolymer mixtures versus ordinary Portland cement (OPC) concretes. The ultrasonic pulse-velocity profiles reveal that all geopolymer samples (AAS.1 through AAS.16) enter both initial and final setting phases markedly earlier than the OPC references (OPC-Code-01, OPC-Code-02, and CEM I 42.5 [44]). On average, the onset of the sharp velocity increase commonly taken as the initial set threshold of approximately 1,000 m/s occurs between 20 and 50 minutes after casting for the geopolymer specimens, whereas none of the OPC samples reach this velocity even after 240 minutes. For instance, OPC-Code-01 and OPC-Code-02 attain 1,000 m/s at roughly 300 minutes and 360 minutes, respectively, while CEM I 42.5 reaches this stage between 200 and 220 minutes. Final setting indicated by pulse velocities in the 3,000–3,500 m/s range, and the commencement of the tertiary slope occurs for geopolymer concretes between 90 and 180 minutes, with most AAS mixtures stabilizing near 3,500–4,000 m/s in under 3 hours. In contrast, OPC-Code-01 requires approximately 12 hours (720 minutes) to reach 3,500 m/s, OPC-Code-02 about 13–14 hours (780–840 minutes), and CEM I 42.5 around 10 hours (600–650 minutes). Thus, the geopolymer systems demonstrate polymerization and hardening rates that are on average 5–8 times faster than those of ordinary Portland cement concretes.

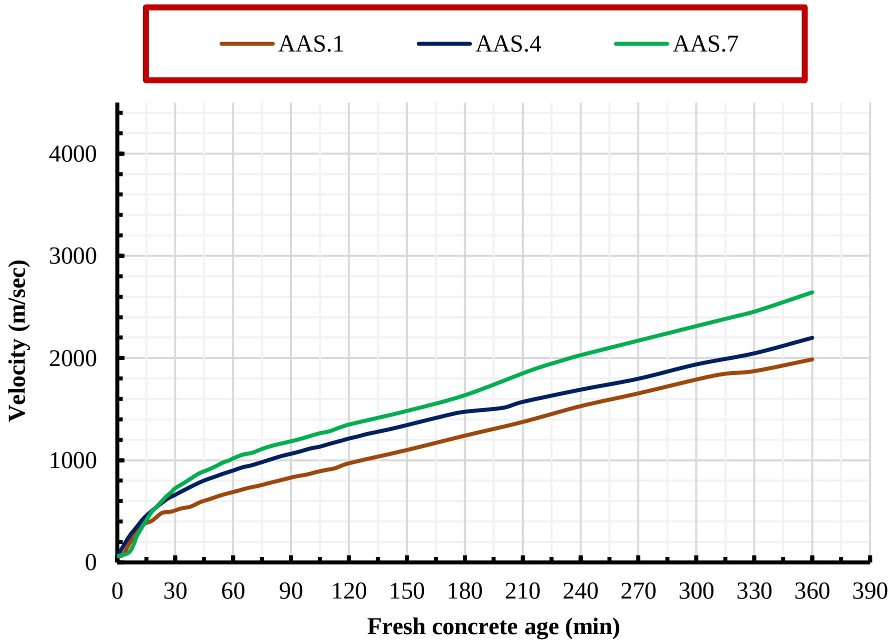

Fig. 13. Setting-time curves for geopolymer concrete with varying alkali-to-slag ratios activated by 4 M NaOH.

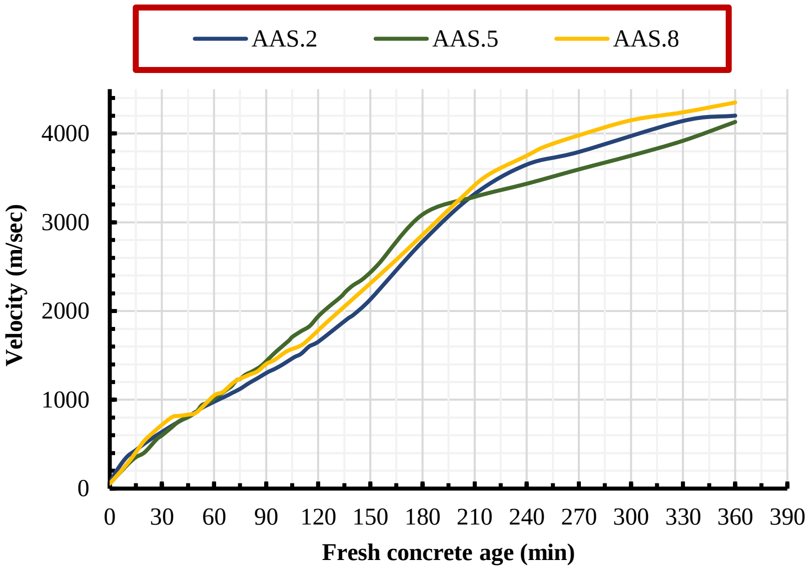

Fig. 14. Setting-time curves for geopolymer concrete with varying alkali-to-slag ratios activated by 6 M NaOH.

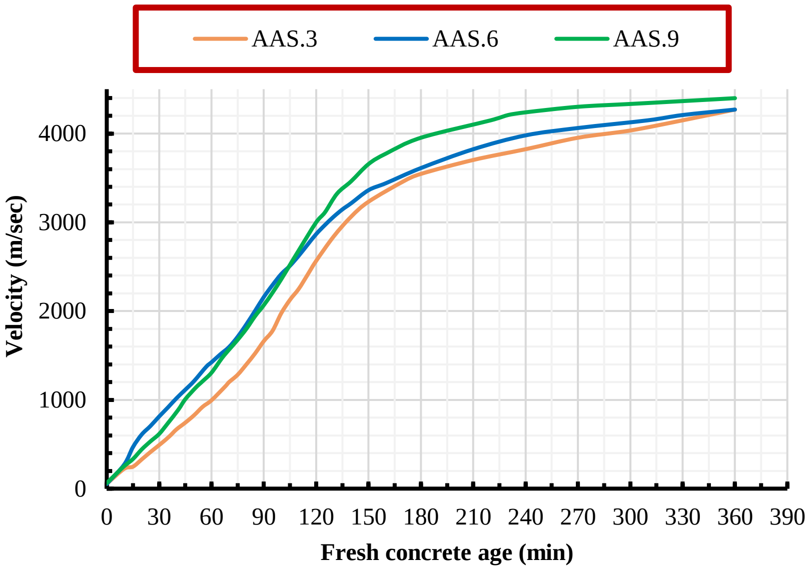

Fig. 15. Setting-time curves for geopolymer concrete with varying alkali-to-slag ratios activated by 8 M NaOH.

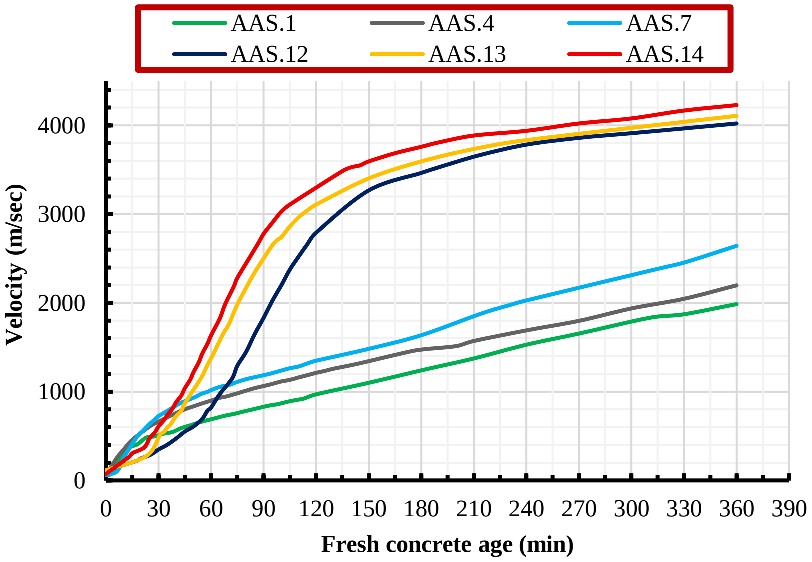

Fig. 16. Comparison of setting-time curves for geopolymer concrete activated with different alkaline solutions.

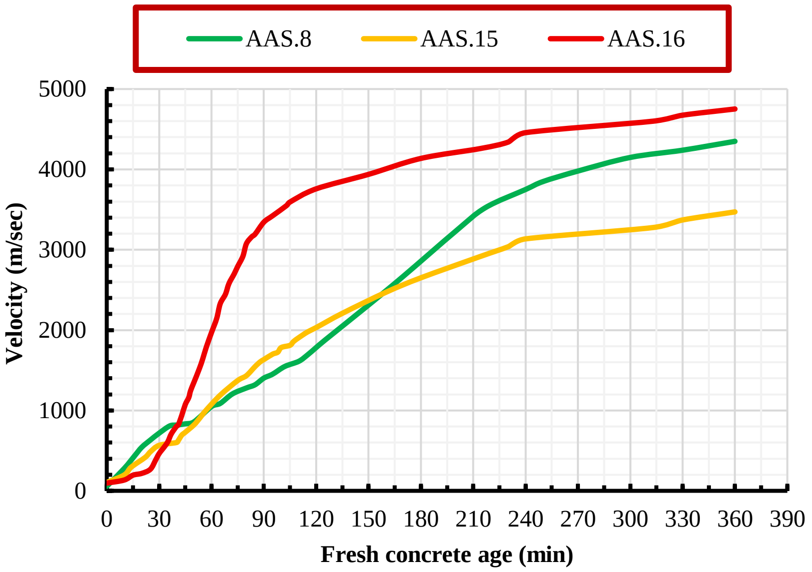

Fig. 17. Setting-time curves of geopolymer concrete mixtures with varying GGBFS contents.

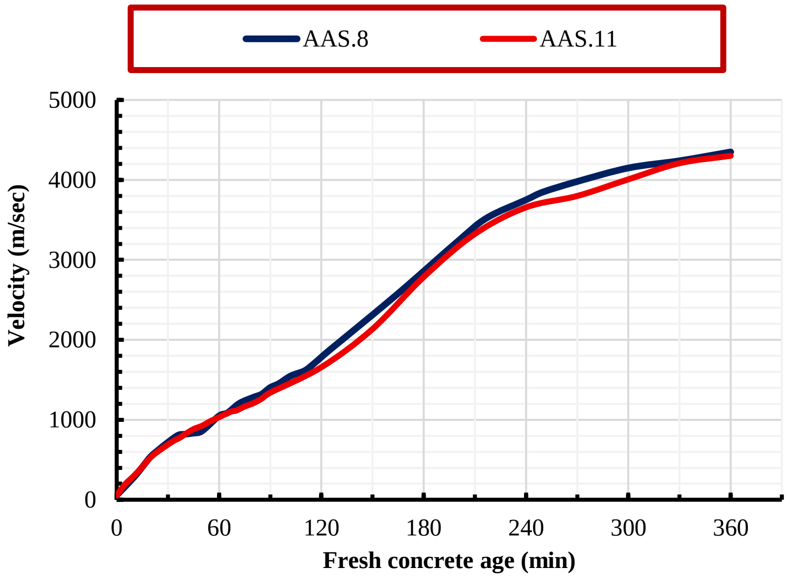

Fig. 18. Comparison of setting-time curves between the reference mix and the mix with 10% ceramic tile powder replacing fine aggregate.

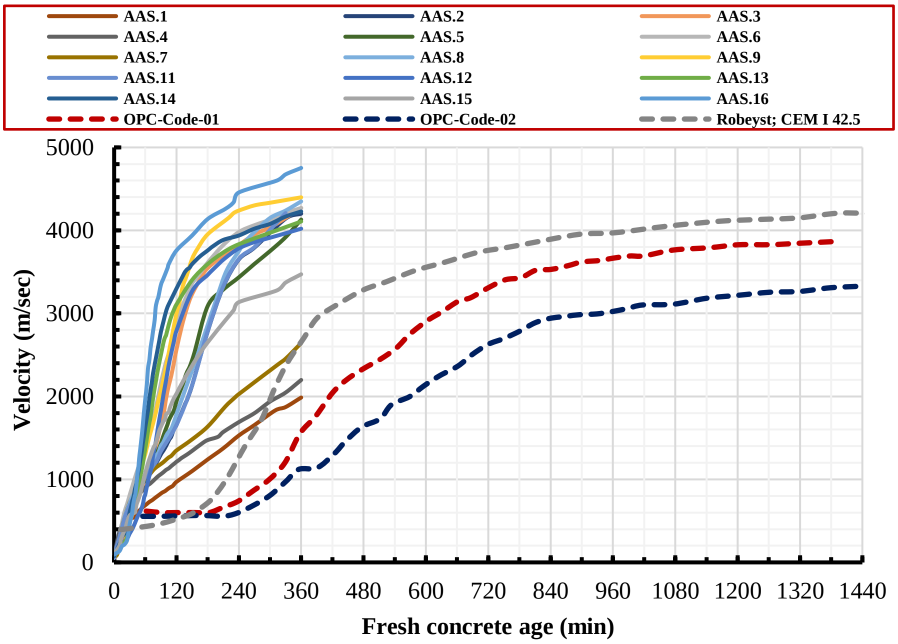

Fig. 19. Comparison of setting-time curves for OPC and slag-based geopolymer concrete.

5. Conclusions

In this study, the ultrasonic method was applied to assess the setting stages of slag-based geopolymer concrete at early ages. The experimental results indicate that this method can provide a comprehensive depiction of the polymerization process and the development of the microstructure of this type of concrete with a chosen composition.

All the ultrasonic velocity curves obtained (except those for samples containing 4 M sodium hydroxide (NaOH), which required more time to reach the final setting point) exhibited a similar three-phase pattern: an initial phase of very low, nearly constant velocity; a second phase with an abrupt increase in velocity; and a third phase during which the rate of increase in velocity slows after a few minutes. As in ordinary concrete, the initial setting time of the geopolymer mixtures was taken as the inflection point of this curve, and the final setting time as the onset of the third phase.

The results also show that slag-based geopolymer concretes set much faster than OPC concrete, with their polymerization reaction and final hardening occurring on average 6–8 times faster than those of OPC concrete. Furthermore, the initial and final setting times decrease as the molarity of the alkaline activator is increased: the alkaline hydroxide initially cleaves the Al–Si bonds and dissolves aluminum ions (which act as polymerization catalysts), and the addition of soluble sodium silicate results in the formation of a hydrated alkali aluminosilicate gel.

Raising the activator concentration from 4 M to 6 M dramatically shortens both the initial and final setting times, whereas a further increase to 8 M results in only a slight additional reduction. Similarly, in mixtures with a fixed NaOH molarity, increasing the overall alkaline solution-to-slag ratio from 0.4 to 0.5 accelerates slag activation and increases the heat of reaction, leading to shorter initial and final setting times for the fresh concrete. Increasing the slag content itself also accelerates the hydration reactions and further reduces the setting time, because the extra calcium in the slag greatly accelerates the process and promotes the rapid formation of C–S–H and C–A–S–H phases. In addition, using potassium hydroxide as the alkaline activator, compared with NaOH at the same molarity, markedly reduces the initial and final setting times of the fresh concrete, likely due to the chemical properties of the potassium ion.

Finally, the UPV method, used in conjunction with a Freshcon mold, is recommended as an appropriate test for assessing the setting times of slag-based geopolymer concrete. Although the rapid setting of geopolymer mixtures in volumetric applications may lead to the formation of cold joints and impose significant time constraints on molding processes, this property—by accelerating the rate of initial hardening—offers considerable advantages for the production of precast elements and the application of geopolymer shotcrete, particularly in tunnel rock support systems. Consequently, the high performance of geopolymer shotcrete justifies further in-depth evaluation in future research. Such studies should focus on critical aspects, including long-term durability and fire resistance. These investigations, which may involve advanced laboratory techniques such as thermomechanical analysis and numerical modeling using finite element methods, not only support global initiatives aimed at reducing greenhouse gas emissions in the construction industry but also contribute to advancing specialized knowledge in the field of geopolymer materials and their innovative applications in civil engineering.

Furthermore, the establishment of an independent standard specifically tailored to the setting behavior of geopolymers, coupled with comprehensive field validation of the UPV methodology under realistic curing and confining conditions, is crucial for the advancement of future research in this domain.

Statements & Declarations

Author contributions

Nader Sabeti: Conceptualization, Investigation, Methodology, Formal analysis, Resources, Writing - Original Draft, Writing - Review & Editing.

Funding

The authors received no financial support for the research, authorship, and/or publication of this article.

Data availability

The data presented in this study will be available on interested request from the corresponding author.

Declarations

The authors declare no conflict of interes.

References

[1] Nodehi, M., Taghvaee, V. M. Alkali-Activated Materials and Geopolymer: a Review of Common Precursors and Activators Addressing Circular Economy. Circular Economy and Sustainability, 2022; 2: 165-196. doi:10.1007/s43615-021-00029-w.

[2] Behforouz, B., Balkanlou, V. S., Naseri, F., Kasehchi, E., Mohseni, E., Ozbakkaloglu, T. Investigation of eco-friendly fiber-reinforced geopolymer composites incorporating recycled coarse aggregates. International Journal of Environmental Science and Technology, 2020; 17: 3251-3260. doi:10.1007/s13762-020-02643-x.

[3] Amran, M., Debbarma, S., Ozbakkaloglu, T. Fly ash-based eco-friendly geopolymer concrete: A critical review of the long-term durability properties. Construction and Building Materials, 2021; 270: 121857. doi:10.1016/j.conbuildmat.2020.121857.

[4] Turner, L. K., Collins, F. G. Carbon dioxide equivalent (CO2-e) emissions: A comparison between geopolymer and OPC cement concrete. Construction and Building Materials, 2013; 43: 125-130. doi:10.1016/j.conbuildmat.2013.01.023.

[5] Robbie, A. Global CO2 emissions from cement production. Earth System Science Data, 2017; 10: 195-217. doi:10.5194/essd-10-195-2018.

[6] Shi, C., Jiménez, A. F., Palomo, A. New cements for the 21st century: The pursuit of an alternative to Portland cement. Cement and Concrete Research, 2011; 41: 750-763. doi:10.1016/j.cemconres.2011.03.016.

[7] Matthes, W., Vollpracht, A., Villagrán, Y., Kamali-Bernard, S., Hooton, D., Gruyaert, E., Soutsos, M., De Belie, N. Ground Granulated Blast-Furnace Slag. In: N. De Belie, M. Soutsos, E. Gruyaert editors. Properties of Fresh and Hardened Concrete Containing Supplementary Cementitious Materials: State-of-the-Art Report of the RILEM Technical Committee 238-SCM, Working Group 4. Cham: Springer International Publishing; 2018. p. 1-53. doi:10.1007/978-3-319-70606-1_1.

[8] Davidovits, J. Geopolymers. Journal of thermal analysis, 1991; 37: 1633-1656. doi:10.1007/BF01912193.

[9] van Deventer, J. S. J., Provis, J. L., Duxson, P., Lukey, G. C. Reaction mechanisms in the geopolymeric conversion of inorganic waste to useful products. Journal of Hazardous Materials, 2007; 139: 506-513. doi:10.1016/j.jhazmat.2006.02.044.

[10] Palomo, A., Krivenko, P., Garcia-Lodeiro, I., Kavalerova, E., Maltseva, O., Fernández-Jiménez, A. A review on alkaline activation: new analytical perspectives. Materiales de Construcción, 2014; 64: e022. doi:10.3989/mc.2014.00314.

[11] Wang, Y., Zhang, S., Li, G., Shi, X. Effects of alkali-treated recycled carbon fiber on the strength and free drying shrinkage of cementitious mortar. Journal of Cleaner Production, 2019; 228: 1187-1195. doi:10.1016/j.jclepro.2019.04.295.

[12] Fernández-Jiménez, A., Palomo, A. Composition and microstructure of alkali activated fly ash binder: Effect of the activator. Cement and Concrete Research, 2005; 35: 1984-1992. doi:10.1016/j.cemconres.2005.03.003.

[13] White, C. E., Provis, J. L., Proffen, T., van Deventer, J. S. J. Molecular mechanisms responsible for the structural changes occurring during geopolymerization: Multiscale simulation. AIChE Journal, 2012; 58: 2241-2253. doi:10.1002/aic.12743.

[14] Lolli, F., Manzano, H., Provis, J. L., Bignozzi, M. C., Masoero, E. Atomistic Simulations of Geopolymer Models: The Impact of Disorder on Structure and Mechanics. ACS Applied Materials & Interfaces, 2018; 10: 22809-22820. doi:10.1021/acsami.8b03873.

[15] Dai, X., Aydin, S., Yardimci, M. Y., Lesage, K., De Schutter, G. Early age reaction, rheological properties and pore solution chemistry of NaOH-activated slag mixtures. Cement and Concrete Composites, 2022; 133: 104715. doi:10.1016/j.cemconcomp.2022.104715.

[16] Aiken, T. A., Kwasny, J., Sha, W., Tong, K. T. Mechanical and durability properties of alkali-activated fly ash concrete with increasing slag content. Construction and Building Materials, 2021; 301: 124330. doi:10.1016/j.conbuildmat.2021.124330.

[17] Fang, Y., Zhuang, K., Zheng, D., Guo, W. The Influence of Alkali Content on the Hydration of the Slag-Based Geopolymer: Relationships between Resistivity, Setting, and Strength Development. Polymers, 2023; 15: doi:10.3390/polym15030518.

[18] Taghvayi, H., Behfarnia, K., Khalili, M. The Effect of Alkali Concentration and Sodium Silicate Modulus on the Properties of Alkali-Activated Slag Concrete. Journal of Advanced Concrete Technology, 2018; 16: 293-305. doi:10.3151/jact.16.293.

[19] Ahmed, H. U., Mohammed, A. S., Mohammed, A. A., Faraj, R. H. Systematic multiscale models to predict the compressive strength of fly ash-based geopolymer concrete at various mixture proportions and curing regimes. PLOS ONE, 2021; 16: e0253006. doi:10.1371/journal.pone.0253006.

[20] Arularasi, V., Thamilselvi, P., Avudaiappan, S., Saavedra Flores, E. I., Amran, M., Fediuk, R., Vatin, N., Karelina, M. Rheological Behavior and Strength Characteristics of Cement Paste and Mortar with Fly Ash and GGBS Admixtures. Sustainability, 2021; 13: doi:10.3390/su13179600.

[21] Ansell, A. Investigation of shrinkage cracking in shotcrete on tunnel drains. Tunnelling and Underground Space Technology, 2010; 25: 607-613. doi:10.1016/j.tust.2010.04.006.

[22] Jameel, F., Sjölander, A., Ansell, A. Testing the in situ properties of wet-mix shotcrete at early age. ed. Boca Raton (FL): CRC Press; 2025.

[23] Aldawsari, S., Kampmann, R., Harnisch, J., Rohde, C. Setting Time, Microstructure, and Durability Properties of Low Calcium Fly Ash/Slag Geopolymer: A Review. Materials, 2022; 15: doi:10.3390/ma15030876.

[24] Gebregziabiher, B. S., Thomas, R. J., Peethamparan, S. Temperature and activator effect on early-age reaction kinetics of alkali-activated slag binders. Construction and Building Materials, 2016; 113: 783-793. doi:10.1016/j.conbuildmat.2016.03.098.

[25] Jiang, X., Zhang, Y., Xiao, R., Polaczyk, P., Zhang, M., Hu, W., Bai, Y., Huang, B. A comparative study on geopolymers synthesized by different classes of fly ash after exposure to elevated temperatures. Journal of Cleaner Production, 2020; 270: 122500. doi:10.1016/j.jclepro.2020.122500.

[26] Feng, X., Wang, Y., Li, L., Jiang, Z., Zhou, G., Wu, Q., Wang, T. Experimental investigation on physical properties and early-stage strength of ultrafine fly ash-based geopolymer grouting material. Construction and Building Materials, 2024; 441: 137526. doi:10.1016/j.conbuildmat.2024.137526.

[27] American Society for Testing and Materials (ASTM). ASTM C403/C403M-16: Standard Test Method for Time of Setting of Concrete Mixtures by Penetration Resistance. West Conshohocken (PA): ASTM International; 2016. doi:10.1520/C0403_C0403M-16.

[28] Lee, T., Lee, J. Setting time and compressive strength prediction model of concrete by nondestructive ultrasonic pulse velocity testing at early age. Construction and Building Materials, 2020; 252: 119027. doi:10.1016/j.conbuildmat.2020.119027.

[29] Li, Z., Alfredo Flores Beltran, I., Chen, Y., Šavija, B., Ye, G. Early-age properties of alkali-activated slag and glass wool paste. Construction and Building Materials, 2021; 291: 123326. doi:10.1016/j.conbuildmat.2021.123326.

[30] Sathiparan, N., Jayasundara, W. G. B. S., Samarakoon, K. S. D., Banujan, B. Prediction of characteristics of cement stabilized earth blocks using non-destructive testing: Ultrasonic pulse velocity and electrical resistivity. Materialia, 2023; 29: 101794. doi:10.1016/j.mtla.2023.101794.

[31] American Society for Testing and Materials (ASTM). ASTM C136/C136M: Standard Test Method for Sieve Analysis of Fine and Coarse Aggregates. West Conshohocken (PA): ASTM International; 2019. doi:10.1520/C0136_C0136M-14.

[32] American Society for Testing and Materials (ASTM). ASTM C33/C33M: Standard Specification for Concrete Aggregates. West Conshohocken (PA): ASTM International; 2018. doi:10.1520/C0033_C0033M-18.

[33] Zhang, H., Li, L., Long, T., Sarker, P. K., Shi, X., Cai, G., Wang, Q. The Effect of Ordinary Portland Cement Substitution on the Thermal Stability of Geopolymer Concrete. Materials, 2019; 12: doi:10.3390/ma12162501.

[34] Naghizadeh, A., Ekolu, S. Effect of different mixture parameters on the setting time of fly ash/rice husk ash-based geopolymer mortar. MATEC Web of Conferences, 2022; 361: 05001. doi:10.1051/matecconf/202236105001.

[35] American Society for Testing and Materials (ASTM). ASTM C191: Standard Test Method for Time of Setting of Hydraulic Cement by Vicat Needle. West Conshohocken (PA): ASTM International; 2000. doi:10.1520/C0191-21.

[36] British Standards Institution. BS 1881-203: Testing concrete recommendations for measurement of velocity of ultrasonic pulses in concrete. United Kingdom: BS Standard; 1986.

[37] British Standards Institution. BS EN 196-3: Methods of testing cement - Determination of setting times and soundness. United Kingdom: BS Standard; 2016.

[38] Reinhardt, H. W., Grosse, C. U. Continuous monitoring of setting and hardening of mortar and concrete. Construction and Building Materials, 2004; 18: 145-154. doi:10.1016/j.conbuildmat.2003.10.002.

[39] Huseien, G. F., Sam, A. R. M., Shah, K. W., Mirza, J., Tahir, M. M. Evaluation of alkali-activated mortars containing high volume waste ceramic powder and fly ash replacing GBFS. Construction and Building Materials, 2019; 210: 78-92. doi:10.1016/j.conbuildmat.2019.03.194.

[40] Xu, W., Tang, Z., Xie, Y., Long, G., Zhu, H., Kai, M., Peng, L., Wang, L., Zaland, S. Effect of synthesis parameters on the alkali activation reaction degree and the relationship between reaction degree and microstructure of fly ash-based geopolymers. Journal of Building Engineering, 2024; 93: 109874. doi:10.1016/j.jobe.2024.109874.

[41] Yang, C., Liu, J., Liu, L., Kuang, L., Zhang, S., Chen, Z., Li, J., Shi, C. Effects of different activators on autogenous shrinkage of alkali-activated slag cement. Construction and Building Materials, 2024; 446: 138018. doi:10.1016/j.conbuildmat.2024.138018.

[42] Mehdizadeh, H., Najafi Kani, E. Rheology and apparent activation energy of alkali activated phosphorous slag. Construction and Building Materials, 2018; 171: 197-204. doi:10.1016/j.conbuildmat.2018.03.130.

[43] Abdul Rahim, R. H., Rahmiati, T., Azizli, K. A., Man, Z., Nuruddin, M. F., Ismail, L. Comparison of Using NaOH and KOH Activated Fly Ash-Based Geopolymer on the Mechanical Properties. Materials Science Forum, 2015; 803: 179-184. doi:10.4028/www.scientific.net/MSF.803.179.

[44] Robeyst, N., Gruyaert, E., Grosse, C. U., De Belie, N. Monitoring the setting of concrete containing blast-furnace slag by measuring the ultrasonic p-wave velocity. Cement and Concrete Research, 2008; 38: 1169-1176. doi:10.1016/j.cemconres.2008.04.006.

Civil Engineering and Applied Solutions, 2025; 1(3): 62–69

Civil Engineering and Applied Solutions

Research Article

journal homepage: ceas.journals.umz.ac.ir

The Effect of Candidate Routes Alignment over Transit Coverage in a Grid Network

Amirali Zarrinmehr [a*], Mohammad Mehdi Ghasemi [b]

[a] *Department of Civil Engineering, Faculty of Engineering and Technology, University of Mazandaran, Babolsar, Iran*
[b] *Department of Business and Management, Aston Business School, Birmingham, United Kingdom*

ARTICLE INFO

Keywords:
Transit routes
Network design
Coverage
Grid-structured networks
Restricted/unrestricted candidate routes

Article history:
Received 05 May 2025
Accepted 17 May 2025
Available online 01 August 2025

ABSTRACT

The design of public transportation (transit) route networks involves identifying the most efficient configuration of routes in an urban setting so as to maximize an objective function, such as network coverage, within the available budget. This problem is generally addressed through two key stages: the generation of potential candidate routes to be selected and the subsequent selection of final routes. According to the literature, the "pool" of candidate routes in the first stage plays a critical role in determining the quality of the selected routes in the second stage. However, in certain network topologies, such as grid-structured networks, urban planners often prefer introducing candidate routes oriented horizontally (east-west) or vertically (south-north). The impact of restricting the candidate routes to exclusively horizontal and vertical routes has not been studied much in existing research. To address this gap, this study examines two scenarios: (1) unrestricted candidate routes and (2) candidate routes restricted to horizontal and vertical orientations. The results averaged for a 6×10 grid network suggest that adopting horizontally and vertically restricted candidate routes results in only a 2% reduction in network coverage compared to using unrestricted candidate routes.

1. Introduction and research background

Public transportation systems are recognized as an integral part of modern cities and serve as a cornerstone for sustainable urban development. Encouraging the use of public transit through the design of strategically efficient routes can help modern cities significantly reduce their fuel consumption, thereby mitigating greenhouse gas emissions and contributing to their environmental preservation. Furthermore, an affordable transit system improves the overall quality of urban life by minimizing travel times, conserving energy, and enhancing convenience for city inhabitants [1, 2]. Given these multifaceted benefits, public transportation has emerged as a recurrent and pivotal theme in transportation planning literature over recent decades.

The process of transit planning comprises a variety of decision-making problems, ranging from long-term decisions with decades-long implications to short-term operational choices made on a daily or weekly basis. Researchers have adopted a structured framework for this process by breaking it down into separate steps of route design, frequency setting, and vehicle/crew scheduling [3]. Among these steps, transit routes design is the most important part as it entails strategic decisions that substantially influence subsequent steps of the planning process [4]. As a result, a great deal of research has been dedicated to developing innovative methodologies and tools, only to identify transit routes configuration in recent decades [1, 2, 5].

The problem of transit route design is focused on determining the optimal configuration of public transportation routes within a city network, with the aim of optimizing a specified objective function. This must be achieved within a limited budget, which in turn, necessitates the efficient allocation of resources [4]. At its core, the problem of network design falls under the category of NP-hard problems, which are characterized by their intractable computational complexity [6]. In practice, this means that obtaining

---

* Corresponding author.
E-mail addresses: azarinmehr@umz.ac.ir (A. Zarrinmehr).

https://doi.org/10.22080/ceas.2025.29167.1007

ISSN: 3092-7749/© 2025 The Author(s). Published by University of Mazandaran.
This article is an open access article distributed under the terms and conditions of the Creative Commons Attribution (CC-BY) license (https://creativecommons.org/licenses/by/4.0/deed.en)

How to cite this article: Zarrinmehr, A., Mehdi Ghasemi, M. The Effect of Candidate Routes Alignment over Transit Coverage in a Grid Network. Civil Engineering and Applied Solutions. 2025; 1(3): 62–69. doi:10.22080/ceas.2025.29167.1007.

exact solutions (i.e., "global optimal" configurations in the search space of the problem) becomes impossible for large-scale networks due to the exponential growth in computational requirements. As a result, the research relies on non-exact solution methods, including heuristic or meta-heuristic algorithms, to address this problem effectively. These algorithms, designed to provide near-optimal solutions within a reasonable timeframe, have proven to be indispensable tools for tackling large transit route design problems in urban environments [7, 8].

The transit routes design problem is generally approached as a two-stage process: route generation followed by route selection. In the first stage, a comprehensive set of candidate routes is created, incorporating alternatives with varying shapes and lengths. In the second stage, the optimal routes configuration is identified by selecting from the generated pool, while maintaining budgetary constraints. Various aspects of this problem have been explored in the research background [9]. Numerous studies have proposed a variety of solution approaches, ranging from the development of innovative heuristic algorithms [8] to the application of metaheuristic algorithms, such as genetic algorithms [10, 11], ant colony optimization [12], and simulated annealing [13]. The objective functions considered in these studies often include maximizing transit ridership [14], network coverage [15], equity measures [16], or minimizing the number of transfers over transit routes [10], system costs [4], and environmental pollution [17].

In addition to the above contributions, other research efforts have focused on addressing demand-side variations, incorporating the multi-objective nature of the problem, and employing stochastic or robust optimization approaches [4, 10, 18]. Furthermore, the interaction between transit systems and other modes of transportation has emerged as another critical area of research [19]. Despite all these efforts, research in these areas remains ongoing, as the complexity and scope of route design pose a broad spectrum of problems for further exploration. For a more comprehensive review of the literature, the interested reader may consult recent review papers and the references cited therein [10, 20, 21].

Among other aspects of the transit routes network design problem, an interesting yet relatively underexplored area is the examination of characteristics associated with specific network structures, such as grid networks, and the implications of these characteristics for designing route configurations. Grid-structured networks are exemplified today by many modern cities such as Kyoto, Beijing, and many North American cities. Transit networks employing a grid structure, with routes oriented predominantly in east-west or north-south directions, offer several attributes that render them attractive to the research community of urban planning. These attributes include their structural simplicity and operational clarity, predictable scheduling and optimized transfer systems, ease of planning and maintenance, and cost-effectiveness—particularly when mass transit systems are involved [22]. Based on these features, few studies have incorporated assumptions such as fixed spacing between lines or uniform/centripetal demand profiles to derive theoretical models and analyses over such networks [22-24]. Though certain aspects of the problem, e.g., the effect of candidate routes orientations over the results obtained for route configurations, remain inadequately studied, highlighting the need for further research.

One critical question in the design of an affordable routes system in a grid network corresponds to the definition of the pool of candidate routes. Due to the aforementioned attributes of grid networks, in urban planning, there is a tendency to define candidate routes along east-west (horizontal) or north-south (vertical) orientations. Referred to as "restricted candidate routes," these predefined orientations prompt the inquiry of how much relaxing this constraint—i.e., incorporating routes that are not necessarily horizontal or vertical, namely "unrestricted" candidate routes—may enhance the quality of the final routes configuration. To investigate this question, this study examines two scenarios: one employing unrestricted candidate routes and the other employing restricted candidate routes. The results are reported in terms of network coverage over a 60 (6×10) node grid network. Our findings suggest that, interestingly, the scenario of restricted candidate routes can achieve solutions with 98% of the quality attained by unrestricted candidate routes.

The remainder of this paper is structured as follows: A general description of the problem is presented in Section 2. The two scenarios of candidate routes and corresponding solution algorithms are introduced in Section 3. The results are presented and discussed in Section 4, followed by concluding remarks in Section 5.

2. Description of the problem

The process of designing transit route networks is traditionally approached in two sequential phases: (1) route generation, which involves creating a pool of candidate transit routes, and (2) route selection, which focuses on identifying an optimal subset of routes from the generated pool. Defining the pool of candidate routes, in the first stage of design, has a large impact on the resulting network [3, 5]. This impact, however, in grid-structured networks, has not been addressed much in the literature. To further explore this effect over grid transportation networks, this section starts by introducing a general formulation of the routes design problem. First, we introduce the concept of network coverage, which is later applied as the study's objective function.

2.1. The concept of network coverage

One of the commonly applied objective functions at the strategic level of urban planning and decision-making is network coverage [15, 18]. In a general perspective, coverage refers to the proportion of network users that are potentially served by the configuration of transit routes in the network. To calculate this measure, it is important to consider that factors such as route transfers within the network and extended travel times associated with transit services can significantly reduce the share of transit in competition with other modes of transportation, such as private cars. Research has interestingly shown that travelers may even opt for longer routes to avoid frequent transfers [24]. To address these behaviors, this study applies a penalty of 5 additional minutes of travel time for each route transfer. Furthermore, while direct transit trips are considered to provide 100% coverage, coefficients of

70% and 50% are assigned to trips involving one and two transfers, respectively. Finally, a coefficient based on travel-time values is adopted to incorporate additional travel times imposed by transit service as compared to private vehicles.

The process for calculating coverage, as influenced by the above penalties, is illustrated in Fig. 1. In this figure:

C: the set of all acceptable candidate transit routes,

S: the set of selected candidate transit routes to be added to the network,

$Cov(S)$: the amount of network coverage (in passenger units) after adopting S as a subset of candidate transit routes, $S \subseteq C$,

$N(S)$: the underlying transportation network by adopting S as the set of transit routes, $S \subseteq C$,

$demand(o, d)$: the amount of transit travel-demand from o to d, $(o, d) \in OD$,

OD: the set of all origin-destinations in the network,

$P(o, d, N(S))$: the shortest transit path from o to d, by considering transfer penalties in $N(S)$, $(o, d) \in OD$, $S \subseteq C$,

$Tr(o, d, N(S))$: the shortest transit travel-time from o to d, by considering transfer penalties in $N(S)$, $(o,d) \in OD$, $S \subseteq C$,

$Au(o, d)$: the shortest auto travel-time from o to d,

$n(o, d, N(S))$: the number of line-transfers in the path $P(o, d, N(S))$, $(o, d) \in OD$, $S \subseteq C$.

```
$Cov(S) = 0$ ;
For each $(o,d) \in OD$
    Calculate $P(o,d,N(S))$, $\mathrm{Tr}(o,d,N(S))$, $n(o,d,N(S))$ and $\mathrm{Au}(o,d)$ ;
    if $n(o,d) = 0$
        $Cov(S) = Cov(S) + 1.0\times \mathrm{Au}(o,d)/\mathrm{Tr}(o,d,N(S))\times demand(o,d)$ ;
    else if $n(o,d) = 1$
        $Cov(S) = Cov(S) + 0.7\times \mathrm{Au}(o,d)/\mathrm{Tr}(o,d,N(S))\times demand(o,d)$;
    else if $n(o,d) = 2$
        $Cov(S) = Cov(S) + 0.5\times \mathrm{Au}(o,d)/\mathrm{Tr}(o,d,N(S))\times demand(o,d)$ ;
```

Fig. 1. The process of calculating network coverage.

As can be observed in Fig. 2, the initial value of Cov(S) is set to zero. Subsequently, through iterations for each origin-destination (O-D) pair, such as (o, d), the auto shortest path, transit shortest path, and the number of transfers involved are determined. The travel demand associated with the O-D pair is then added to the cumulative value of Cov(S).

Fig. 2 illustrates the use of coefficients 1.0, 0.7, and 0.5 to account for the inconvenience caused by line transfers for travelers, reducing the value of covered demand accordingly. Additionally, travel-time penalties for transit users are addressed by employing a coefficient represented as Au(o, d)/Tr(o, d, N(S)).

At the end of the iterative process in Fig. 2, Cov(S) is calculated in terms of passenger units over the network. Note that the value of coverage can also be expressed in terms of the percentage of the total travel demand, simply by calculating the ratio of the “covered” passengers to the total travel demand.

2.2. Problem formulation

We assume that the travel demand between origin-destination (O-D) pairs remains constant throughout the analysis period. To provide a generalized formulation of the problem, let us define:

L: an upper bound for the maximum length of all selected transit routes (previously defined) with regard to the budget constraint

K: the total number of candidate routes in the set C

l_k: the length of the k^{th} candidate route, $1 \le k \le K$

$b_k(S)$: a binary variable which is 1 if the k^{th} candidate route is a member of set S, and 0 otherwise, $1 \le k \le K$.

$$\max \quad Cov(S) \tag{1}$$

$$\text{s.t.} \quad S \subseteq C \tag{2}$$

$$\sum_{k=1}^{K} b_k(S)\, l_k \le L \tag{3}$$

In the above formulation, the objective function (1) intends to maximize the network's coverage by identifying an optimal subset of candidate routes, referred to as S. Meanwhile, constraint (2) states that the routes have to be selected from an “acceptable” pool of candidate routes. This acceptable pool will be further discussed later on in the next section. Constraint (3) also imposes a limit on the total length of selected transit routes, which must not exceed a specified value, L. This value is set based on the available budget for planning. It can be easily demonstrated that this formulation falls within the NP-hard category of problems and cannot be tackled by exact solution algorithms on a large scale.

3. Two scenarios for solving the problem

Given the problem definition in section 2.2, it is obvious that the set of candidate routes C, i.e., potential routes to select from, can affect the search space and therefore the quality of the routes configuration. In a general sense and from an operations research point of view, the larger the search space of C, the higher the quality of solutions to the problem. Nevertheless, when grid-structured transportation networks are involved, many urban planning authorities tend to restrict the candidate routes to horizontal (east-west) or vertical (north-south) routes and benefit from their orderly and reliable service. The pivotal question arising here is, to what extent can this restriction of candidate routes contribute to the reduction of network coverage?

To answer this question, we consider two scenarios in this study: scenario 1, in which candidate routes do not necessarily need to be horizontal or vertical, and scenario 2, in which candidate routes are restricted to horizontal or vertical routes. Fig. 2 provides a schematic overview of these two scenarios.

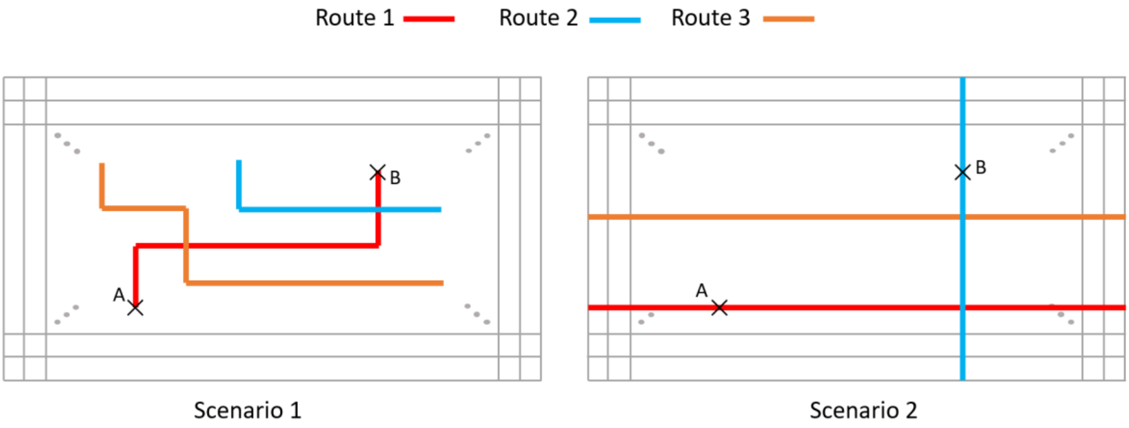

Fig. 2. Schematic overview of two scenarios for candidate transit routes.

To solve the problem in scenario 1, considering the intractable scale of the search space, a heuristic algorithm is introduced and applied in this study. Also, for scenario 2, an exact solution based on enumeration is exploited.

3.1. Scenario 1: Unrestricted candidate routes

In this scenario, the search space of the problem is extremely large even for medium-sized examples. As a result, a heuristic algorithm is presented in this section, which can be categorized as a constructive algorithm. The algorithm builds upon the idea of connecting the most promising nodes of the network using transit routes configuration. Prior to algorithm presentation, let us define V as the set of network nodes and d_{IJ} as the amount of travel demand from node I to node J, I and $J \in V$. Based on these definitions, a measure of a node’s importance, namely Level of Activity (LoA), is adopted for nodes of the network, as follows:

$$\mathrm{LoA}(N) = \sum_{I \in \mathrm{V}} d_{IN} + \sum_{J \in \mathrm{V}} d_{NJ} \qquad N \in V \tag{4}$$

According to (4), LoA(N) is the total amount of transit travelers ingoing to and outgoing from node N, $N \in V$. It is obvious that nodes with higher values of LoA(N), while included in the transit routes configuration, are more likely to increase the overall coverage in the network. To present the solution algorithm, let us further define:

S: Set of selected candidate routes to be added to the network,

$l(A, B)$: the length of the transit route between nodes A and B, and

l_{min}, l_{max}: standard values for minimum and maximum lengths for a transit route, respectively.

Based on the above definitions, Fig. 3 presents the proposed algorithm to solve the problem in scenario 1.

The algorithm in Fig. 3 starts by initialization and reading input data (steps 0 and 1). Prior to starting iterations (steps 3 to 6), the algorithm calculates the level of importance (namely LoA measure) for all nodes of the network (step 2). In the course of its iterations, in a greedy fashion, the algorithm picks up the two nodes A and B (e.g. the nodes depicted in Fig. 2) with maximum LoA from the set of nodes V (steps 3 and 4) and tries to connect them by introducing a direct shortest-path route to the set of transit routes (steps 5 and 6). The iterations will proceed until the algorithm fails to add more candidate routes within the available budget (step 6).

3.2. Scenario 2: Restricted (horizontal/vertical) candidate routes

In this scenario, the selection among candidate routes is restricted to only horizontal (east-west) and vertical (north-south) routes in the network. For example, for a grid network of n×m size, the number of candidate routes is limited to (n + m) routes, consisting of n horizontal and m vertical routes. Given the search space, which is now much smaller than that of scenario 1, problems of small-to-medium scale can now be solved using exact solution algorithms or even enumeration methods.

Let us define a dominant solution as a selection of candidate routes to which no further candidate route can be added while holding the budget constraint. Based on the definition of coverage in this study, the global optimal (i.e., exact) solution of the problem in scenario 2 can be found within the search space of dominant solutions. It is not difficult to prove this lemma in the sense that the addition of new candidate routes to a grid network will not lead to a decline in the value of coverage (as defined earlier in Fig. 3).

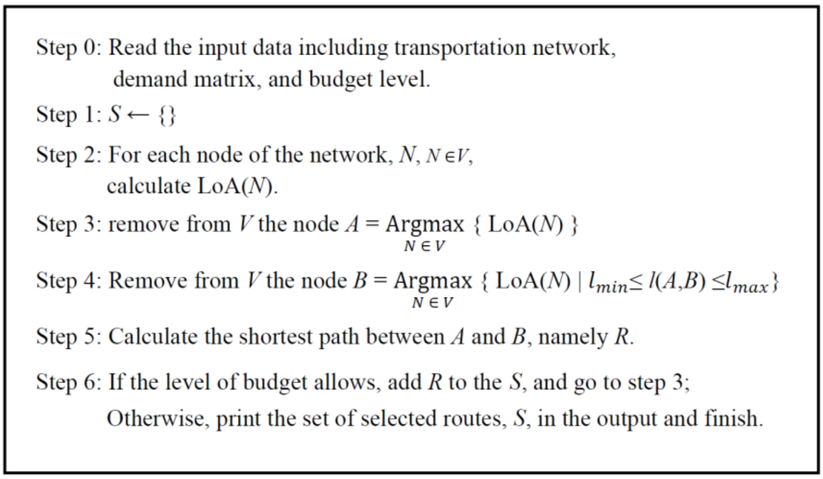

```
Step 0: Read the input data including transportation network,
        demand matrix, and budget level.
Step 1: $S \leftarrow \{\}$
Step 2: For each node of the network, $N$, $N \in V$,
        calculate LoA($N$).
Step 3: remove from $V$ the node $A = \underset{N \in V}{\mathrm{Argmax}} \{ \mathrm{LoA}(N) \}$
Step 4: Remove from $V$ the node $B = \underset{N \in V}{\mathrm{Argmax}} \{ \mathrm{LoA}(N) \mid l_{min} \leq l(A,B) \leq l_{max} \}$
Step 5: Calculate the shortest path between $A$ and $B$, namely $R$.
Step 6: If the level of budget allows, add $R$ to the $S$, and go to step 3;
        Otherwise, print the set of selected routes, $S$, in the output and finish.
```

Fig. 3. Heuristic algorithm to solve the problem in scenario 1.

Therefore, to solve the problem in scenario 2, one can simply perform an enumeration over dominant solutions of the problem and achieve the best solution obtained as the global optimal solution.

4. Results

To evaluate the results derived from the two introduced scenarios, the algorithms presented in the previous section are implemented using the Python programming language. A medium-sized grid network consisting of 60 (6×10) nodes is considered to run the programs. A general representation of this network is depicted in Fig. 4, where it is assumed that each block has a length and width of 2.2 km and 2 km, respectively, and the maximum length of public transit routes due to the budget constraint (i.e. the value for L in (3) in problem formulation) is constrained to 100 km. Additionally, it is assumed that travel demand values follow a uniform random distribution, and to report the results, 30 independent demand matrices are taken into consideration. Table 1 illustrates the coverage values obtained for each of the two scenarios.

According to the results in Table 1, after running the programs on 30 random demand matrices, the average coverage values obtained for scenarios 1 and 2 are 14.2% and 13.9%, respectively. These findings suggest that, despite restricting public transit lines to horizontal and vertical routes, it is still possible to achieve results with an average quality of 98% (i.e., 100 × 13.9/14.2%) compared to the unrestricted transit routes scenario.

The relatively small 2% difference between the two defined scenarios can be significant from an urban planning perspective. As mentioned in Section 1, numerous criteria other than coverage are involved in the urban design of cities. These criteria may justify such a reduction in coverage when adopting multi-objective planning approaches. As an example of the results obtained for both scenarios, Fig. 5 illustrates the route configurations for demand matrix 6 in Table 1. In this figure, (a) and (b) correspond to scenarios 1 and 2, respectively, where the coverage values of 14.22% and 13.89% are achieved.

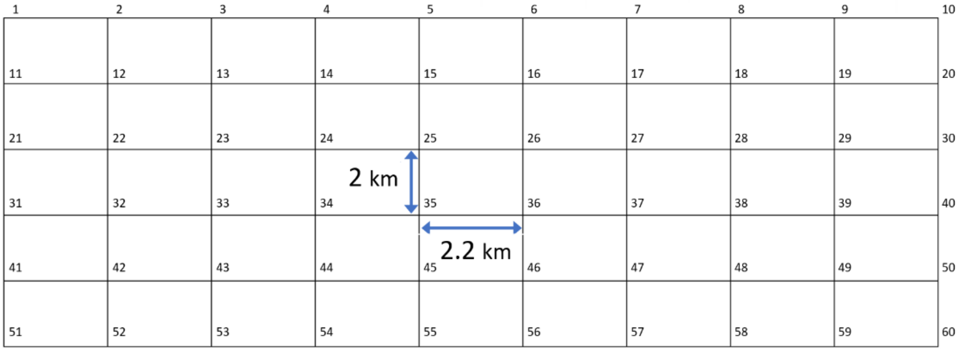

Fig. 4. 6×10 grid network used in this study.

5. Concluding remarks

In this paper, the problem of transit routes configuration for grid networks was studied for the structure of its candidate routes. The paper aimed to answer this question: To what extent does restricting the search space of candidate routes to horizontal or vertical routes reduce the quality of the results in terms of network coverage?

Table 1. Results obtained for scenarios 1 and 2 over 30 random demand matrices.

Demand Matrix	Coverage (%)		Demand Matrix	Coverage (%)	
	Scenario 1	Scenario 2		Scenario 1	Scenario 2
1	11.9	13.5	16	16.3	13.8
2	14.8	13.6	17	9.5	13.9
3	15.7	13.6	18	13.2	13.5
4	18.3	13.7	19	11.7	13.9
5	15.2	14.0	20	13.1	13.8
6	14.2	13.9	21	12.3	13.9
7	13.8	13.7	22	17.0	13.6
8	15.9	13.9	23	12.7	13.7
9	16.5	13.9	24	11.0	13.5
10	15.7	13.5	25	15.3	13.9
11	14.6	13.8	26	16.5	13.7
12	15.4	13.7	27	10.6	13.8
13	17.2	13.9	28	16.6	13.9
14	11.4	13.9	29	12.9	13.5
15	11.8	14.0	30	13.6	16.7

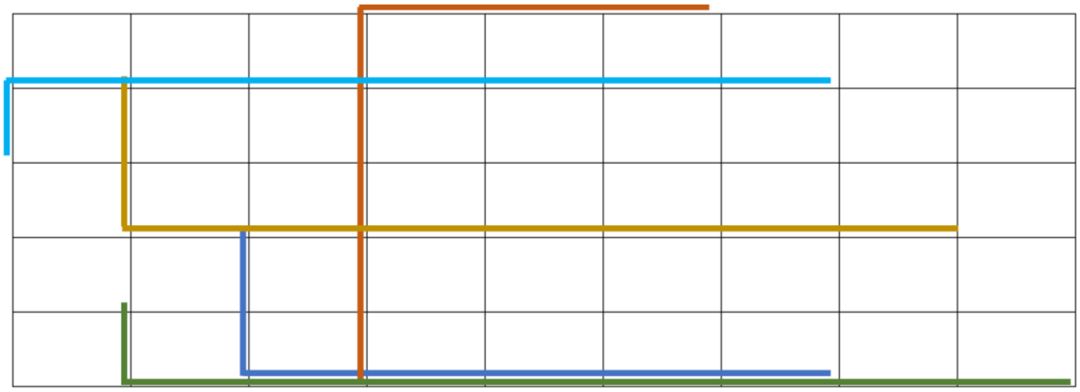

(a) Scenario 1

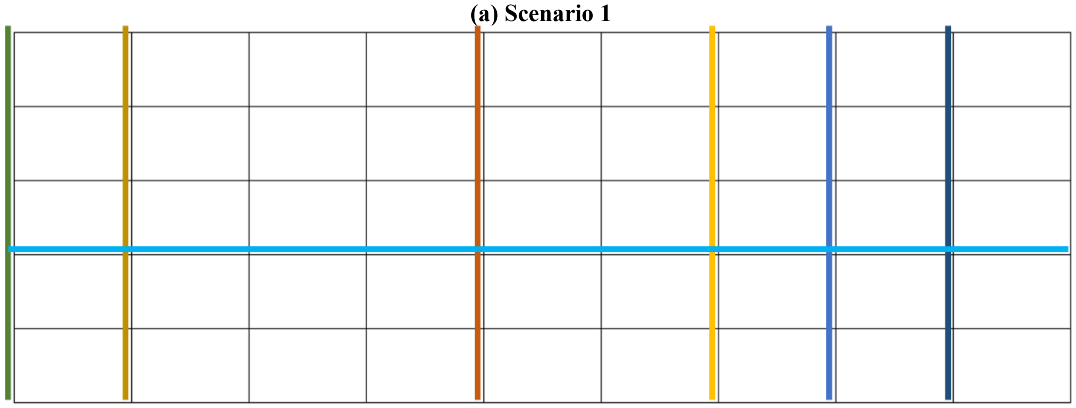

(b) Scenario 2

Fig. 5. Results obtained for demand matrix 6.

Two scenarios were taken into account: (1) unrestricted candidate routes, in which there is no constraint for the shape of candidate routes, and (2) restricted (horizontal/vertical) candidate routes, in which only horizontal (east-west) or vertical (south-north) candidate routes can be selected. To examine the results, a medium-sized grid network of 60 nodes (6×10) was taken into account, and two algorithms corresponding to the scenarios were applied.

In the first scenario, a constructive algorithm was introduced that finds the most promising nodes of the network in terms of travel demand and tries to interconnect these nodes through route selection. In the second scenario, however, the search space is notably smaller and therefore an exact enumeration algorithm was applied to extract the global optimal solutions of the problem. The comparison between the two scenarios over 30 random travel demand matrices, interestingly, suggested that scenario 2 can lead to solutions with 98% coverage as compared to scenario 1. In other words, restricting the search space of candidate routes to horizontal/vertical routes, in this study, leads to only a 2% decline in the quality of the solutions.

To expand the findings of this study, several directions can be taken into account in future research. For example, more sophisticated and advanced algorithms for comparison can be investigated. Additionally, larger networks with other configurations can be considered for comparison between the two scenarios. Finally, exploring other travel demand patterns, e.g., centripetal demand matrices with single or multiple demand centers, can be an interesting topic for future research.

Statements & Declarations

Author contributions

Amirali Zarrinmehr: Conceptualization, Methodology, Supervision, Writing - Original Draft.

Mohammad Mehdi Ghasemi: Investigation, Visualization, Validation, Resources, Formal analysis.

Funding

The authors received no financial support for the research, authorship, and/or publication of this article.

Data availability

The data presented in this study will be available on interested request from the corresponding author.

Declarations

The authors declare no conflict of interes.

References

[1] Shah, K. J., Pan, S.-Y., Lee, I., Kim, H., You, Z., Zheng, J.-M., Chiang, P.-C. Green transportation for sustainability: Review of current barriers, strategies, and innovative technologies. Journal of Cleaner Production, 2021; 326: 129392. doi:10.1016/j.jclepro.2021.129392.

[2] Ceder, A. Urban mobility and public transport: future perspectives and review. International Journal of Urban Sciences, 2021; 25: 455-479. doi:10.1080/12265934.2020.1799846.

[3] Guihaire, V., Hao, J.-K. Transit network design and scheduling: A global review. Transportation Research Part A: Policy and Practice, 2008; 42: 1251-1273. doi:10.1016/j.tra.2008.03.011.

[4] Zarrinmehr, A., Saffarzadeh, M., Seyedabrishami, S., Nie, Y. M. A path-based greedy algorithm for multi-objective transit routes design with elastic demand. Public Transport, 2016; 8: 261-293. doi:10.1007/s12469-016-0131-1.

[5] Gattermann, P., Harbering, J., Schöbel, A. Line pool generation. Public Transport, 2017; 9: 7-32. doi:10.1007/s12469-016-0127-x.

[6] Mejri, I., Layeb, S. B., Zeghal, F. A survey on network design problems: main variants and resolution approaches. European Journal of Industrial Engineering, 2023; 17: 253-309. doi:10.1504/EJIE.2023.129443.

[7] Salhi, S., Thompson, J. An Overview of Heuristics and Metaheuristics. In: S. Salhi, J. Boylan editors. The Palgrave Handbook of Operations Research. Berlin (DE): Springer International Publishing; 2022. p. 353-403. doi:10.1007/978-3-030-96935-6_11.

[8] M. Almufti, S., Ahmad Shaban, A., Arif Ali, Z., Ismael Ali, R., A. Dela Fuente, J. Overview of Metaheuristic Algorithms. Polaris Global Journal of Scholarly Research and Trends, 2023; 2: 10-32. doi:10.58429/pgjsrt.v2n2a144.

[9] Durán-Micco, J., Vansteenwegen, P. A survey on the transit network design and frequency setting problem. Public Transport, 2022; 14: 155-190. doi:10.1007/s12469-021-00284-y.

[10] Nnene, O. A., Zuidgeest, M. H. P., Joubert, J. W. BRT network design for transit cost reduction in Cape Town, South Africa. Journal of Public Transportation, 2023; 25: 100042. doi:10.1016/j.jpubtr.2023.100042.

[11] Wei, Y., Jiang, N., Li, Z., Zheng, D., Chen, M., Zhang, M. An Improved Ant Colony Algorithm for Urban Bus Network Optimization Based on Existing Bus Routes. ISPRS International Journal of Geo-Information, 2022; 11: doi:10.3390/ijgi11050317.

[12] Oudani, M. A Simulated Annealing Algorithm for Intermodal Transportation on Incomplete Networks. Applied Sciences, 2021; 11: doi:10.3390/app11104467.

[13] Zarrinmehr, A., Saffarzadeh, M., Seyedabrishami, S. A local search algorithm for finding optimal transit routes configuration with elastic demand. International Transactions in Operational Research, 2018; 25: 1491-1514. doi:10.1111/itor.12359.

[14] Zarrinmehr, A., Moloukzade, H. Application of a Hill-Climbing Algorithm to Public Transportation Routes Design in Grid Networks. International Journal of Transportation Engineering, 2021; 9: 597-612. doi:10.22119/ijte.2021.285454.1569.

[15] Wan, T., Lu, W., Sun, P. Equity impacts of the built environment in urban rail transit station areas from a transit-oriented development perspective: a systematic review. Environmental Research Communications, 2023; 5: 092001. doi:10.1088/2515-7620/acf8b2.

[16] Piracha, A., Chaudhary, M. T. Urban Air Pollution, Urban Heat Island and Human Health: A Review of the Literature. Sustainability, 2022; 14: doi:10.3390/su14159234.

[17] Wang, L., Jin, J. G., Sibul, G., Wei, Y. Designing Metro Network Expansion: Deterministic and Robust Optimization Models. Networks and Spatial Economics, 2023; 23: 317-347. doi:10.1007/s11067-022-09584-7.

[18] Zhang, L., Wen, H., Lu, J., Lei, D., Li, S., Ukkusuri, S. V. Exploring cascading reliability of multi-modal public transit network based on complex networks. Reliability Engineering & System Safety, 2022; 221: 108367. doi:10.1016/j.ress.2022.108367.

[19] Mauttone, A., Cancela, H., Urquhart, M. E. Network Design with Applications to Transportation and Logistics. 1st ed. Berlin (DE): Springer International Publishing; 2021. doi:10.1007/978-3-030-64018-7.

[20] Abdallah, T. Sustainable Mass Transit: Challenges and Opportunities in Urban Public Transportation. 2nd ed. Amsterdam (NL): Elsevier; 2023. doi:10.1016/B978-0-443-15271-9.00006-6.

[21] Xie, F., Levinson, D. Topological evolution of surface transportation networks. Computers, Environment and Urban Systems, 2009; 33: 211-223. doi:10.1016/j.compenvurbsys.2008.09.009.

[22] Miyagawa, M. Spacing of intersections in hierarchical road networks. Journal of the Operations Research Society of Japan, 2018; 61: 272-280. doi:10.15807/jorsj.61.272.

[23] Daganzo, C. F. Structure of competitive transit networks. Transportation Research Part B: Methodological, 2010; 44: 434-446. doi:10.1016/j.trb.2009.11.001.

[24] Stern, R. Passenger Transfer System Review. 1st ed. Washington D.C. (DC): National Academy Press; 1996.

Civil Engineering and Applied Solutions, 2025; 1(3): 70–79

Civil Engineering and Applied Solutions

Research Article

journal homepage: ceas.journals.umz.ac.ir

CEAS Civil Engineering and Applied Solutions

2D vs 3D Finite Element Analysis of Free Span Response in Subsea Pipelines

Meisam Qorbani Fouladi [a], Hamed Shirazi [a], Maryam Taghizadeh [a*], Giacomo Viccione [b]

[a] *Department of Civil Engineering, University of Science and technology of Mazandaran, Behshahr, Iran*
[b] *Department of Geology, Faculty of Science, University of SALERNO, Fisciano, Italy*

A R T I C L E I N F O

Keywords:
Subsea pipelines
Free span
2D vs 3D modeling
Finite Element Method

Article history:
Received 01 July 2025
Accepted 21 July 2025
Available online 01 August 2025

A B S T R A C T

Free-span formation in subsea pipelines, often caused by seabed irregularities, local scour, or differential settlements, poses a significant threat to pipeline integrity through the induction of vortex-induced vibrations (VIV), fatigue damage, and potential structural failure. While two-dimensional (2D) numerical models are widely used in early-stage designs due to their simplicity and computational efficiency, their ability to accurately predict the complex dynamic behavior of pipelines remains limited. In contrast, three-dimensional (3D) models provide a more realistic representation of seabed geometry, pipe-soil interaction, and hydrodynamic loading, albeit at the expense of greater computational resources. This study presents a comparative numerical analysis of subsea pipelines with free spans under both 2D and 3D finite element models using ABAQUS software. Key parameters, including deformed shapes, natural frequencies, and simulation run-times, are extracted and evaluated. The results offer valuable insight into the accuracy and applicability of simplified 2D models for preliminary design purposes, providing engineers with a practical framework for selecting appropriate modeling strategies based on project constraints and performance requirements. The study also lays the groundwork for aligning simplified numerical analyses with international design standards.

1. Introduction

A submarine pipeline is a vital component of the hydrocarbon resources from offshore fields to onshore facilities in a safe manner. There is a high level of complexity in the environmental conditions surrounding these structures. It is important to note that these conditions have a significant influence on pipeline performance and safety. As far as the environmental conditions are concerned, free spans play a substantial role in the design and operation of these pipelines. A free span affects pipeline support conditions and can lead to vortex-induced vibrations (VIV), leading to structural fatigue and reduced service life. To ensure safety and optimize design, it is therefore imperative to understand the mechanical and dynamic behavior of pipelines in the presence of free spans [1-4].

In the early stages of subsea pipeline design, structural analyses under free-span conditions were mainly based on simplified theoretical models, such as the Euler-Bernoulli beam theory, where the pipeline was assumed to act as a rigid beam resting on a rigid seabed with linear dynamic behavior [5]. While useful for preliminary assessments, these approaches lacked the capability to accurately capture the interaction between the seabed, hydrodynamic loading, and the pipeline's dynamic response. Subsequently, experimental and field-based approaches gained traction for studying the real behavior of free-spanning pipelines. Experimental studies in flow channels and water tunnels enabled direct investigation of phenomena such as VIV, hydrodynamic pressure distribution, and structural response [6]. In addition, field data obtained from in-situ monitoring systems installed on operational pipelines provided valuable insights into real-world performance [7]. Nevertheless, inherent limitations such as high costs, limited scalability, and difficulty in controlling environmental parameters restricted the broad applicability of experimental methods in

---

* Corresponding author.
E-mail addresses: taghizadeh@mazust.ac.ir (M. Taghizadeh).

https://doi.org/10.22080/ceas.2025.29587.1021
ISSN: 3092-7749/© 2025 The Author(s). Published by University of Mazandaran.
This article is an open access article distributed under the terms and conditions of the Creative Commons Attribution (CC-BY) license (https://creativecommons.org/licenses/by/4.0/deed.en)
How to cite this article: Qorbani Fouladi, M., Shirazi, H., Taghizadeh, M., Viccione, G. 2D vs 3D Finite Element Analysis of Free Span Response in Subsea Pipelines. Civil Engineering and Applied Solutions. 2025; 1(3): 70–79. doi:10.22080/ceas.2025.29587.1021.

practical design processes.

With the development of numerical methods and increased computational capacity, the finite element method (FEM) has become a standard tool in subsea pipeline design. Many early studies adopted two-dimensional modeling as a practical compromise to reduce computational cost and complexity [8]. In this approach, the pipeline is typically modeled as a cross-sectional element and analyzed under hydrodynamic loading, self-weight, and interaction with the seabed in a two-dimensional plane [9].This method enables faster simulations and supports extensive parametric studies, making it common in early design phases or projects constrained by time and resources [10]. However, 2D models exhibit inherent limitations that may result in inaccurate predictions of actual pipeline behavior. For example, they cannot accurately evaluate vibration frequency, structural displacements, or complex nonlinear interactions between the pipeline and seabed. Therefore, evaluating the accuracy and applicability of 2D models, particularly through comparison with 3D simulations, remains a critical issue in simulation-based design.

With advancements in computational tools and numerical software, three-dimensional modeling of free-spanning subsea pipelines has gained widespread attention among researchers and engineers. 3D analyses allow for a more realistic representation of complex effects such as three-directional seabed irregularities and nonlinear pipeline–seabed interaction [11]. In scenarios involving hydrodynamic phenomena, 3D modeling for obtaining reliable results is not just important, but vital. Many recent studies have employed software platforms such as ABAQUS, ANSYS, and OrcaFlex to capture nonlinear behavior, dynamic loading, and pipe seabed flow interactions. Although these models require greater computational effort, they offer superior accuracy in predicting dynamic responses, especially in VIV-related fatigue and progressive failure analyses. Consequently, 3D simulations not only provide deeper insights into pipeline behavior but also serve as reference standards for validating simplified 2D models.

Despite significant progress in both 2D and 3D numerical modeling of free-spanning pipelines, challenges remain in assessing the accuracy of simplified models and their consistency with real-world conditions. In many engineering projects, the use of 2D models is inevitable due to resource or time constraints; however, their validity, particularly in predicting vibration, deformation, and dynamic responses, must be critically evaluated through comparison with 3D models. The present study aims to simulate and compare the behavior of subsea pipelines under two-dimensional and three-dimensional conditions. A validated numerical model based on the finite element method (FEM) is employed to conduct the analysis. The dynamic response of the pipeline is examined under uniform loading, with particular emphasis on the influence of a soft seabed on its structural behavior. The analysis primarily focuses on critical parameters such as the deformed shape of the pipeline, natural frequencies, and the total computation time required for the simulations. These parameters are essential for understanding the dynamic behavior and stability of subsea pipelines. Comparing them in 2D and 3D models helps assess the accuracy and reliability of each modeling approach. By emphasizing this comparison, the study seeks to identify the strengths and limitations of 2D models and assess their applicability in preliminary design scenarios. The outcomes of this study can offer practical guidance for design engineers by clarifying the capabilities and limitations of 2D analysis, supporting more informed decisions in selecting the appropriate level of modeling fidelity. Furthermore, this research contributes to efforts toward standardizing the use of simplified models in compliance with international design codes and guidelines.

2. Governing equation

Beam theory is commonly used to model free-spanning subsea pipeline structural behavior. The Euler-Bernoulli beam theory is considered an appropriate approach for estimating flexural deformation according to DNV-RP-F105 [12], particularly when the span length is large relative to the pipeline diameter. The theory ignores shear deformation and assumes that the cross-section remains as a plane perpendicular to the neutral axis after deformation. The flexural response of the beam subjected to distributed loading is formulated in Eq. 1:

$$EI\frac{d^4w(x)}{dx^4} = q(x) \tag{1}$$

where E is the Young's modulus, I is the second moment of area, $w(x)$ is the vertical deflection of the beam at position x, and $q(x)$ is the distributed load along the beam.

2.1. Two-dimensional (2D) formulation

In the 2D case, deformation is restricted to a single plane, typically involving bending about a primary axis [13]. The internal response can be characterized by the shear force $V(x)$ and bending moment $M(x)$, which are related to deflection as follows:

$$V(x) = \frac{d^3}{dx^3}\,(EI\,(x)) \tag{2}$$

$$M\,(x) = \frac{d^2}{dx^2}\,(EI\,(x)) \tag{3}$$

2.2. Three-dimensional (3D) formulation

In three-dimensional analysis, the pipeline may undergo bending about two orthogonal principal axes, and, where necessary, torsional deformation can also be considered [14]. The governing equations for flexural deformation in the y- and z-directions are as follows [15]:

$$q_y(x) = \frac{d^4 w_y(x)}{dx^4} EI_y \tag{4}$$

$$q_z(x) = \frac{d^4 w_y(x)}{dx^4} EI_y \tag{5}$$

where I_y and I_z are the second moments of area about the respective principal axes, $W_y(x)$ and $W_z(x)$ represent transverse displacements in two perpendicular directions, and $q_y(x)$ and $q_z(x)$ are the distributed loads acting in the respective directions.

3. Two-dimensional and three-dimensional simulation setup

To simulate the free-span phenomenon, a section of the pipeline path is assumed to contain loose soil. Consequently, settlements may occur due to hydrostatic pressure and the weight of both the pipeline and the supporting mattress. The simulations are performed without considering the influence of soil deformation on the settlement values. Given that the solution domain has relatively low geometric complexity and axial symmetry, computational cost can be reduced by applying static symmetry. Therefore, only half of the domain is modeled instead of the full geometry.

In both 2D and 3D models, wire elements are employed to simulate the pipeline behavior due to their simplicity and lower computational cost. Although solid elements could provide a more detailed structural representation, their use would substantially increase computational demands and add complexity to the modeling process. It is important to note that, since this study does not focus on phenomena related to the pipeline wall thickness, the use of solid elements is not considered necessary. Furthermore, while the 2D model employs shell elements for the pipeline structure, the 3D model uses solid elements for other structural components.

3.1. Model geometry

In the modeling process, span lengths of 2, 4, 6, 8, and 10 meters were considered. For an accurate simulation of the pipeline behavior in the free-span region, a relatively long pipeline segment resting on firm soil was included in the model, with an actual total length of 280 meters. To reduce computational time, only half of the geometry was modeled by exploiting static symmetry conditions. As shown in Fig. 1, all other geometrical characteristics of the model are illustrated.

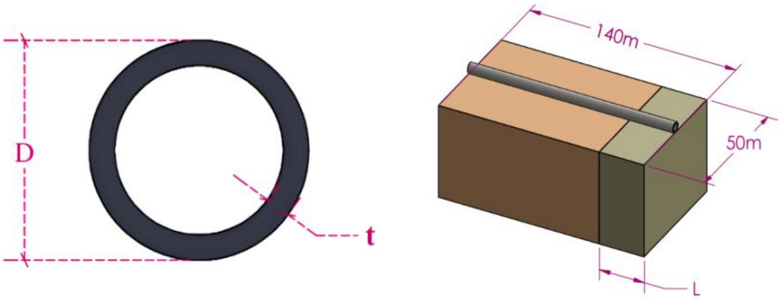

Fig. 1. The entire model and pipe section parameters.

In this study, three different pipeline configurations have been employed. The geometric specifications corresponding to each scenario are summarized in Table 1.

Table 1. Geometry properties.

No.1		No.2		No.3	
***t*(m)**	***D*(m)**	***t*(m)**	***D*(m)**	***t*(m)**	***D*(m)**
0.02	1	0.035	1	0.035	2

3.2. Material

The materials used in this study are classified into three main groups. The first group relates to the mechanical properties of steel pipelines and includes both elastic and plastic characteristics. To model the nonlinear plastic behavior of steel, a bilinear stress-strain model has been employed, with its parameters presented in Table 2. For the plasticity modeling of steel, an isotropic hardening law is used, and the Von Mises yield criterion governs the onset of yielding. The second and third groups relate to the geotechnical properties of the subsoil. The second group represents zones with high settlement potential, modeled using soils with low stiffness. In contrast, the third group corresponds to areas with adequate stiffness and higher resistance, where significant settlement is not expected. To define the plastic behavior of the soil materials, the Mohr-Coulomb failure criterion has been applied. The parameters used in this model are provided in Table 3.

Table 2. Mechanical properties of pipe.

Apparent density (kg/m^2)	**5000**	
Elastic	**Young's modulus (GPa)**	**Poisson's ratio**
	210	0.3
Plastic	**Young's modulus (GPa)**	**Poisson's ratio**
	455	0.3

Table 3. Mechanical properties of soils.

Apparent density (kg/m^2)	**Stiff soil**		**Soft soil**	
Elastic	**Young's modulus (MPa)**	**Poisson's ratio**	**Young's modulus (MPa)**	**Poisson's ratio**
	100	0.25	1	0.25
Moher coulomb plasticity	**Friction angle**	**Dilation angle**	**Friction angle**	**Dilation angle**
	35	15	25	8

3.3. Load and boundary conditions

To define the boundary conditions in the Abaqus model and in accordance with the requirements of geometric and loading symmetry, a Cartesian coordinate system is adopted. In this system, the *xx*-axis is aligned with the longitudinal direction of the pipeline, the *yy*-axis is defined as vertical and perpendicular to the *xx*-axis, and the *zz*-axis is horizontal and orthogonal to both *xx* and *yy* axes. Based on this coordinate system, roller supports are assigned at both ends of the pipeline along the *yy*-axis, allowing vertical displacement while constraining motion in all other directions. The interaction between the pipeline and the surrounding soil is modeled using a surface-to-surface contact definition. In this contact formulation, frictional forces are considered in both the normal and tangential directions. In the tangential direction, the coefficient of friction between the pipe and the soil is assumed to be 0.2, following the recommendations of the DNV-ST-F101 [16] standard for soft soils. This standard suggests a typical friction coefficient in the range of 0.2 to 0.3 under such conditions. A Hard Contact condition is applied in the normal direction to prevent unrealistic penetration between the pipe and the soil, thereby ensuring a more accurate simulation of their physical interaction. This contact formulation allows for proper transfer of normal forces and effectively eliminates numerical interpenetration between the contacting surfaces.

To accurately represent the plane strain conditions inherent to the actual problem, additional constraints have been applied in the three-dimensional analysis to eliminate any out-of-plane deformations. Within the scope of this study, the following loads are considered:

- Internal pressure applied to the inner wall of the pipe, resulting from the fluid flow within it;
- The external pressure is the hydrostatic pressure created by the pipe's location 50 meters below sea level;
- The weight of the pipeline, applied in the model using gravitational acceleration;
- The weight of the mattress, modeled as a line load.

It is noteworthy that the internal pressure, external pressure, and self-weight of the pipelines are gradually applied during the first-time stage (stage 1). Subsequently, in the second time stage (stage 2), the load induced by the mattress is introduced, while the previously applied loads remain active. This two-stage loading approach is designed to more accurately simulate real-world conditions and to minimize the effects of sudden load application. Moreover, this method enables the individual assessment of each loading component, allowing for a clearer evaluation of their respective significance. The loading values are specified in Table 4.

Table 4. Load values.

	Value
Pipe external pressure (N/m^2)	502762
Pipe internal pressure (N/m^2)	1E07
Acceleration of gravity(g) (m/s^2)	9.81
Weight of mattress (N/m)	100000

3.4. Model validation

To validate the numerical model developed in this study, a benchmark problem was simulated numerically, consisting of a pipe with an outer diameter of 1 meter and a wall thickness of 2 cm under specified boundary conditions. In this model, one end of the pipe was fixed (clamped), and an axial load of 100,000 N was applied to the free end. The objective of this analysis was to evaluate the axial displacement resulting from the applied axial load on the pipe structure. The numerical results obtained using the Abaqus software were compared with the corresponding analytical solution derived based on linear elasticity theory and classical Euler beam equations. In the analytical solution, the axial displacement due to the applied load was calculated using Eq. 6, which relates the axial load, geometric and mechanical properties of the pipe, and the resulting displacement within the elastic deformation framework:

$$\delta = \frac{PL^3}{3EI} \tag{6}$$

Each parameter employed in Eq. 6 corresponds to the values specified in Table 5.

Table 5. Analytical parameters.

***P* (N)**	100000
***L* (m)**	10
***E* (GPa)**	210

A comparison of the vertical and in-plane displacements at the free end of the pipeline, derived from the numerical simulation and analytical solution, is provided in Table 6, and the in-plane deformation of the pipe section is shown in Fig. 2.

Table 6. Comparison of numerical and analytical results.

Numerical Solution	Analytical Solution	Percentage Error (%)
0.0214728	0.021464	0.04

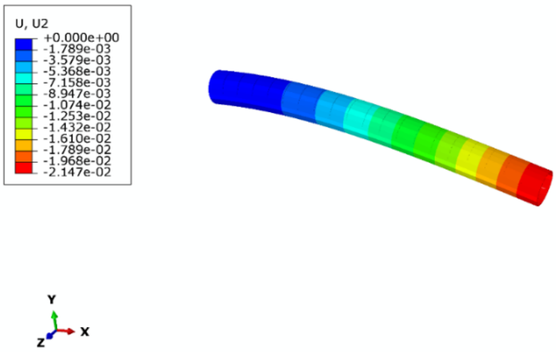

Fig. 2. In-plane deformation of the pipe-section beam.

The results obtained from the numerical and analytical analyses exhibited a satisfactory level of agreement, with the deviations falling within an acceptable range. This comparison verifies the reliability of the numerical model and confirms the appropriateness of the applied boundary conditions and loading scenarios in the simulation process. Therefore, it can be concluded that the numerical modeling approach employed in this study possesses sufficient accuracy and validity for analyzing the intended physical behavior.

4. Results and discussion

4.1. Parametric study of model geometry

The effects of varying the free span length on pipeline deformation are examined for different geometric configurations, including variations in the outer diameter and wall thickness of the pipe, as illustrated in Figs. 3 to 5.

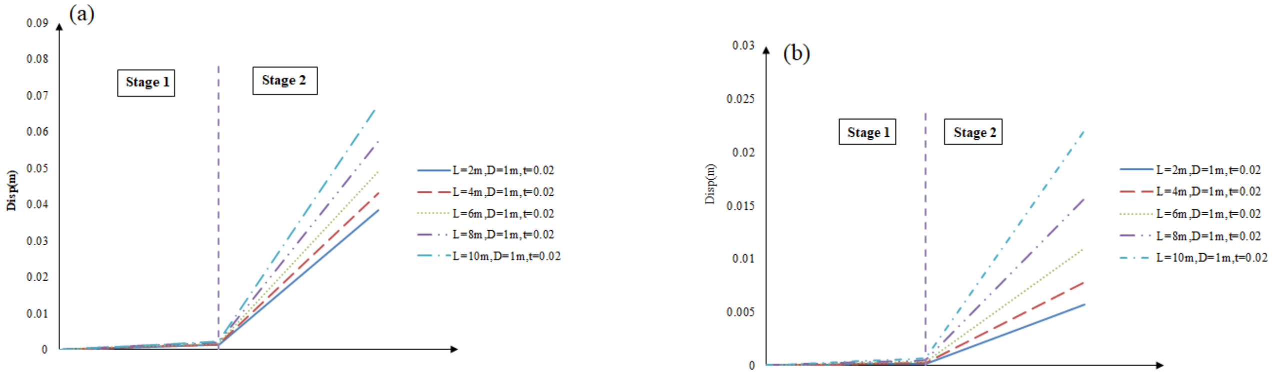

Fig. 3. Max displacement of model: D = 1 m, t = 0.02 m, in the vertical direction within the plane; a) 2D modeling, b) 3D modeling.

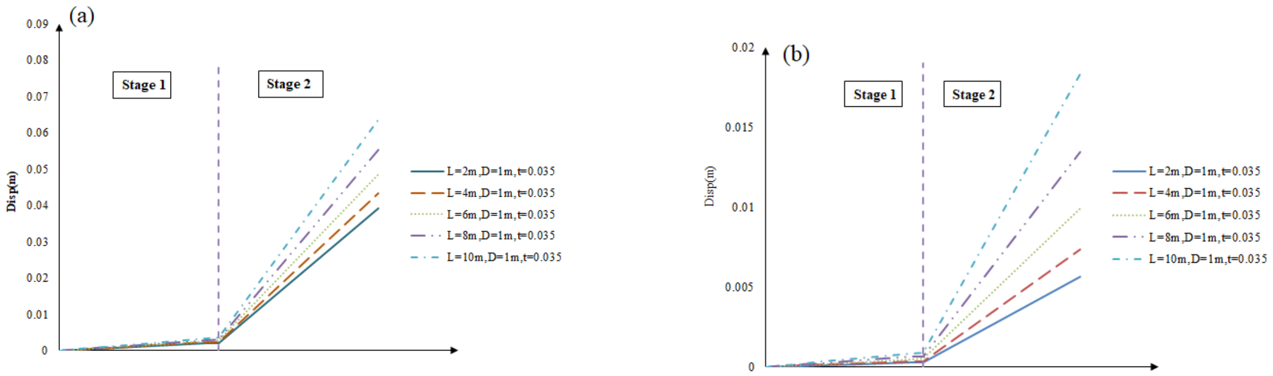

Fig. 4. Max displacement of model: D = 1 m, t = 0.035 m, in the vertical direction within the plane; a) 2D modeling, b) 3D modeling.

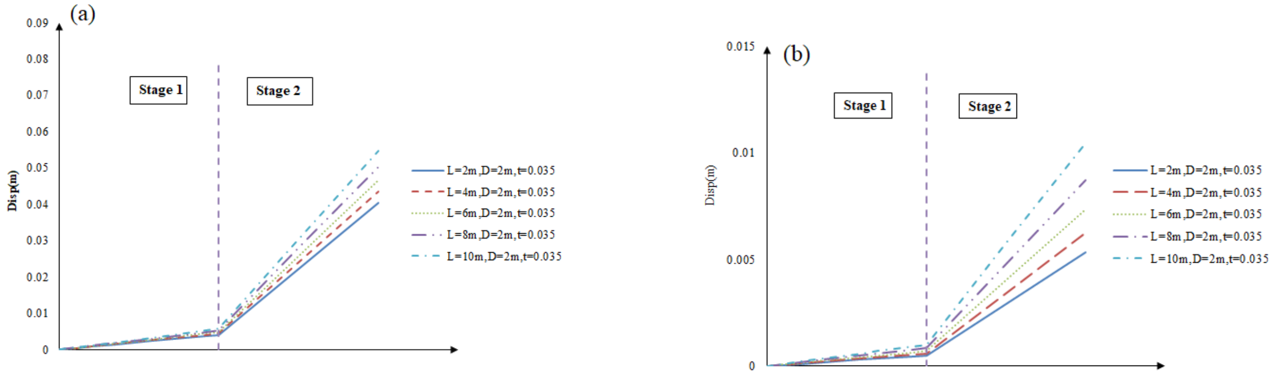

Fig. 5. Max displacement of model: D = 1 m, t = 0.035 m, in the vertical direction within the plane; a) 2D modeling, b) 3D modeling.

According to the Figs. 3 to 5, there is a pronounced and progressive increase in structural displacement with an increase in the length of the free span from 2 m to 10 m. The results obtained from the three sets of numerical displacement diagrams reveal a clear and consistent trend regarding the deformation behavior of subsea pipelines with varying geometric configurations. Specifically, pipelines with an outer diameter of 1 meter exhibit significantly larger free span displacements compared to those with a 2 m diameter. This variation can be attributed to the fundamental influence of geometric properties on flexural resistance. While the cross-sectional area and consequently the self-weight increase proportionally with the square of the radius, the moment of inertia, a key parameter governing flexural stiffness, increases with the fourth power of the radius. Therefore, assuming constant wall thickness, an increase in pipe diameter results in a substantial increase in flexural rigidity, leading to a notable reduction in deformation.

Furthermore, the comparison between 2D and 3D finite element models demonstrates considerable differences in the predicted displacement magnitudes. According to the illustrated results, the maximum displacement in the 2D model ranges from 0.03 to 0.06 meters, whereas the 3D model shows considerably lower values between 0.005 and 0.02 meters. Similar trends are observed in the other sets of diagrams, clearly indicating that 3D modeling predicts lower deformations under identical loading conditions. This distinction originates from fundamental differences in geometric representation and loading application: the 3D model incorporates the full spatial geometry of the pipe and allows for the simultaneous evaluation of bending and torsional effects, along with a more realistic load distribution and stress propagation across the structure. These factors collectively enhance the model's effective stiffness and reduce its predicted displacement. In contrast, the 2D model, based on plane strain or plane stress assumptions, is limited to simulating in-plane bending responses and fails to capture torsional resistance or out-of-plane deformation mechanisms. As a result, the 2D model generally overestimates displacement when compared to a more comprehensive 3D analysis.

The trend observed as the free span length increases from 2 to 10 meters further illustrates this distinction: according to Fig.3, the displacement increases by approximately 43% in the 2D simulations, while the same parameter shows a more pronounced 74% increase in the 3D model. This sharper gradient in the 3D case is attributed to the activation of additional deformation mechanisms such as torsion, lateral bending, and full 3D stress redistribution, which are inherently absent in 2D simulations. Moreover, in Fig.4, increasing the wall thickness leads to an approximate 5% reduction in displacement growth rate in both modeling approaches. Meanwhile, in Fig. 5, increasing the pipe diameter from 1 meter to 2 meters results in an average displacement reduction of about 20%.

Collectively, these findings highlight the critical role of geometric parameters—especially radius and cross-sectional area—in governing the flexural response of subsea pipelines through their influence on the moment of inertia. The notable differences between 2D and 3D modeling outputs strongly emphasize the necessity of full three-dimensional simulations for accurate prediction of structural behavior in free-span pipeline segments, particularly under conditions involving long spans and significant torsional interactions. While 2D models offer computational simplicity and efficiency, they may overpredict displacement magnitudes due to their inherent simplifications and limited physical representation. Moreover, the final results of the analysis clearly show that, across all three modeling scenarios (No1, No2, No3), the minimum displacement corresponds to the 2-meter span, whereas the maximum displacement is observed in the 10-meter span. This observation highlights the fact that longer spans reduce the system's flexural rigidity and enhance its susceptibility to applied loads. This behavior is in agreement with the theoretical foundations of beam mechanics and emphasizes the critical role of span length control and the consideration of time-dependent cumulative loading effects in the design of free-spanning pipelines, particularly in subsea environments, to reduce displacement and maintain structural integrity. Fig. 6 presents the overall deformation patterns of the pipeline as obtained from both two-dimensional and three-dimensional modeling approaches.

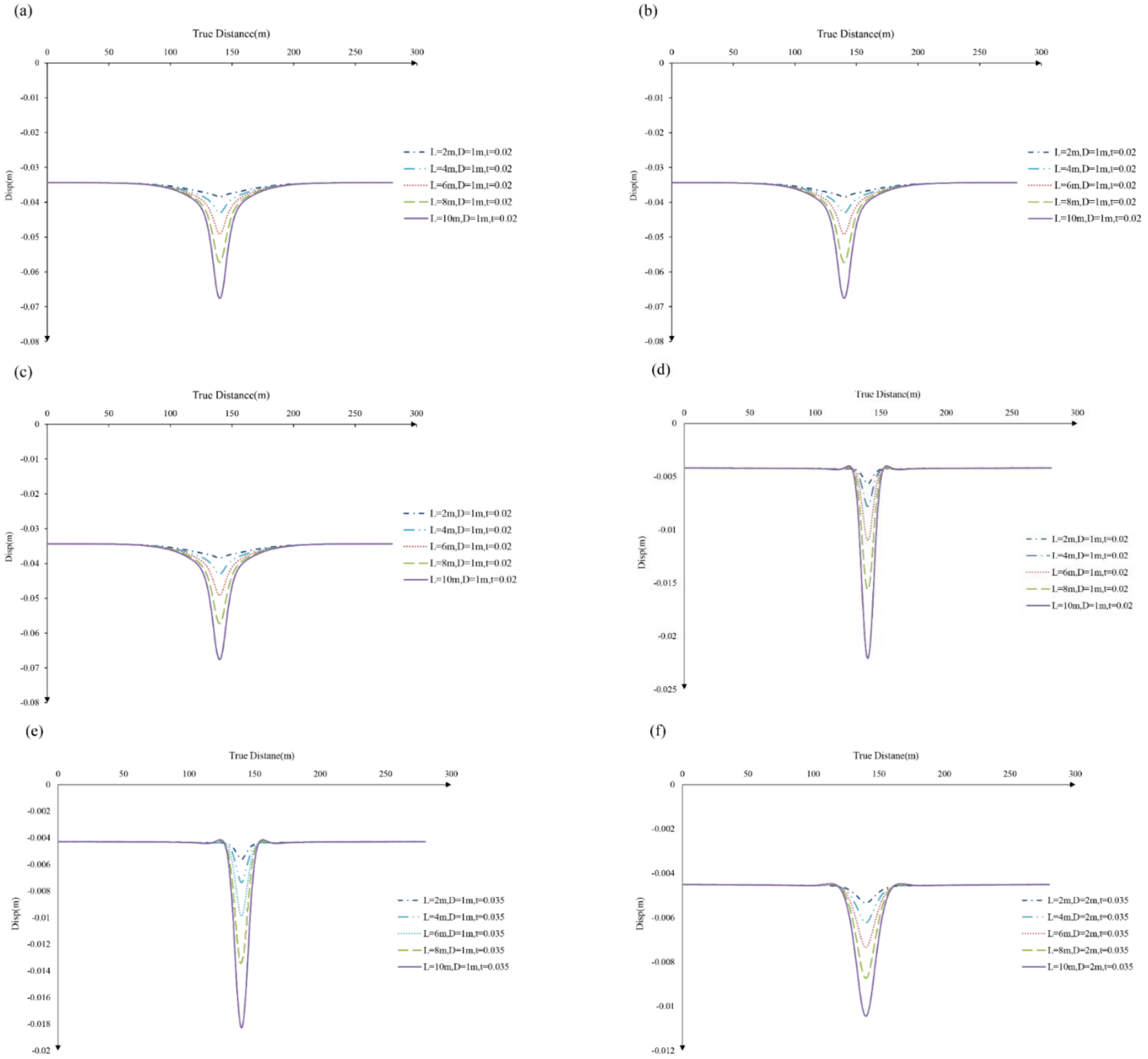

Fig. 6. Realistic pipeline deformation in all models; a,b,c) 2D modeling, d,e,f) 3D modeling.

4.2. Comparison of natural frequencies created in models

One of the additional parameters examined in both the two-dimensional and three-dimensional models is the natural frequency associated with various natural modes. The comparative evaluation of these frequencies by the 2D and 3D models is presented in Fig. 7.

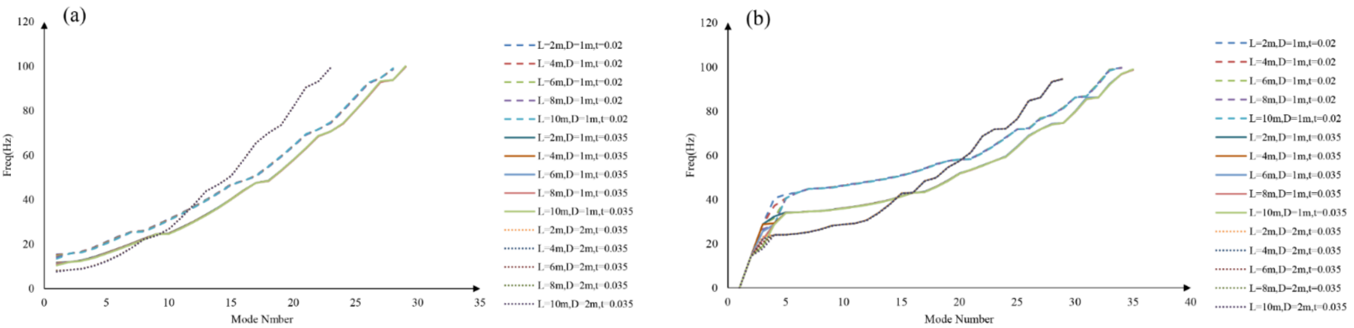

Fig. 7. Natural frequency of model: D = 1 m, t = 0.02 m; a) 2D modeling, b) 3D modeling.

Based on Fig. 7, several outcomes can be deduced from the results. First, when comparing the two-dimensional and three-dimensional models, in the lower natural modes, the frequencies obtained from the two-dimensional model are lower than the corresponding values predicted by the three-dimensional analysis. However, this trend reverses in the higher modes. The aforementioned finding is not the sole outcome derivable from this comparison. Regarding the influence of geometrical variations on natural frequencies, it is observed that changes in free span length result in only minor variations in the lower modes. The relatively minor variations in the free span length of subsea pipelines, ranging from two to ten meters in the present work, do not significantly affect the natural vibration frequency of the pipeline due to several factors. Firstly, the total length of the pipeline is substantially greater than these local variations, rendering their impact on the overall dynamic behavior negligible. Secondly, the natural frequency is primarily governed by the effective length, boundary conditions, and material properties of the entire system, which remain largely unchanged by small local length fluctuations. Thirdly, the localized nature of these variations limits their influence, as the vibrational modes are distributed throughout the entire structure rather than confined to small segments. Lastly, the inherent bending stiffness and structural rigidity of the pipeline are sufficiently high, making minor changes in free span length insufficient to produce notable shifts in the natural frequency.

In terms of diameter variation, models with smaller diameters exhibit higher natural frequencies in the initial modes, whereas in the higher modes, the trend is reversed. Variations in the external diameter of subsea pipelines have a pronounced impact on their natural vibration frequency due to the direct influence of diameter on the bending stiffness and mass per unit length of the pipeline. Specifically, the bending stiffness is proportional to the fourth power of the external diameter, as the moment of inertia of the cross-section scales approximately with D^4, where D represents the external diameter. This means that even small changes in diameter result in substantial changes in stiffness. Although the mass per unit length also increases with diameter roughly proportional to D^2, the effect of increased bending stiffness dominates in determining the natural frequency. Since the natural frequency of a vibrating system is approximately proportional to the square root of the stiffness-to-mass ratio ($\sqrt{(k/m)}$), the net effect of increasing diameter is a significant increase in natural frequency. Therefore, unlike minor variations in free span length, changes in the external diameter produce considerable shifts in the vibrational characteristics of subsea pipelines. This behavior is observed consistently in both 2D and 3D models.

Finally, with respect to wall thickness, it is evident that models with reduced thickness exhibit lower natural frequencies across all modes, a trend that holds true for both modeling approaches. The wall thickness of a subsea pipeline significantly influences its natural vibration frequency by directly affecting the cross-sectional moment of inertia and bending stiffness. An increase in wall thickness leads to a higher moment of inertia, thereby enhancing the bending stiffness of the pipeline. While greater thickness also increases the mass per unit length, the resulting increase in stiffness typically outweighs the added mass. Consequently, the ratio of stiffness to mass (k/m) increases, leading to an elevation in the natural frequency of vibration. Therefore, thicker pipeline walls contribute to higher natural frequencies, improving the pipeline's resistance to vibrational excitations.

4.3. Comparison of computational cost between 2D and 3D modeling

Despite the high level of accuracy offered by three-dimensional (3D) modeling in evaluating structural responses, this approach presents a significant challenge compared to its two-dimensional (2D) counterpart: the considerable computational effort required. The computational cost associated with 3D modeling is substantially greater than that of 2D simulations. This observation is confirmed by the simulations introduced in the previous sections. In the 2D models, the minimum and maximum run times were 19 and 40 seconds, respectively, with an average runtime of 22 seconds using a standard laptop equipped with a quad-core processor and 8 GB of RAM. In contrast, the 3D models exhibited a minimum runtime of 318 seconds and a maximum of 1996 seconds, with an average of 748 seconds on the same hardware. This represents an approximate 14-fold increase in computational time. Such a significant increase not only validates the aforementioned claim but also highlights the importance of considering computational efficiency when choosing between 2D and 3D modeling strategies, particularly in large-scale parametric studies or real-time applications where time and resources are constrained.

5. Conclusions

This study presented a detailed comparative investigation of two-dimensional (2D) and three-dimensional (3D) finite element models for the structural analysis of free-span subsea pipelines. Key parameters such as vertical deflection, natural frequencies, and computational cost were evaluated to assess the performance and applicability of each modeling approach.

The results revealed that while 2D models offer notable computational efficiency and can be effectively used in early-stage assessments, they exhibit limitations in capturing higher-mode vibrational behavior and complex dynamic responses. In contrast, 3D models demonstrated superior accuracy in representing realistic boundary conditions and deformation patterns, particularly in the presence of nonlinear interactions and complex loading scenarios, albeit at a significantly higher computational cost. Furthermore, it was observed that increasing the free span length substantially amplifies pipeline deflection, while larger diameters and thicker walls contribute to enhanced flexural rigidity and reduced displacement. The behavior of natural frequencies under varying geometric and boundary conditions was also examined, showing consistent trends across both modeling approaches. These findings underscore the critical importance of selecting appropriate modeling fidelity based on the objectives and phase of the design process. While 2D models may suffice for preliminary evaluations and parametric studies, 3D modeling remains essential for detailed structural analysis, final design validation, and integrity assessment. Overall, the insights gained from this study can inform more effective pipeline design strategies and support best practices per industry standards for free-span integrity management in subsea environments.

Despite the contributions of this study, several limitations remain, which open avenues for future research. One of the fundamental challenges in this study lies in the multiplicity of influential parameters, which necessitates extensive and diverse modeling efforts for comprehensive investigation. This complexity complicates the analysis and makes it difficult to attain a holistic understanding of the system's behavior. Therefore, it is recommended that future studies systematically evaluate the effects of various parameters by employing advanced numerical analysis methods and dimension reduction or sensitivity analysis techniques to achieve a more precise understanding of the phenomenon under investigation.

For future research, it is also suggested to examine the effects of heat transfer as a significant factor influencing system behavior. Additionally, analyzing the problem under conditions with longer free spans could provide deeper insights into the structural response under more realistic scenarios. These considerations may serve as a valuable pathway for further development and enhancement of the findings presented in this study.

Statements & Declarations

Author contributions

Meisam Qorbani Fouladi: Conceptualization, Investigation, Formal analysis, Resources, Writing - Review & Editing, Project administration, writing—original draft preparation.

Hamed Shirazi: Conceptualization, Investigation, Software, Validation.

Maryam Taghizadeh: Investigation, Methodology, Formal analysis, Writing - Review & Editing, Supervision, writing—Original draft preparation.

Giacomo Viccione: Investigation, Formal analysis, Writing - Review & Editing.

Funding

The authors received no financial support for the research, authorship, and/or publication of this article.

Data availability

The data presented in this study will be available on interested request from the corresponding author.

Declarations

The authors declare no conflict of interes.

References

[1] Nielsen, F. G., Søreide, T. H., Kvarme, S. O. VIV Response of Long Free Spanning Pipelines. In: ASME International Conference on Offshore Mechanics and Arctic Engineering; 2002 June 23–28; Oslo, Norway. p. 121-129. doi:10.1115/omae2002-28075.

[2] Xu, W.-H., Gao, X.-F., Du, J. The prediction on in-line vortex-induced vibration of slender marine structures. Acta Mechanica Sinica, 2012; 28: 1303-1308. doi:10.1007/s10409-012-0098-3.

[3] Sumer, B. M. Hydrodynamics around cylindrical strucures. 2nd ed. Singapore (SG): World Scientific Publishing Co; 2006. doi:10.1142/6248.

[4] Charanvarma, S., Shashikala, A. Dynamic Response of Free-span Sub-sea Pipelines under Vortex Induced Vibrations. Applied Mechanics and Materials, 2014; 567: 228-234. doi:10.4028/www.scientific.net/AMM.567.228.

[5] Palmer, A. C., King, R. A. Subsea Pipeline Engineering. 2nd ed. Tulsa (OK): PennWell; 2008.

[6] Blevins, R. D. Flow-induced vibration. 2nd ed. New York (NY): Van Nostrand Reinhold; 1977.

[7] Chakrabarti, S. Handbook of Offshore Engineering. 1st ed. Amsterdam (NL): Elsevier; 2005.

[8] Thomaz, T., Carneiro, D., Ellwanger, G., Nascimento, L., Pereira, S. Application of 2D Finite Element Analysis on Subsea Pipe-Soil Interaction Assessment. In: ASME 2014 33rd International Conference on Ocean, Offshore and Arctic Engineering; 2014; p. 1-9. doi:10.1115/omae2014-24670.

[9] Zhao, E., Dong, Y., Tang, Y., Cui, L. Numerical study on hydrodynamic load and vibration of pipeline exerted by submarine debris flow. Ocean Engineering, 2021; 239: 109754. doi:10.1016/j.oceaneng.2021.109754.

[10] Sharifi, S. M. H., Tasdighi, M. Evaluation of Vortex Induced Vibration Effective Parameters on Free-Span Subsea Pipelines. International Journal Of Coastal, Offshore And Environmental Engineering (ijcoe), 2019; 4: 9-15. doi:10.29252/ijcoe.3.3.9.

[11] Jiang, D., Huang, X., Zhao, D., Yang, H., Tang, G. Fatigue Life Prediction of Submarine Pipelines with Varying Span Length and Position. Journal of Marine Science and Engineering, 2025; 13: 763. doi:10.3390/jmse13040763.

[12] DET NORSKE VERITAS (DNV). DNV-RP-F105: Free Spanning Pipelines. Bærum (NO): DNV; 2021.

[13] Li, Y., Li, Y., Akbar, N. Analysis of vibration of the Euler-Bernoulli pipe conveying fluid by dynamic stiffness method and transfer matrix. Journal of Applied Mathematics and Physics, 2020; 8: 172. doi:10.4236/jamp.2020.81013.

[14] Ning, J., Lin, T., Liu, S., Bai, R., Huang, W. Three-dimensional pipeline element formulation for global buckling analysis of submarine pipelines with sleeper. Marine Structures, 2023; 90: 103428. doi:10.1016/j.marstruc.2023.103428.

[15] Hwang, W., Lee, J. S. Analytical model for the structural behavior of pipelines during lowering-in. Applied Sciences, 2019; 9: 2595. doi:10.3390/app9132595.

[16] DET NORSKE VERITAS (DNV). DNV-ST-F101: Submarine Pipeline Systems. Bærum (NO): DNV; 2021.